Formability Characterization of Sheet Metals using the Angular Stretch Bend Test

by

Nicholas Aydemir

A thesis

presented to the University of Waterloo

in fulfillment of the

thesis requirement for the degree of

Master of Applied Science

in

Mechanical and Mechatronics Engineering

Waterloo, Ontario, Canada, 2023

Author’s Declaration

This thesis consists of material all of which I authored or co-authored: see Statement of Contributions included in the thesis. This is a true copy of the thesis, including any required final revisions, as accepted by my examiners.

I understand that my thesis may be made electronically available to the public.

Statement of Contributions

Nicholas Aydemir was the sole author for this thesis and performed all testing and analysis documented within except for characterization of the yield function, hardening behavior and in-plane limit strains which were performed by my colleagues on the project, Dr. Jacqueline Noder and Edward Gutierrez.

Abstract

This thesis investigates the mechanics of the angular stretch bend test (ASBT) and analytical models using three different advanced high strength steels (AHSS) and finite element simulation. The three steels, 590R, 3rd Gen 1180, and DP980 were characterized using the ASBT. The accuracy of models from the literature used to eliminate process dependent effects such as bending, and tool contact pressure were evaluated with the experimental data. A finite element model was developed to further investigate the process correction models.

Historically, the automotive forming industry has relied upon in-plane experimental methods to produce forming limit curves (FLCs) but this can lead to overly-conservative component designs as they ignore the beneficial effects of bending and tool contact pressure that delay the onset of tensile instability, both of which are present in the ASBT. The ASBT in plane strain tension can be characterized by the bend severity which is the ratio of the blank thickness to the punch radius. The bend severity is a useful parameter but does not consider the strain path or other test parameters such as the die gap width or entry radii. To assess the effect of the die gap, a new ASBT die set was designed and used in the experimental work in this thesis. The focus of the experimental work was on three grades of automotive advanced high strength steels: 590R, DP980, and 3rd Gen 1180. Full-field strain measurements were obtained using stereo-digital image correlation (DIC). The experimental results showed that the strain paths were controlled by the bend severity and sample width while the die gap width played a secondary role.

Analytical models have been proposed in the literature to reconcile the differences between limit strains obtained using different experimental test methods. The models involve measuring surface curvature, calculating thickness based upon the curvature and surface strains, accounting for non-linear strain paths (NLSP) for linearization of the limit strains and compensating for tool

contact pressure. The curvature model was found to be sensitive to the size of the measurement window with a 20 mm window recommended. The thickness model studied from the literature was relatively complex, so a new analytical model was developed for the ASBT to determine the thickness across the range of practical bend severities from 0.14 to 1.4 using the curvature and surface strains. The new proposed ASBT thickness model was in good agreement with the finite-element data with comparable accuracy to the more complex models in the literature.

The influence of non-linear strain paths (NLSP) was found to be relatively minor in the ASBT as the strain paths were relatively linear and near plane strain. The achievable strain paths in the current ASBT using a cylindrical punch were constrained to intermediate uniaxial tension to plane strain tension. Overall, the minimal influence of NLSP on the ASBT is an advantage as the NLSP correction can be very sensitive to the limit strain detection algorithm as reported in the literature.

The analytical model to compensate for contact pressure in the literature was evaluated to the ASBT experiment data and produced promising results when comparing the pressure compensated limit strains to corresponding in-plane limit strain data. However, detailed finite element simulations of the ASBT showed that the contact pressure predicted by the model was significantly lower than the simulation values. The analytical model to compensate for the contact pressure appeared to work in some cases but is attributed to its systemic underprediction of the actual contact pressure tied with an extremely sensitive pressure correction tied to the hardening rate. It is believed that the high sensitivity to the hardening coupled with the underestimation of the contact pressure magnitude counterbalanced one another and led to reasonable corrections for the out-of-plane limit strains. Future work is required to improve the accuracy of the contact pressure model and to then re-visit the phenomenological mapping criterion used for the limit strains.

A finite element model was developed in conjunction with the experimental work to provide further insight to the models. A convergence study was performed on a plane-strain constrained ASBT model to determine the minimum number of through-thickness solid elements to obtain convergence in the strain field. Several methods to obtain contact pressure data from the finite-element simulations were considered as the contact area depends upon the solver and contact algorithms. It was observed that elastic tooling has a significant influence upon the contact pressure although the tooling is commonly idealized as rigid in metal forming simulations. Shell elements were also evaluated as they are the preferred element type in the forming industry but were not able to resolve the relatively high bend severities considered in this thesis.

Acknowledgements

This thesis would not have been completed were it not for the many contributions and support I received along the way. First and foremost, a big thank you to my supervisor Professor Clifford Butcher. Your guidance, knowledge, engineering intuition (and patience) were invaluable to me throughout. I am very grateful for your support especially during the rough times amidst the pandemic, and I appreciate that you adapted very quickly to support me remotely. A big thank you to Professor Mike Worswick, Dr. José Imbert-Boyd, Dr. Jacqueline Noder, and Kenneth Cheong who were always available to assist and mentor me whenever I had any questions in the office or lab. The lab support provided by Eckhard Budziarek, Tom Gawel, Andy Barber, Richard Gordon, Amir Zhumagulov, and Kenneth Cheong was always much appreciated, and the experimental work in this thesis would not have been possible without you!

I would also like to thank the American Iron and Steel Institute (AISI) and Dr. Hesham Ezzat for their support in this thesis. The feedback and comments from AISI were much appreciated throughout the project, and I thoroughly enjoyed working with all the individuals on the project.

A special thanks to Edward Gutierrez, these past few years would have gone by a lot slower without your support and friendship! To Dr. Kaab Omer, who always hears me out whenever I have something benign to complain about and entertains my unsolicited FEM questions. To Sante DiCecco, for always helping me out and keeping it real with me!

Lastly, to my family and my partner Mimi. Thanks for your patience and support during these past few years. I dedicate this thesis to you.

Table of Contents

Author's Declaration ii

Statement of Contributions iii

Abstract iv

Acknowledgements vii

List of Figures xii

List of Tables xx

1. Background 1

1.1. Advanced High Strength Steels and Sheet Metal Formability 1

1.2. Experimental Generation of the FLC 3

1.3. The Angular Stretch Bend Test 6

1.4. Equivalent In-plane Limit Strains and Relevant Models 8

1.5. Summary and Current Work 11

2. Experimental Methods and Materials 13

2.1. Material Properties 13

2.2. In-plane FLC Experimental Setup and Results 16

2.3. ASBT Experimental Setup 19

2.4. DIC Parameters 20

2.5. Application of the LBF Method 21

3. Angular Stretch Bend Test 23

3.1. Design of the Angular Stretch Bend Tooling 23

3.2. Sample Geometry and Test Conditions 26

3.3. Experimental Results – Strain Paths and Limit Strains 27

3.4. Influence of Die Gap 32

4. Investigation of Analytical Models to Produce Equivalent In-plane Limit Strains 36

4.1. Curvature of the Convex Surface 36

4.2. Instantaneous Thickness Models 37

4.2.1. Background on Thickness Models in Literature 38

4.2.2. New Stretch Bend Thickness Model 41

4.2.3. Evaluation of New Stretch Bend Thickness Model 43

4.3. Strain Path on Middle and Inner Layers of the Sheet 47

4.4. Non-linear Strain Path (NLSP) Correction 50

4.5. Contact Pressure Calculation and Contact Pressure Modified Limit Strains 57

4.5.1. Stretch Bend Limit Strains with Contact Pressure Correction 59

5. Stretch Bend Simulation – Development of Finite Element Model and Analysis 64

5.1. Identification of the Number of Through-thickness Solid Elements in Stretch Bending 64

5.1.1. Finite-element Model Setup 65

5.1.2. Convergence of Load-displacement Response 67

5.1.3. Thickness Strain of the Cross-Section 68

5.1.4. Through-Thickness Major Strain Distribution for Mesh Convergence 69

5.2. Evaluation of Shell Elements in Stretch-bending 71

5.2.1. Background on Shell Elements 72

5.2.2. Finite-element model of the ASB using shell elements 73

5.2.3. Load-displacement Response 73

5.2.4. Through-thickness Equivalent Strain and Normal Stress Distributions 74

5.3. Investigation of Simulation Solver, Contact Type, and Measurement of the Contact Pressure 79

5.3.1. Comparison of Load-Displacement Response with Experimental Data 79

5.3.2. Comparison of Surface Strains with Mesh Pattern and Size 80

5.3.3. Evaluation of Simulation Consistency with Implicit/Explicit Solvers and Contact Algorithms 83

5.3.4. Comparison of Simulation Contact Pressure 87

5.3.5. Contact Area Convergence Study 88

5.3.6. Improving Simulation Contact Area Curves with Lines of Best Fit 89

5.4. Investigation of Through-thickness Strain and Contact Pressure 91

5.4.1. Comparison of Load-displacement Response 92

5.4.2. Through-thickness Major Strain Distributions 93

5.4.3. Strain Path on Middle and Inner Layers of the Sheet 96

5.4.4. Contact Pressure Model Investigation 101

5.4.5. Alternative Pressure Model Investigation - Hertz Contact Pressure 110

6. Conclusions and Recommendations 118

6.1. Conclusions 118

6.2. Recommendations 121

References 123

APPENDIX A. Limit Strain Detection 129

ISO Method Limit Strain Applied to a Stretch Bend Experiment 129

APPENDIX B. Fracture Regularization 130

Fracture Regularization of the Angular Stretch Bend Test 130

APPENDIX C. Contact Stress 138

LS-DYNA Mortar Contact Stress 138

APPENDIX D. Experimental Data 140

LBF Limit Strains and Corrected Limit Strains 140

Comparison of Raw Experimental Data and Spline-fit Data 143

APPENDIX E. Tabulated Simulation Data 145

Punch Contact Area 145

Punch Displacements for Power-law material Simulations 146

List of Figures

Figure 1-1 - Automotive steels: Total elongation vs. ultimate tensile strength [2] 2

Figure 1-2 - Example of an FLC with common deformation modes and strain paths denoted (FLC_0 circled) [7] 3

Figure 1-3 - Example of in-plane deformation: Schematic of Marciniak test [8] 4

Figure 1-4 – Example of out-of-plane deformation: Schematic of Nakazima test [8] 5

Figure 1-5 – Thinning strain rate during last 30 images of a plane strain specimen before fracture with so-called stable and unstable regions identified (regions NTS) [9] 6

Figure 1-6 - Diagram of a typical ASBT 7

Figure 1-7 – Before (a) and after (b) process corrections were applied to Nakazima limit strains of an MP980 steel compared to the in-plane limit strains (Marciniak) [17] 9

Figure 1-8 - Effect of hardening model on the NLSP and pressure compensated limit strains [18] 10

Figure 1-9 - Process corrected limit strains of a 3rd Gen 1180 steel [20] a) Effect of pressure corrections b) Comparison of Marciniak and pressure corrected Nakazima limit strains 11

Figure 2-1 - Engineering stress strain response (a) and hardening rate from MHS model (b) [22] 14

Figure 2-2 - Von Mises and Yld2000 yield surfaces for studied materials [20], [22] 16

Figure 2-3 - Experimental setup of MTS press at the University of Waterloo 17

Figure 2-4 – Dimensions of Marciniak die set used to create in-plane FLCs by Noder et al. [22] and Gutierrez et al. [20] 17

Figure 2-5 - Marciniak FLCs for studied materials [20], [22] 18

Figure 2-6 - LBF limit strains for 590R and 3rd Gen 1180 [26] 19

Figure 2-7 - Example of a speckle pattern on a 590R sample with Teflon beneath (10 mm punch below Teflon not visible) 20

Figure 2-8 - Example of circle inspector in VIC-3D software (image just prior to fracture) 22

Figure 2-9 – Visible hairline crack observable in an ASBT, data processing terminated one image prior (590R, die gap width = 30 mm, punch radius = 1 mm) 22

Figure 3-1 - Upper die inserts from left to right: 30, 51, 76.2 mm 24

Figure 3-2 - Upper die without insert (left) and with 30 mm insert (right) 24

Figure 3-3 – Schematic of top and bottom die (cross-section view) of new stretch bend tooling, dimensions in mm 24

Figure 3-4 - Schematic for top die insert, dimensions in mm 25

Figure 3-5 - Stretch bend die surface knurling detail (all dimensions in mm) 25

Figure 3-6 – ASBT punch platform (left) and punches with radius of (left to right): 1, 5, 10, 15 mm 26

Figure 3-7 - Sample geometry a) 25.4 mm (1 inch) b) 76.2 mm (3 inch) 26

Figure 3-8 - 590R strain paths and LBF limit strains, 76.2 mm sample. Each punch radius and die gap combination is denoted. ’30-10’ indicates a 30 mm die gap and 10 mm radius punch. .. 28

Figure 3-9 - 590R strain paths and LBF limit strains, 25.4 mm sample 29

Figure 3-10 - DP980 strain paths and LBF limit strains, 25.4 mm sample 30

Figure 3-11 - DP980 strain paths and LBF limit strains, 76.2 mm sample 31

Figure 3-12 - 3rd Gen 1180 strain paths and mod. LBF limit strains, 25.4 mm sample 32

Figure 3-13 - 3rd Gen 1180 strain paths and mod. LBF limit strains, 76.2 mm sample 32

Figure 3-14 - Load vs. displacement for different gap widths at the same t/R, 590R, 76.2 mm sample, t/R = 0.14 34

Figure 3-15 - Load vs. displacement for different gap widths at the same t/R, 590R, 76.2 mm sample, t/R = 1.4 34

Figure 3-16 - Load vs. displacement for different gap widths. 590R, 25.4 mm sample, t/R = 0.14..... 35

Figure 4-1 - Example of curvature line extraction in VIC-3D software (image just prior to fracture)..... 37

Figure 4-2 - Infinitesimal element used in Min et al. thickness model derivation [28]. (a) circular shell element (b) 3D deformed element (c) projection of the deformed element (d) deformed 3D shell element in spherical coordinates 39

Figure 4-3 - Thickness model (SB model) 42

Figure 4-4 - Major strain at apex of sample extracted using a 0.5 mm diameter circle extractor tool 44

Figure 4-5 - Schematic illustrating how the samples were cut before viewing with the microscope 45

Figure 4-6 - Microscope image and measuring line of 590R sample R5 45

Figure 4-7 - Thickness comparison of 590R experiments, SB model, and curvature method 46

Figure 4-8 - Effect of fitting window on SB Model 47

Figure 4-9 - Strain path on layers, 590R, 76.2 mm sample, t/R=1.4..... 49

Figure 4-10 - Strain path on layers, 590R, 76.2 mm sample, t/R=0.28..... 49

Figure 4-11 - Strain path on layers, 590R, 76.2 mm sample, t/R=0.14..... 50

Figure 4-12 - 590R NLSP Corrections, t/R = 1.4, 76.2 mm sample 52

Figure 4-13 – 590R NLSP Corrections, t/R = 0.28, 76.2 mm sample – Arrow denotes general shift of limit strains after NLSP correction 52

Figure 4-14 – 590R NLSP Corrections, t/R = 0.14, 76.2 mm sample – Arrow denotes general shift of limit strains after NLSP correction 53

Figure 4-15 - 3rd Gen 1180 NLSP Corrections, t/R = 1.4, 76.2 mm sample 54

Figure 4-16 - 3rd Gen 1180 NLSP Corrections, 25.4 mm sample – Arrow denotes general shift of limit strains after NLSP correction 55

Figure 4-17 - DP980 NLSP corrections, t/R=1.4, 76.2 mm sample - Arrow denotes general shift of limit strains after NLSP correction 56

Figure 4-18 -DP980 NLSP corrections, t/R=0.093 & 0.28, 25.4 mm sample - Arrows denote general shift of limit strains after NLSP correction 56

Figure 4-19 - 590R Pressure Corrected Limit Strains, t/R = 1.4, 76.2 mm sample – arrow denotes general shift of limit strains after pressure correction 59

Figure 4-20 - 590R Pressure Corrected Limit Strains, t/R = 0.28, 76.2 mm sample - arrow denotes general shift of limit strains after pressure correction 60

Figure 4-21 - 590R Pressure Corrected Limit Strains, t/R = 0.14, 76.2 mm sample - arrow denotes general shift of limit strains after pressure correction 60

Figure 4-22 - 3rd Gen 1180 Pressure Corrected Limit Strains, t/R = 1.4, 76.2 mm sample . 61

Figure 4-23 - 3rd Gen 1180 Pressure Corrected Limit Strains, 25.4 mm sample - arrow denotes general shift of limit strains after pressure correction 62

Figure 5-1 - Schematic of the ASBT model 65

Figure 5-2 - Detail view of mesh in ASBT mesh convergence model 66

Figure 5-3 – Stress-strain response and hardening rate of power-law material used in simulations, $\boldsymbol{K = \sigma y = 500}$ MPa 67

Figure 5-4 – Variation of load vs. displacement response with number of elements through-thickness 68

Figure 5-5 – Variation of thickness strain with number of elements through-thickness plotted against punch displacement 69

Figure 5-6 - Variation of the major strain through-thickness of the sheet with number of elements at the peak load 70

Figure 5-7 – Variation of the major strain through-thickness of the sheet with number of elements at 75% max. load punch displacement 70

Figure 5-8 - Variation of the major strain through-thickness of the sheet with number of elements at 50% max. load punch displacement 71

Figure 5-9 - Load-displacement response comparison of shells vs. solids 74

Figure 5-10 - Through-thickness strain comparison, 2.3 mm punch displacement 75

Figure 5-11 - Through-thickness strain comparison, 3.4 mm punch displacement 75

Figure 5-12 - Through-thickness strain comparison, 4.5 mm punch displacement 76

Figure 5-13 – Through-thickness stress comparison, 2.3 mm punch displacement 77

Figure 5-14 – Through-thickness stress comparison, 3.4 mm punch displacement 77

Figure 5-15 – Through-thickness stress comparison, 4.5 mm punch displacement 78

Figure 5-16 - Quarter symmetry model with 76.2 mm sample, 30 mm die gap, and 1 mm radius punch 79

Figure 5-17 – Load-surface displacement response of various meshes 80

Figure 5-18 - Schematic showing data collection line for major strain on the surface 81

Figure 5-19 - Surface major strain comparison - 2 mm punch displacement 82

Figure 5-20 - Surface major strain comparison - 4 mm punch displacement 82

Figure 5-21 - Surface major strain comparison - 6 mm punch displacement - experimental limit strain 83

Figure 5-22 - Load-displacement response of 2-way contacts, 1 mm mesh 86

Figure 5-23 - Load-displacement response of 1-way contacts and implicit for reference, 1 mm mesh 87

Figure 5-24 - Normalized interface pressure comparison, 1 mm mesh 88

Figure 5-25 - Punch mesh detail for contact area convergence study 89

Figure 5-26 - Punch contact area for various punch mesh sizes - raw data from LS-DYNA 89

Figure 5-27 - Punch contact areas, trendlines dotted 90

Figure 5-28 - Contact pressure comparison of raw simulation data and cubic trendline method - blank mesh vs. punch mesh 91

Figure 5-29 - Load-displacement response and limit strains of all power-law material simulations 92

Figure 5-30 - Through-thickness major strain distribution, n=0.1, t/R=1.4 94

Figure 5-31 - Through-thickness major strain distribution, n=0.3, t/R=1.4 94

Figure 5-32 - Through-thickness major strain distribution, n=0.1, t/R=0.14 95

Figure 5-33 - Through-thickness major strain distribution, n=0.3, t/R=0.14 95

Figure 5-34 - Strain path on layers comparison, n=0.1, t/R=1.4, rigid punch 97

Figure 5-35 - Effect of fitting interval on strain model, n=0.1, t/R=1.4, rigid punch 98

Figure 5-36 - Simulation coordinate data and quadratic fits, n=0.1, t/R=1.4, rigid punch 99

Figure 5-37 - Simulation coordinate data and quadratic fits, n=0.1, t/R=0.14, rigid punch .. 99

Figure 5-38 - Strain path on layers comparison, n=0.1, t/R=1.4, elastic punch 100
Figure 5-39 - Strain path on layers comparison, n=0.1, t/R=0.14, rigid punch..... 101
Figure 5-40 - Punch contact area for rigid/elastic tooling simulations..... 102
Figure 5-41 - Punch contact area trendlines for rigid/elastic tooling simulations..... 102
Figure 5-42 - Normalized contact pressure, t/R = 1.4 Simulations 103
Figure 5-43 - Normalized contact pressure, t/R = 0.14 Simulations 103
Figure 5-44 - Simulation pressure normalized by flow stress, rigid tooling simulations.... 105
Figure 5-45 - Simulation pressure normalized by flow stress, elastic tooling simulations . 105
Figure 5-46 - Simulation vs. Min model contact pressure, n=0.1, t/R=1.4, rigid punch..... 107
Figure 5-47 - Simulation vs. Min model contact pressure, n=0.1, t/R=1.4, elastic punch .. 107
Figure 5-48 - Simulation vs. Min model contact pressure, n=0.3, t/R=1.4, rigid punch..... 108
Figure 5-49 - Simulation vs. Min model contact pressure, n=0.3, t/R=1.4, elastic punch .. 108
Figure 5-50 - Simulation vs. Min model contact pressure, n=0.1, t/R=0.14, rigid punch... 109
Figure 5-51 - Simulation vs. Min model contact pressure, n=0.1, t/R=0.14, elastic punch 109
Figure 5-52 - Simulation vs. Min model contact pressure, n=0.3, t/R=0.14, rigid punch... 110
Figure 5-53 - Simulation vs. Min model contact pressure, n=0.3, t/R=0.14, elastic punch 110
Figure 5-54 - Hertz contact pressure: a) cylinder contact with inner cylinder. b) schematic of ASBT 111
Figure 5-55 - Simulation pressure vs. Hertz, n=0.1, t/R=1.4, rigid punch 112
Figure 5-56 - Simulation pressure vs. Hertz, n=0.1, t/R=1.4, elastic punch 112
Figure 5-57 - Power-law and E_2 parameter comparison, n = 0.1 material 114
Figure 5-58 - Simulation and Modified Hertz Pressure, n=0.1 material, rigid tooling 115
Figure 5-59 - Simulation and modified Hertz pressure, n=0.1 material, elastic tooling 115

Figure 5-60 – Simulation and modified Hertz pressure, n=0.3 material, rigid tooling 116

Figure 5-61 – Simulation and modified Hertz pressure, n=0.3 material, elastic tooling..... 116

Figure A-1 - ISO method applied to an ASBT 129

Figure B-1 - 3rd Gen 1180 fracture locus..... 131

Figure B-2 - Regularization blank mesh details (1 mm) 132

Figure B-3 - Load-displacement regularization (3in-30-1) 133

Figure B-4 - Load-displacement regularization (1in-51-5) 134

Figure B-5 - Load-displacement regularization (1in-51-15) 135

Figure B-6 - 3rd Gen 1180 Regularization factors (tensile, ASBT, PS/EB domes)..... 136

Figure C-1 - Effect of the IGAP parameter on the mortar contact stress 139

Figure D-1 - Comparison of raw and spline-fit strain path data (590R, t/R=1.4) 144

List of Tables

Table 2-1 - Tensile Mechanical Properties of Steels Used in Experiments (± standard deviation) 14

Table 2-2 - Modified Hockett-Sherby Coefficients for Studied Materials 15

Table 2-3 - Plastic Anisotropy of Studied Materials 15

Table 2-4 – Yld-2000 Coefficients for Studied Materials 15

Table 2-5 - DIC parameters for experiments by material 21

Table 3-1 - List of test conditions for the 76.2 mm sample geometry 27

Table 3-2 - List of test conditions for the 25.4 mm sample geometry 27

Table 3-3 - Major limit strain averages and standard deviations (590R, 76.2 mm sample) .. 33

Table 4-1 - Tabulated comparison of 590R thickness tests, SB model, and curvature method 46

Table 5-1 - Mesh sizes for mesh convergence study 66

Table 5-2 - Shell element and IDOF settings used in shell element study 73

Table 5-3 - Simulation Details to compare solver and contact type 85

Table 5-4 - Punch mesh element sizes 88

Table 5-5 - Power-law simulation details (gap width 30 mm) 92

Table 5-6 – Average $\boldsymbol{E2}$ parameter 117

Table B-1 - Fracture regularization test conditions (3rd Gen 1180) 130

Table D-1 – 590R Limit Strains (25.4 mm sample) 140

Table D-2 - 590R Limit Strains (76.2 mm sample) 141

Table D-3 – 3rd Gen 1180 Limit Strains (25.4 mm sample) 142

Table D-4 – 3rd Gen 1180 Limit Strains (76.2 mm sample) 142

Table D-5 - DP980 Limit Strains (25.4 mm)..... 143

Table D-6 - DP980 Limit Strains (76.2 mm sample) 143

Table E-1 - Cubic coefficients for punch contact area trendlines for punch mesh convergence study..... 145

Table E-2 - Cubic coefficients for punch contact area trendlines of rigid/elastic tooling simulations..... 145

Table E-3 - Punch displacements shown in through-thickness major strain distribution figures 146

1. Background

1.1. Advanced High Strength Steels and Sheet Metal Formability

One of the primary challenges faced in the automotive industry is how to increase fuel efficiency and lower greenhouse gas emissions without compromising on occupant safety. [1]. The incorporation of advanced high strength steels (AHSS) for structural lightweighting is an active area of research as thinner gage components can be produced to reduce weight relative to traditional steels [1]. AHSS grades such as dual-phase steel were not widely incorporated into vehicles until the 2000's. Great strides have been made in the past two decades in refining the microstructures and chemistry of AHSS grades. The AHSS category now represents a diverse range of steels with multiple variants of grades tailored to the application such as for global or local formability.

The development of AHSS can be split into 'generations', with the first generation largely consisting of dual-phase (DP), complex phase (CP), and transformation induced plasticity (TRIP) steels. The second generation introduced twinning-induced plasticity (TWIP) steels that met the goals of increasing strength without sacrificing ductility. However relatively high costs and challenges with welding due to their high alloy content limited industrial application [2], [3]. The third generation of AHSS were developed to address the gap between the first and second generation steels as shown in the so-called 'banana diagram' in Figure 1-1 that shows total elongation (%) vs. tensile strength (MPa) of automotive steels.

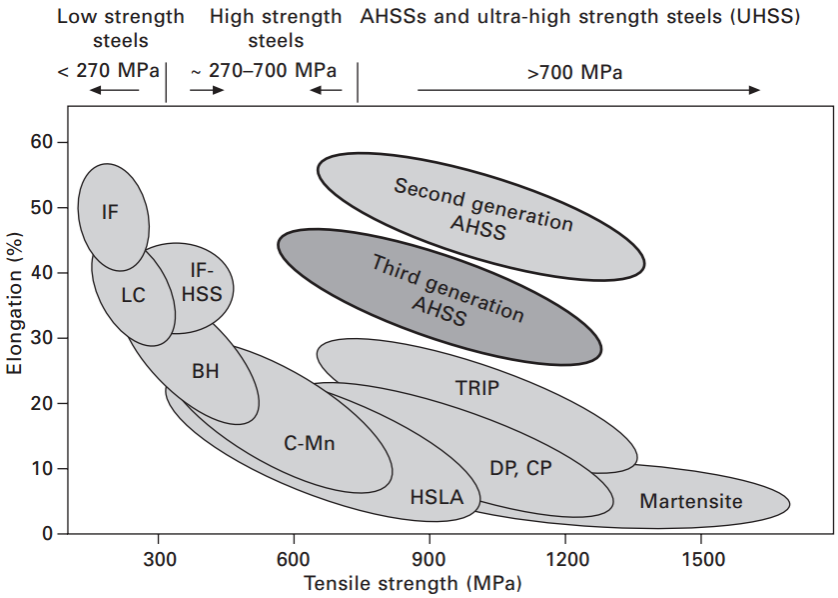

Figure 1-1 - Automotive steels: Total elongation vs. ultimate tensile strength [2]

The banana diagram illustrates the general trade-off with strength but only approximately correlates with formability, which is governed by the hardening behavior of the steel which is not captured by the tensile strength and total elongation. Materials with identical ultimate strength and total elongations may have vastly different forming properties. In general, the higher the hardening rate, the higher the uniform elongation and forming limits. Sheet metal formability is a term used to describe the amount of plastic deformation a sheet metal part can withstand before the formation of an acute neck (strain localization) or fracture [4]. Physically, an acute neck corresponds to a local surface defect that is prone to fracture with subsequent deformation. For class-A surfaces that will be painted, such as body skins and closure panels, a surface defect such as an acute neck is sufficient to reject the part.

One way to quantify and visualize formability is the forming limit curve (FLC) in terms of the major and minor strains that correspond to the formation of an acute neck. The FLC concept was introduced by Keeler for positive minor strains [5] in stretching operations and extended by Goodwin [6] for negative minor strains found in drawing operations. In the generation of the FLC,

the principal strain history or strain path is obtained from an experiment and a limit strain detection method is used to obtain the limit strain. Multiple tests are required to obtain the limit strains in strain paths from uniaxial to equal-biaxial stretching.

An example of an FLC is shown in Figure 1-2 along with the strain paths of common deformation modes in sheet metal forming. The FLC is the red curve in Figure 1-2 which is created by joining the limit strains of multiple experiments in different deformation modes together. The lowest limit strains are obtained in plane strain tension in which there is no minor strain and is commonly referred to as the FLC_0.

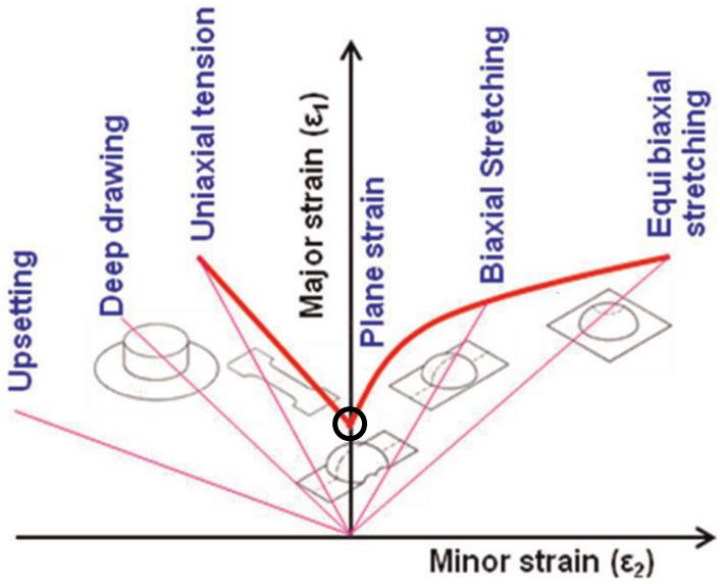

Figure 1-2 - Example of an FLC with common deformation modes and strain paths denoted (FLC_0 circled) [7]

1.2. Experimental Generation of the FLC

The concept of the FLC is built upon the assumption of in-plane proportional loading in linear strain paths. Out-of-plane tests can also be used but typically have higher limit strains.

The Marciniak test is commonly used for in-plane formability which involves stretching the material over a flat punch, see Figure 1-3. A sacrificial material referred to as a 'carrier blank' with

a central hole is placed between the punch and blank such that the centre of the blank is unsupported and experiences frictionless in-plane stretching. The carrier blank should be at least as ductile as the test sample, have a thickness of at least 0.8 times the thickness of the test sample, and the diameter of the central hole, D_{bh}, should be 32-34 mm [8].

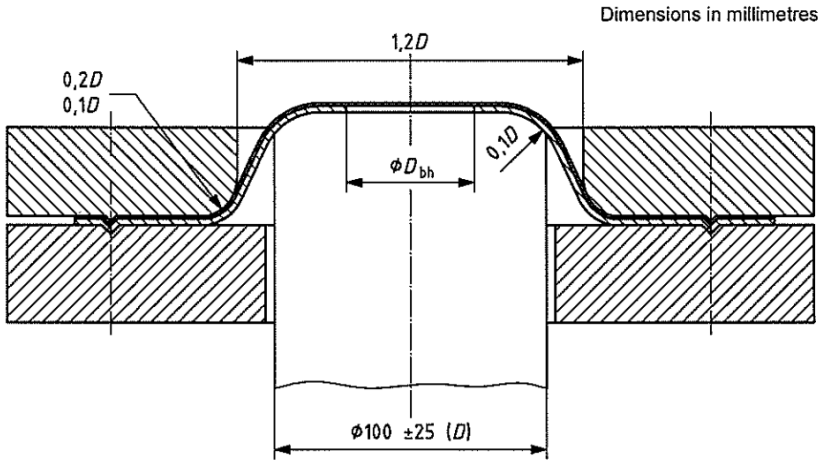

Figure 1-3 - Example of in-plane deformation: Schematic of Marciniak test [8]

Out-of-plane deformation is typically related to bending in sheet metal forming as shown in Figure 1-4 with a schematic of the Nakazima dome test which uses a hemispherical punch with a radius of 50 mm. Friction and tool contact pressure along with the out-of-plane bending serve to stabilize deformation and delay the onset of necking relative to the in-plane Marciniak tests. The Nakazima test remains the most common method for FLC generation due to its simplicity compared to the Marciniak that requires the sacrificial carrier blank.

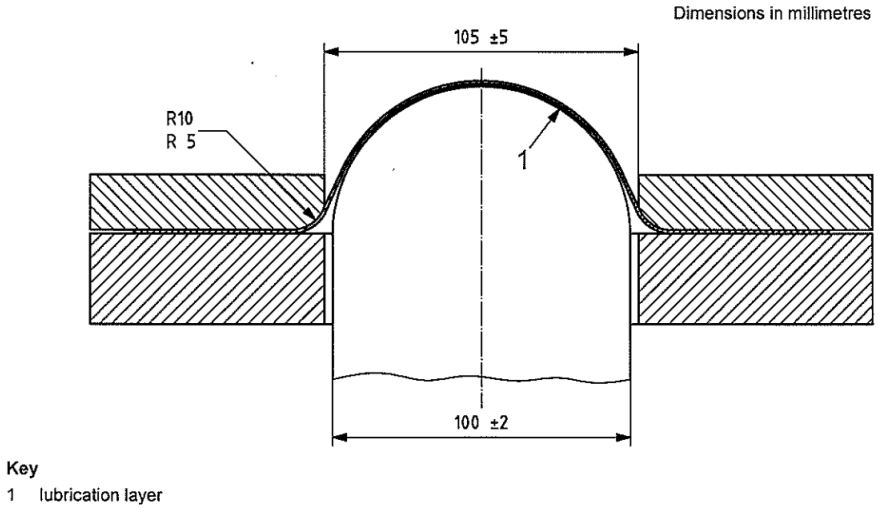

Figure 1-4 – Example of out-of-plane deformation: Schematic of Nakazima test [8]

The ISO-12004-2 standard [8] on formability characterization (i.e., creation of FLCs) allows both Marciniak and Nakazima tests and views them as interchangeable although the limit strains produced by either experimental method can vary significantly depending upon the material and thickness. The limit strain detection methodology within ISO-12004-2, denoted hereafter as "ISO method" is designed for in-plane stretching. The limit strains are obtained by performing inverse parabolic fits of the measured strain distribution prior to fracture. For the Nakazima test, the use of a 50 mm radius hemispherical punch is deemed sufficiently large to approximate in-plane stretching.

The ISO method for limit strain detection has been reported as being conservative and its assumptions about the strain distribution at necking are not valid for general forming operations that often involve stretching and bending. Volk and Hora [9] introduced a temporal method for limit strain detection using the fact that the onset of strain localization corresponds to an abrupt increase in the thinning strain rate. The method is referred to here as the 'linear best-fit method' (LBF). Deformation is idealized into homogeneous (stable) and inhomogeneous (unstable) phases.

Linear fitting of the strain rate history in each phase and the intersection of the lines provides the limit strain as shown in Figure 1-5. Noder et al. [10] proposed a modified LBF method better suited for stretch and tight radius bending to account for non-linearity in the strain rates due to initial punch contact and bending.

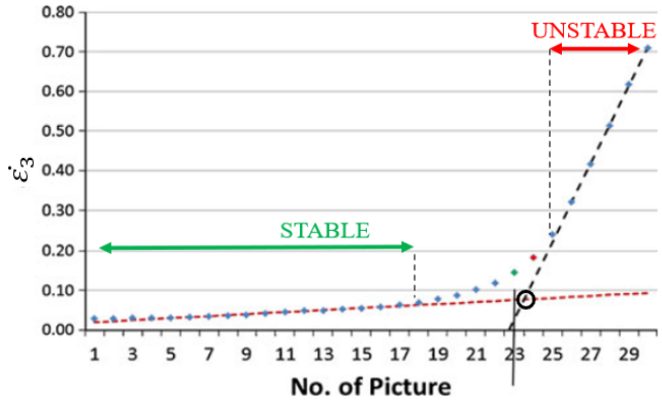

Figure 1-5 – Thinning strain rate during last 30 images of a plane strain specimen before fracture with so-called stable and unstable regions identified (regions NTS) [9]

1.3. The Angular Stretch Bend Test

The angular stretch bend test (ASBT) is used to quantify formability using bending with superimposed tension to represent deformation caused by small punch and/or die radii in deep drawing processes. In the ASBT, a blank is clamped by an upper and lower die and stretched by a cylindrical punch until fracture. The ASBT produces strain paths between plane strain and uniaxial tension (refer to Figure 1-2). The strain path can be altered by changing the specimen geometry, and punch geometry [11]. The bend severity of the ASBT can be quantified with a dimensionless ratio of the sheet thickness to the punch radius (t/R) but it is not a unique metric to describe the ASBT because it does not account for the strain path. However, since the ASBT primarily produces strain paths close to plane strain tension, the bend severity can still be a useful metric for this test.

A typical setup for the ASBT is shown in Figure 1-6. Unfortunately, there is currently no standard governing the ASBT to reconcile differences in tooling and sample geometry. Consequently, a wide variety of tooling and sample geometries have been used in the literature, and a gap exists in the literature as transferability of results has not been quantified. Notable studies were performed by Tharrett and Stoughton [12], Kitting et al. [13], Neuhauser et al. [11], Morales-Palma et al. [14], and Cheong [15].

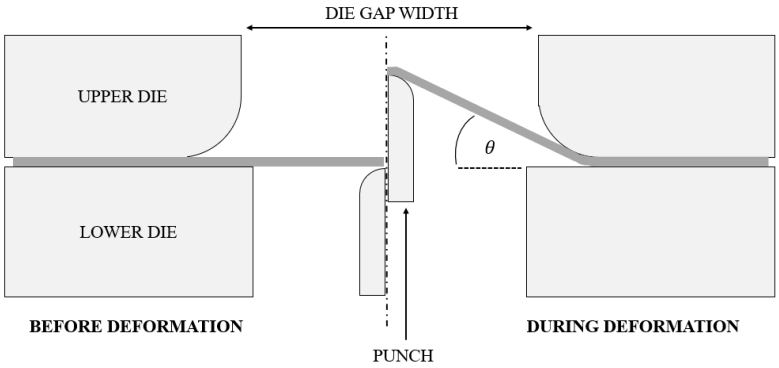

Figure 1-6 - Diagram of a typical ASBT

The ASBT highlights the limitations of the traditional FLC because the principal strain history (strain path) alone cannot distinguish if the strain was accumulated in-plane or out-of-plane to quantify the severity of bending (curvature) and contact pressure. Experimentally, the through-thickness stress and strain gradients due to bending and tool contact are known to stabilize deformation to delay or ultimately suppress necking if sufficiently severe [10]–[14], [16]. Consequently, higher strain levels can be reached before the inner layers will become sufficiently stretched in tension to activate a necking mode. Fracture on the convex surface in tension may also occur before necking as in the tight radius v-bend test. Although the influence of bending is well-known, the quantification of bend severity and how to account for it in the design phase of a forming operation has been the challenge. Furthermore, differences of tooling in the literature have

not been studied, and whether or not parameters such as the die gap width affect transferability of results.

1.4. Equivalent In-plane Limit Strains and Relevant Models

Recently, the idea of an equivalent in-plane FLC was proposed by Min et al. [17] where the limit strains produced using an experimental method involving process-dependent effects can be 'corrected' to obtain the in-plane limit strains. The so-called 'process corrections' are models that account for non-linear strain path (NLSP), curvature (bending strain), and contact pressure.

If the process corrections are accurate, it would mean both an in-plane and out-of-plane FLC can be created with one test method like Nakazima or ASBT. Min et al. [17] applied the process corrections to Nakazima tests of an MP980 steel using punch radii of 50.8 and 25.4 mm (denoted Nakazima-2 and Nakazima-4 respectively) and compared the results to the corresponding in-plane FLC (Marciniak). Min et al. [17] showed that the correction models had minimal effect on the Marciniak limit strains where the process-dependent effects are minimal. The results before and after the process corrections were applied are shown in Figure 1-7.

The process corrected limit strains for both Nakazima-2 and Nakazima-4 experiments show good agreement with the in-plane Marciniak FLC. However, there is a gap in the literature as these process corrections have not been applied to experiments that produce higher bend severities relative to the Nakazima test such as the ASBT. In the aforementioned study, the Nakazima-4 tests only have a bend severity twice as large as the standard Nakazima test which is considered an in-plane experimental method according to the ISO standard. In Chapter 4, the process correction models are applied to ASBT experimental data with a wide range of bend severities from 0.08 to 1.4.

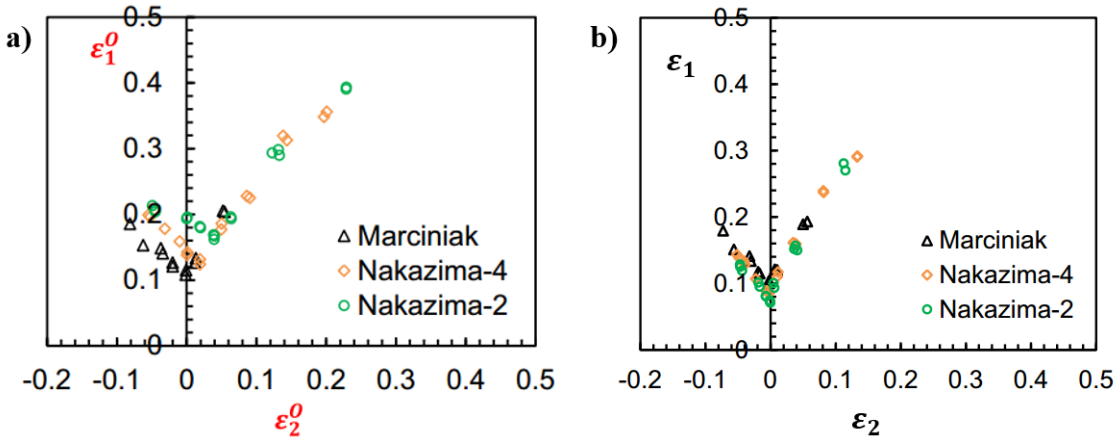

Figure 1-7 – Before (a) and after (b) process corrections were applied to Nakazima limit strains of an MP980 steel compared to the in-plane limit strains (Marciniak) [17]

Another gap exists in the literature as the process corrections of Min et al. [17] to estimate the thickness during out-of-plane bending and stretching and the compensation of the contact pressure have not been critically evaluated using finite-element analysis. Phenomenological forms were proposed and although they appear to have worked well for Nakazima tests, Noder et al. [18] showed a strong coupling of the contact stress with the hardening exponent that may not be physical. Noder et al. [18] showed that the limit strains can be incorrectly overcompensated below that of the in-plane, frictionless FLC which can be exacerbated by the hardening model as shown in Figure 1-8. The Hockett-Sherby (HS) hardening law calibrated using only tensile data produces a non-physical FLC after the NLSP and pressure corrections are applied. In contrast, the Hollomon and modified Hockett-Sherby (MHS) hardening models calibrated with tensile and shear tests produce a viable FLC.

A subsequent analysis by Noder [19] derived closed form solutions for the onset of instability in plane strain with contact pressure and found overall poor agreement with the Min et al. [17] method. A discussion of the contact pressure compensation and thickness estimation in stretch bending will be provided in Chapter 4.

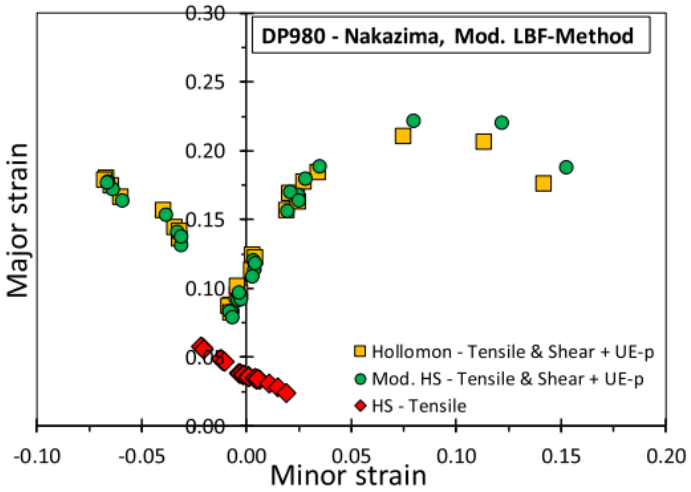

Figure 1-8 - Effect of hardening model on the NLSP and pressure compensated limit strains [18]

Nevertheless, the process corrections of Min et al. [17] and their good agreement in other studies such as by Gutierrez et al. [20] and Butcher et al. [21] for AHSS makes them attractive to consider in high bend severity experiments such as stretch bending. An example of the process corrections applied to a 3rd Gen 1180 steel by Gutierrez et al. [20] are shown in Figure 1-9. The methodology is attractive because if key information of the forming process is known or can be estimated (tool contact pressure for example), the corrections could be applied inversely to the in-plane (Marciniak) FLC to obtain the out-of-plane FLC corresponding to the forming conditions (Nakazima, ASBT). The ability to map an out-of-plane FLC to an in-plane FLC (or vice-versa) would be invaluable to the metal forming industry since producing experimental FLCs is both costly and time-consuming. Therefore, assessing if the process corrections work across a wide range of bend severities is a key motivation in this thesis.

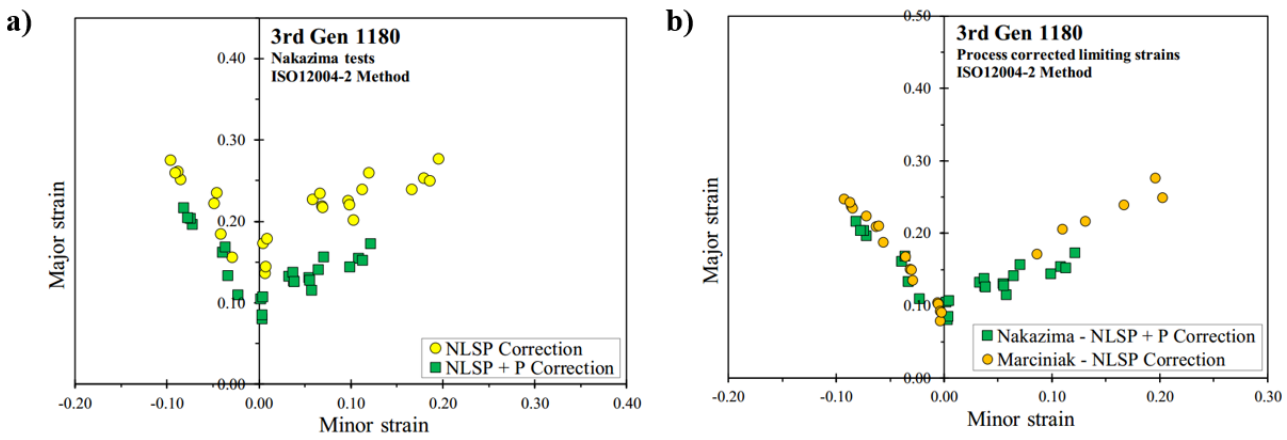

Figure 1-9 - Process corrected limit strains of a 3rd Gen 1180 steel [20] a) Effect of pressure corrections b) Comparison of Marciniak and pressure corrected Nakazima limit strains

1.5. Summary and Current Work

The ASBT can be a useful tool for characterizing sheet metal formability and its application to the virtual design of forming operations where the regions of the part experience stretch-bending and high tool contact pressures. The conventional FLC will be excessively conservative and erroneously predict fracture in regions that are otherwise safe. While the conservative FLC will result in increased success rates in die tryout, it can also result in missed opportunities for lightweighting, particularly for the third generation of AHSS with strength levels of 1180 MPa and higher where the forming windows are constrained. The influence of the non-linear strain path, thinning during stretch-bending, and the tool contact pressure on the forming limits must be considered. The correction methodology of Min et al. [17] is attractive but also requires critical evaluation using finite-element analysis to evaluate and if necessary, modify the sub-models for contact pressure and thinning.

The objectives of this thesis are:

1) Develop a modular angular stretch bend test for use with stereo DIC strain measurement with the unique ability of using multiple die gap widths to assess their effects on the limit strains
2) Investigate the process corrections proposed by Min et al. [17] using experimental ASBT data for curvature, NLSP and contact pressure
3) Develop a simplified model to predict the sheet thickness in the ASBT using DIC surface strain and geometry data
4) Perform a detailed finite-element analysis of the ASBT to evaluate the following process correction models with through-thickness data not available in-situ
    a. Through-thickness strain
    b. Contact pressure

The thesis is organized as follows: Chapter 2 details the materials and experimental setup used in the experiments. Chapter 3 details the design, development and testing of the of the stretch bend tooling. Chapter 4 details the process corrections, and application to the experimental data of Chapter 3.

In Chapter 5 a finite element model of the stretch bend test is developed. The choice of element formulation, solid or shell, solver (explicit vs. implicit) and contact algorithms are evaluated. Rigid and elastic tooling were compared with two power-law materials and two different bend severities. An alternative pressure model was trialed on the simulation data. Conclusions and recommendations for future work are provided in Chapter 6.

2. Experimental Methods and Materials

In this chapter an overview of the experimental methods and materials of interest is provided. The experimental work consists of angular stretch bend tests for three grades of steel. Two sample geometries were used for each material, however, the range of bend severities tested differed for each material. Full-field strain measurement using stereo DIC was used for all tests. The limit strains were obtained using the time-dependent LBF method of Noder et al. [10].

2.1. Material Properties

Three grades of steel were considered throughout the thesis denoted as 590R, DP980, and 3rd Gen 1180. The mechanical property data for the DP980, 3rd Gen 1180 data was published by Noder et al. [18] and Gutierrez et al. [20], respectively. The 590R property data was published by Noder et al. [22]. The engineering stress vs. strain responses are shown in Figure 2-1a, and the tensile properties provided in Table 2-1; The tensile tests were performed with the JIS No. 5 geometry with a gage width of 25 mm and analyzed with an axial extensometer gage length of 50 mm. The shear-conversion introduced by Rahmaan et al. [23] was employed to obtain the hardening response at large strains past the onset of diffuse necking in the tensile tests.

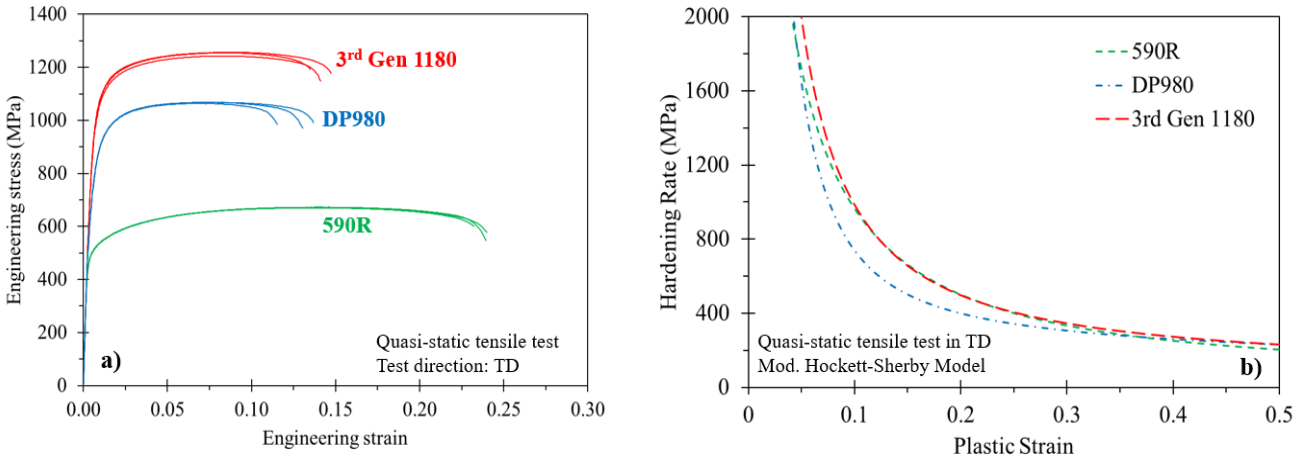

Figure 2-1 - Engineering stress strain response (a) and hardening rate from MHS model (b) [22]

Table 2-1 - Tensile Mechanical Properties of Steels Used in Experiments (± standard deviation)

Material and nominal thickness	Yield Stress (0.2% offset) (MPa)	Ultimate Tensile Stress (UTS) (MPa)	Uniform Elongation (UE) (%)	Total Elongation (TE) (%)
590R [10], t =1.4 mm	490 ± 2	671 ± 1	14.4 ± 0.1	23.8 ± 0.4
DP980 [10], t = 1.2 mm	735 ± 2	1065 ± 3	7.8 ± 0.2	13.7 ± 0.5
3rd Gen 1180 [20], t = 1.4 mm	950 ± 12	1251 ± 8	8.4 ± 0.2	14.1 ± 0.6

The so-called Modified Hockett-Sherby hardening model (MHS) [18] was calibrated to the hardening data and has the form:

$$\bar{\sigma} = A - (A - B)\exp\left(-C\left(\varepsilon_{eq}^{p}\right)^{D}\right) + F\sqrt{\varepsilon_{eq}^{p}}\,. \tag{2.1.1}$$

The MHS parameters for the three materials are provided in in Table 2-2, with the hardening rate evolution shown in Figure 2-1b.

Table 2-2 - Modified Hockett-Sherby Coefficients for Studied Materials

Material	A (MPa)	B (MPa)	C (−)	D (−)	F (MPa)
590R [10]	743.3	448.0	4.53	0.58	217.71
DP980 [10]	1072.87	604.90	11.54	0.50	327.25
3rd Gen 1180 [20]	1323.56	785.15	5.29	0.395	281.46

The Lankford coefficients (R-values) of the three steels are provided in Table 2-3. To model the anisotropic behaviour of the materials the Yld2000 [24] yield criterion was calibrated with its eight coefficients, $a_1 - a_8$, and flow exponent, *m*, listed in in Table 2-4. The corresponding yield surfaces are shown in Figure 2-2. The isotropic von Mises yield surface is a reasonable first-order approximation to the anisotropic yield surfaces for the steels considered.

Table 2-3 - Plastic Anisotropy of Studied Materials

590R	R_0	$R_{22.5}$	R_{45}	$R_{67.5}$	R_{90}	R_b
	0.67 ± 0.01	0.82 ± 0.01	1.08 ± 0.01	1.00 ± 0.01	0.9 ± 0.02	-
DP980	R_0	R_{15}	R_{30}	R_{45}	R_{60}	R_{75}
	0.78 ± 0.02	0.79 ± 0.02	0.86 ± 0.03	1.03 ± 0.01	0.96 ± 0.01	0.87 ± 0.03
	R_{90}	R_b				
	0.95 ± 0.01	0.84 ± 0.06				
3rd Gen 1180	R_0	$R_{22.5}$	R_{45}	$R_{67.5}$	R_{90}	R_b
	0.76 ± 0.01	0.83 ± 0.00	0.93 ± 0.00	0.90 ± 0.02	0.90 ± 0.01	0.92 ± 0.03

Table 2-4 – Yld-2000 Coefficients for Studied Materials

Material	Barlat Yld-2000 Calibration Coefficients								
	a_1	a_2	a_3	a_4	a_5	a_6	a_7	a_8	m
590R [22]	0.792	1.119	1.105	0.989	1.014	0.842	0.999	0.995	4.8
DP980 [25]	1.851	-0.455	-1.446	-1.025	-0.264	1.310	0.639	1.622	6.0
3rd Gen 1180 [20]	0.969	0.946	0.978	0.998	1.016	0.964	0.993	1.066	4.7

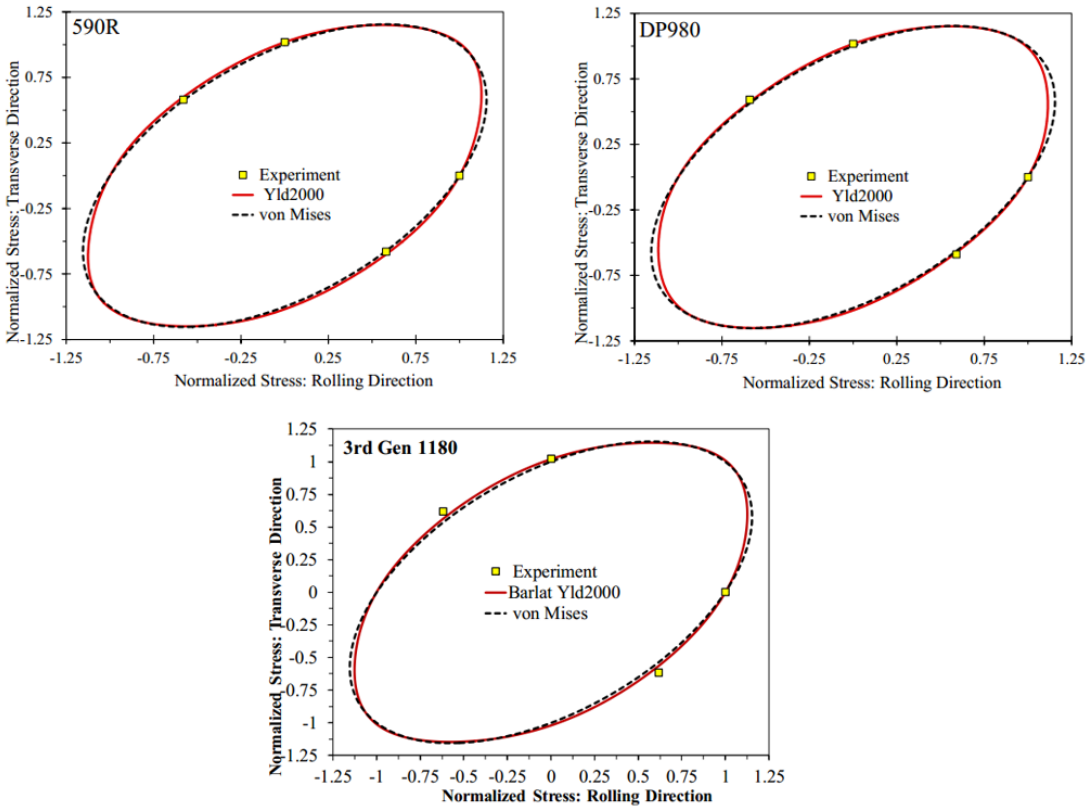

Figure 2-2 - Von Mises and Yld2000 yield surfaces for studied materials [20], [22]

2.2. In-plane FLC Experimental Setup and Results

Gutierrez et al. [20] performed Marciniak tests on the 3rd Gen 1180 and Noder et al. [22] performed Marciniak tests on the 590R and DP980. All tests were conducted at the University of Waterloo according to the ISO-12004-2 standard [8]. The experimental setup is shown below in Figure 2-3 which consists of an MTS hydraulic press system and DIC system. A schematic of the tooling used for the Marciniak experiments is shown in Figure 2-4.

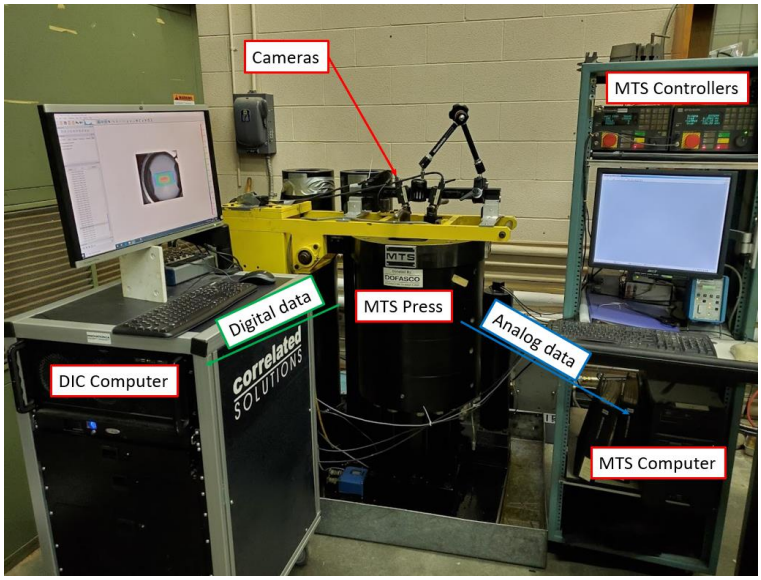

Figure 2-3 - Experimental setup of MTS press at the University of Waterloo

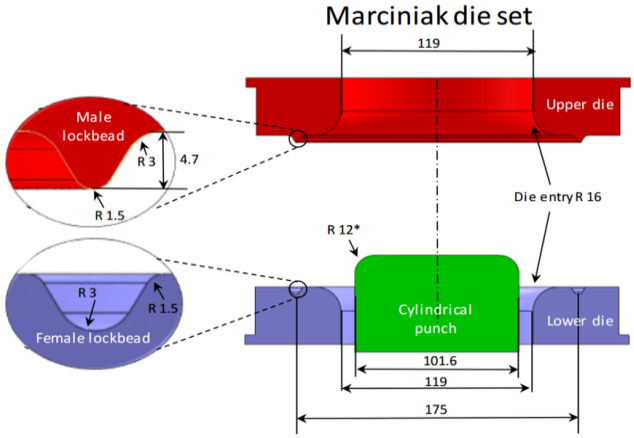

Figure 2-4 – Dimensions of Marciniak die set used to create in-plane FLCs by Noder et al. [22] **and Gutierrez et al. [20]**

The Marciniak FLCs are used to compare the efficacy of the equivalent in-plane FLC proposed by Min et al. [17]. The FLC created with the ISO method is shown below in Figure 2-5, however, the ISO method limit strains shown in Figure 2-5 should not be compared with LBF limit strains for the stretch bend experimental work completed in this thesis. The ISO limit strains are shown here for reference only.

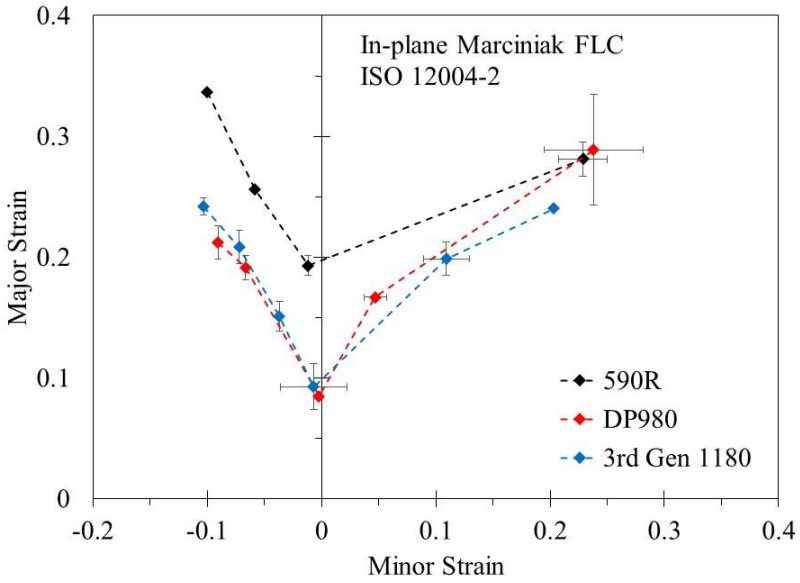

Figure 2-5 - Marciniak FLCs for studied materials [20], [22]

The mod. LBF limit strains for the 590R and 3rd Gen 1180 on the draw-side of the FLC were provided in a private correspondence from Gutierrez [26] and are shown below in Figure 2-6; these limit strains are used for comparison with the ASBT limit strains (Section 4). LBF limit strains for the DP980 were not available thus any comparison to the in-plane FLC for the DP980 uses the data shown in Figure 2-5.

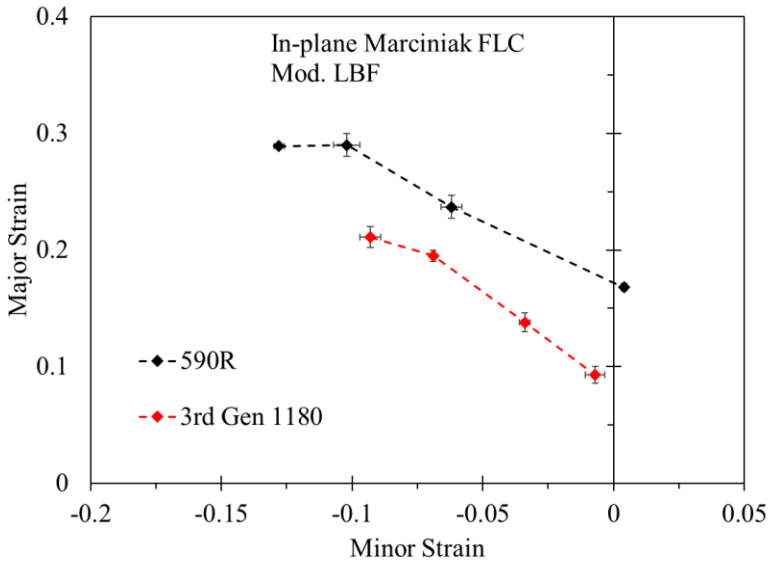

Figure 2-6 - LBF limit strains for 590R and 3rd Gen 1180 [26]

2.3. ASBT Experimental Setup

The ASBT experiments were conducted using the same MTS hydraulic press and DIC system setup shown in Figure 2-3. The stretch bend tool set (detailed in Chapter 3) was installed in the MTS hydraulic press. The DIC camera had a lens with a focal length of 17 mm. The MTS press was set to clamp the sample with 640 kN of force, and the punch speed was set to 0.25 mm/s for all tests.

The samples were spray painted to produce a black and white speckle pattern for DIC strain measurement. The paint used was Painter's Touch® multi-purpose spray paint manufactured by RUST-OLEUM. An example of a painted speckle pattern is shown in Figure 2-7.

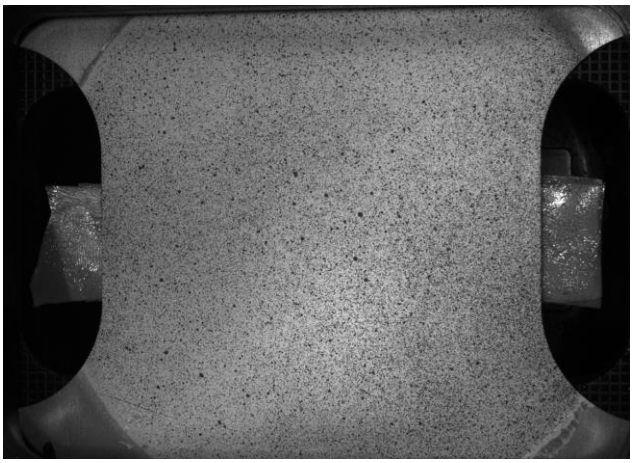

Figure 2-7 - Example of a speckle pattern on a 590R sample with Teflon beneath (10 mm punch below Teflon not visible)

The bottom of the sample and top surface of the punch were lubricated with polytetrafluoroethylene (PTFE) spray for each experiment. Additionally, similar to the method outlined in the ISO-12004-2 [8], layers of Teflon cut to a size slightly larger than the punch and petrolatum were sandwiched together and placed between the punch and the sample for each experiment. The Teflon strips between the punch and sample are visible in Figure 2-7 at the edge of the sample and outward.

2.4. DIC Parameters

The stereoscopic DIC system for all experiments consisted of two cameras and VIC-3D software. Full-field strain measurements were obtained using the DIC system and the relevant DIC parameters are shown in Table 2-5. The frame rate was set to obtain at least 500 images per test.

The image resolution for the 590R experiments was 0.057 mm/pixel and the image resolution for the DP980 and 3rd Gen 1180 experiments was 0.047 mm/pixel. The virtual strain gage length (VSGL) was determined by

$$VSGL = resolution \times step \times filter \tag{2.4.1}$$

A summary of the DIC parameters for each material tested is shown in Table 2-5. The VSGL was set to approx. 1.1 mm by altering the step and filter size to remain consistent with in-plane experimental data [20], [27] from the same lots of material used in this work. The subset size was 29-35 pixels in all tests.

Table 2-5 - DIC parameters for experiments by material

	Frame rate (frames per second)	Resolution (mm/pixel)	Strain filter	Step size (pixels)	VSGL (mm)
590R	7	0.057	4	5	1.1
DP980	15	0.047	5	5	1.1
3rd Gen 1180	25	0.047	5	5	1.1

2.5. Application of the LBF Method

Noder et al. [10] proposed a modified time dependent limit strain detection method based on the linear best-fit (LBF) method of Volk and Hora [9] and applied it to V-bend experiments. The amount of bending in the ASBT is less than a V-bend test, hence the modified LBF method was selected to determine the experimental limit strains in this thesis. The method proposed by Noder et al. [10] is henceforth referred to as 'LBF' in this thesis. The ISO method was not used due to the severe strain gradient perpendicular to the neck present in high bend severity stretch bend experiments. An example of the ISO method applied to a stretch bend experiment from this thesis is shown in the Appendix.

To obtain the strain data required for the LBF method, a circle inspector with a radius of 0.5 mm (approx.) is centred at the location of maximum major strain one image prior to fracture. An example of the circle inspector centred around the maximum major strain location just prior to fracture in VIC-3D is shown in Figure 2-8.

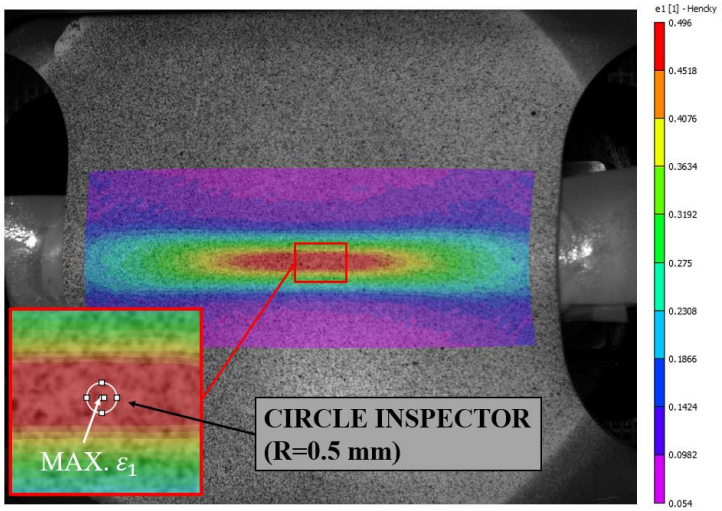

Figure 2-8 - Example of circle inspector in VIC-3D software (image just prior to fracture)

The experimental work involved several different bend severities where in some cases the sample would abruptly fracture while in others, hairline cracking on the surface was evident before rupture. A case showing hairline cracking prior to rupture is shown below in Figure 2-9.

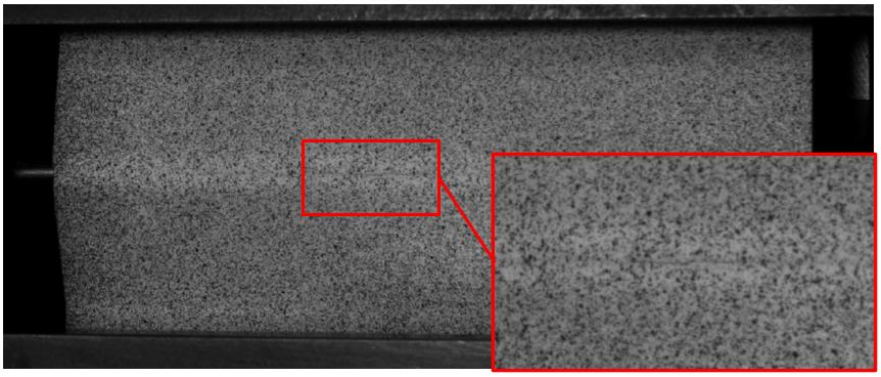

Figure 2-9 – Visible hairline crack observable in an ASBT, data processing terminated one image prior (590R, die gap width = 30 mm, punch radius = 1 mm)

3. Angular Stretch Bend Test

This chapter summarizes the development of the stretch bend die-set, testing and analysis. The objectives of the chapter are:

1) Evaluate the new die-set and observe the effect of altering the die gap width. The 590R steel was used across a wider range of bend severities and die gap widths for this purpose
2) Characterize the influence of the bend severity (t/R) on formability in stretch bending
3) The test data for the 590R will be used in Chapter 4 to aid in the validation of a model to estimate the sheet thickness using surface strain and geometry measurements.

3.1. Design of the Angular Stretch Bend Tooling

The ASBT tooling was designed with an emphasis on plane strain stretch bending of sheet metal to evaluate the shift of the FLC_0 as a function of bend severity (t/R). The ASBT tooling uses interchangeable cylindrical punches and variable die gap widths to control the amount of stretching. The die set was knurled in the clamping area avoid draw-in to simplify the boundary conditions in the finite-element model of the test. Lockbeads are effective and commonly used in this type of tooling but complicate the boundary condition and require a fine mesh to properly model the lockbead closure.

The die gap width can be modified using the interchangeable inserts shown in Figure 3-1. Three insert sizes were selected based upon the range of sizes reported in the literature which were: 30 mm, 51 mm, and 76.2 mm. The top die is shown in Figure 3-2 with and without the insert installed. All the inserts have an entry radius of 10 mm. Schematics of the top and bottom die are shown in Figure 3-3.

Figure 3-1 - Upper die inserts from left to right: 30, 51, 76.2 mm

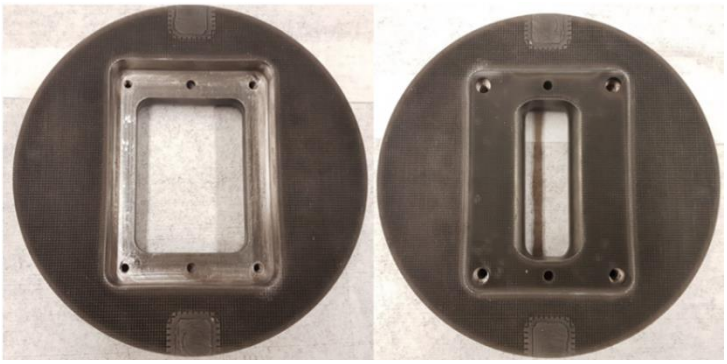

Figure 3-2 - Upper die without insert (left) and with 30 mm insert (right)

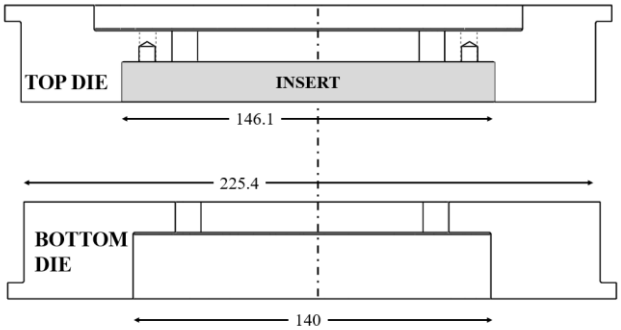

Figure 3-3 – Schematic of top and bottom die (cross-section view) of new stretch bend tooling, dimensions in mm

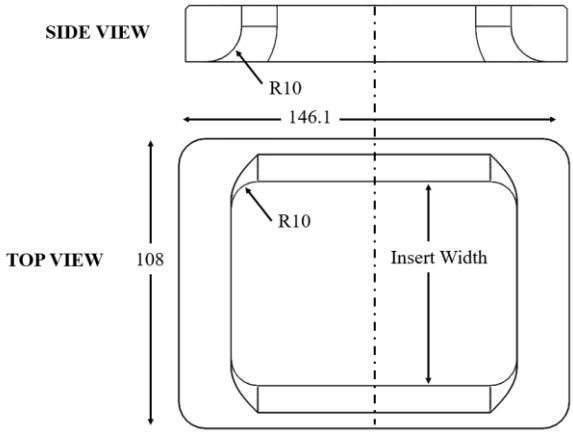

Figure 3-4 - Schematic for top die insert, dimensions in mm

The surface knurling was machined according to the dimensions shown in Figure 3-5. The dies and inserts were made of 4140 steel and case-hardened to a hardness of 55-60 HRC using plasma ion nitriding for a depth of hardening of up to 0.76 mm (0.30 inches).

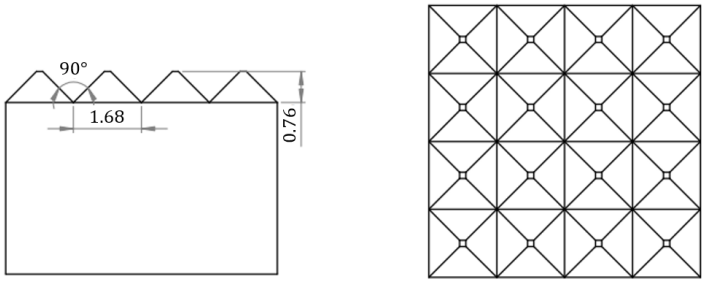

Figure 3-5 - Stretch bend die surface knurling detail (all dimensions in mm)

The cylindrical punches are interchangeable by means of a punch platform connected to the load cell assembly to ensure consistent punch placement. The punch platform and ASBT punches used are shown in Figure 3-6.

Figure 3-6 – ASBT punch platform (left) and punches with radius of (left to right): 1, 5, 10, 15 mm

3.2. Sample Geometry and Test Conditions

Two types of sample geometries were used for each material that conform to the ISO-12004 standard [8] and are denoted by their gage width. The 25.4 mm sample geometry is shown in Figure 3-7a, and the 76.2 mm sample geometry is shown in Figure 3-7b.

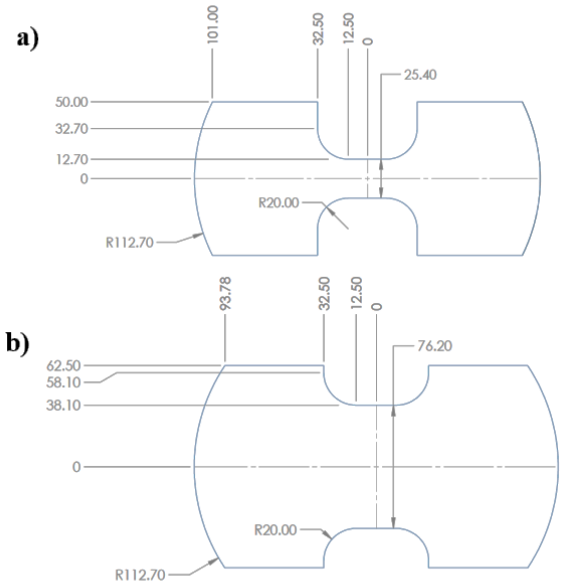

Figure 3-7 - Sample geometry a) 25.4 mm (1 inch) b) 76.2 mm (3 inch)

A variety of punch sizes and gap widths were considered for a given bend severity. The 590R was used to evaluate the tooling across a wide range of conditions due to its combination of

moderate strength and ductility. The 3rd Gen 1180 and DP980 tests were performed after the initial study with the 590R. The test conditions are summarized in in Table 3-1 and Table 3-2.

Table 3-1 - List of test conditions for the 76.2 mm sample geometry

Gap width (mm)	Punch radius (mm)	590R	DP980	3rd Gen 1180
30	1	✓	✓	✓
30	5	✓		
30	10	✓		
51	1	✓		
51	5	✓		
51	10	✓		
76.2	1	✓		
76.2	5	✓		
76.2	10	✓		

Table 3-2 - List of test conditions for the 25.4 mm sample geometry

Gap width (mm)	Punch radius (mm)	590R	DP980	3rd Gen 1180
30	1	✓		
30	10	✓		
51	5		✓	✓
51	15		✓	✓
76.2	1	✓		
76.2	10	✓		

3.3. Experimental Results – Strain Paths and Limit Strains

The strain paths and limit strains for the 590R tests with the 76.2 mm width geometry can be seen in Figure 3-8 where the limit strains are similar in magnitude for all conditions. The strain paths appeared to be governed by the nominal t/R ratio while the gap width had a negligible influence.

Non-linearity of the strain path appeared to increase with the punch size as the level of bending decreases and stretching increases. The strain paths produced with the 1 mm punch deviate from

plane strain (toward a uniaxial tension strain path) but are relatively linear. The strain paths produced with the 5 mm punch show similar deformation to the 1 mm punch until about 0.2 major strain (approximately 2/3 of the major limit strain) and then transitioned to a strain path similar to uniaxial tension. After the limit strain was reached, the strain path transitions to plane strain as the incremental minor strain, $d\varepsilon_2$, approaches zero.

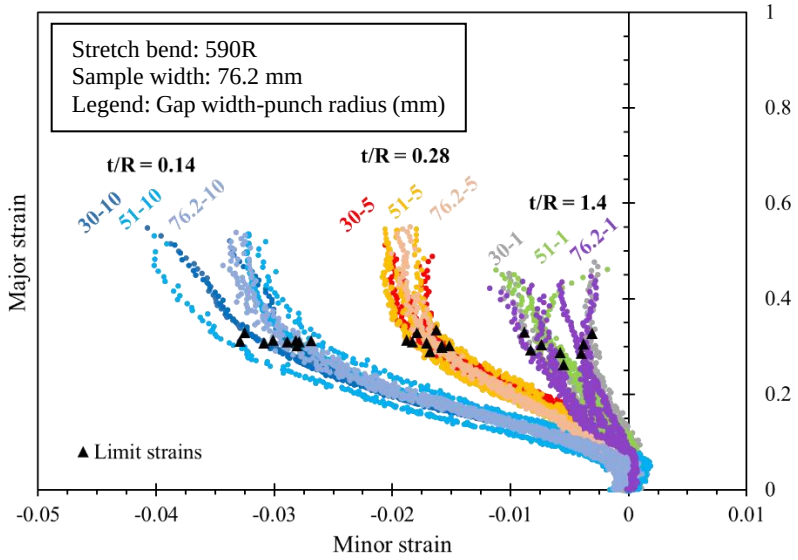

Figure 3-8 - 590R strain paths and LBF limit strains, 76.2 mm sample. Each punch radius and die gap combination is denoted. '30-10' indicates a 30 mm die gap and 10 mm radius punch.

The strain paths and limit strains 590R steel using the narrower 25.4 mm width are shown in Figure 3-9. As with the 76.2 mm width geometry, the strain paths are grouped by the t/R ratio. The amount of non-linearity in the strain paths is higher with the larger punch size, as the initial deformation is similar between both bend severities.

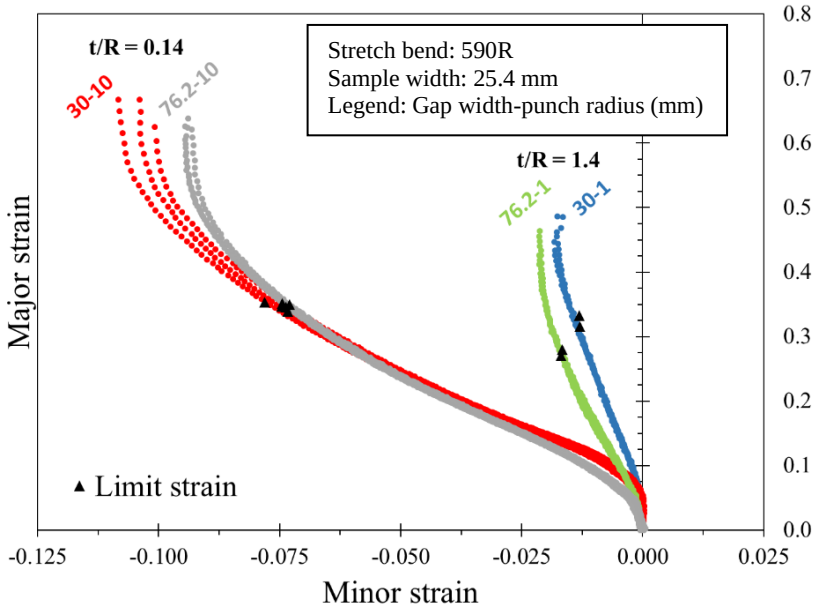

Figure 3-9 - 590R strain paths and LBF limit strains, 25.4 mm sample

The strain paths and limit strains of the DP980 for the 25.4 and 76.2 mm width samples are shown in Figure 3-10 and Figure 3-11 respectively. Note the t/R are different from that of the 1.4 mm thick 590R since the sample thickness of the DP980 is 1.2 mm. Qualitatively, the same trends in the strain path and limit strains with the punch radius and sample width were observed for the DP980.

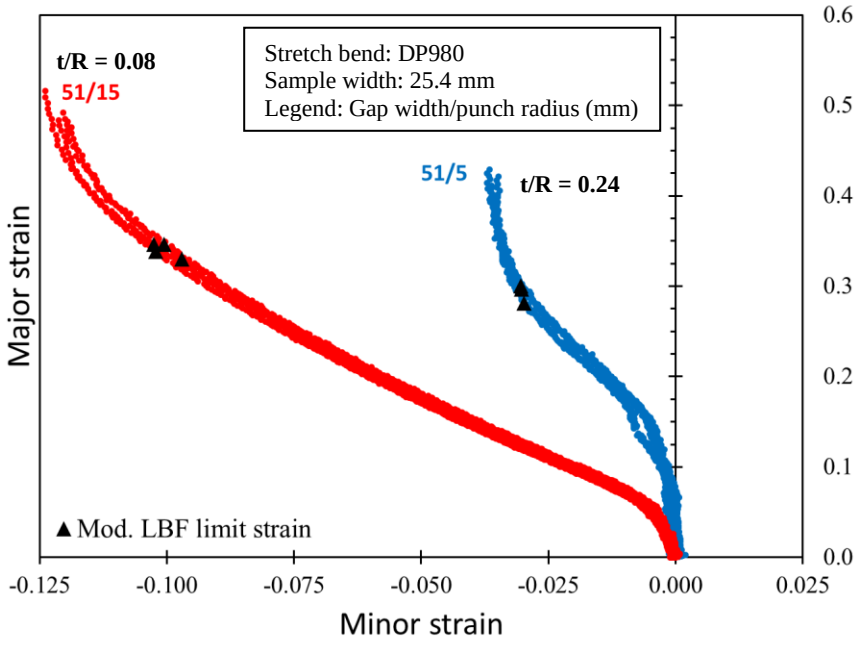

Figure 3-10 - DP980 strain paths and LBF limit strains, 25.4 mm sample

For the 25.4 mm samples of DP980 shown in Figure 3-10, the strain path produced with the 5 mm radius punch shows an initial phase of near plane strain deformation, followed by a shift towards the uniaxial stretching and then a shift back towards plane strain during localization. The observed strain path using the 15 mm radius punch ($t/R = 0.08$) exhibited a smaller region of approximate plane strain deformation before it transitioned towards uniaxial tension. The initial plane strain deformation is attributed to approximate plane strain bending of the sample as it conforms to the cylindrical punch geometry followed by stretch-dominated conditions.

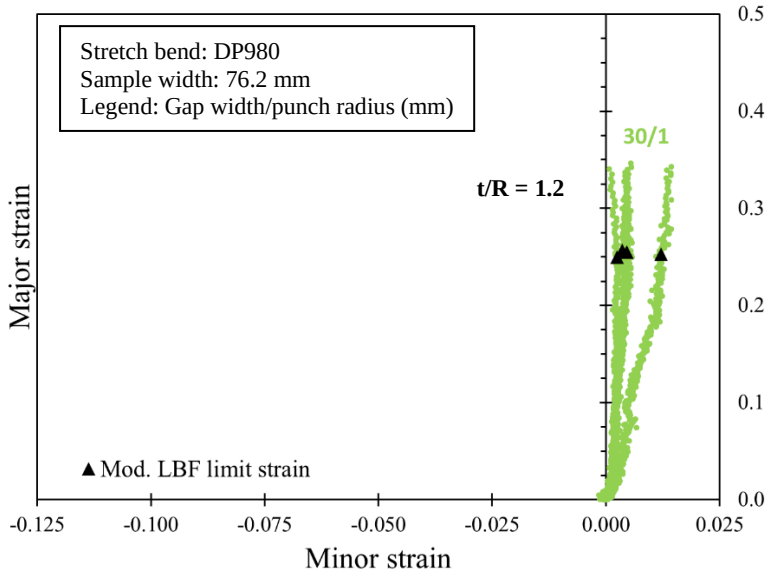

Figure 3-11 - DP980 strain paths and LBF limit strains, 76.2 mm sample

The strain paths and limits strains for the 3rd Gen 1180 steel using the 25.4 mm and 76.2 mm width sample geometries are shown in Figure 3-12 and Figure 3-13. The 25.4 mm samples tested at a bend severity of 0.28 and 0.093 both showed a similar degree of non-linearity in the strain paths as seen in the 590R and DP980.

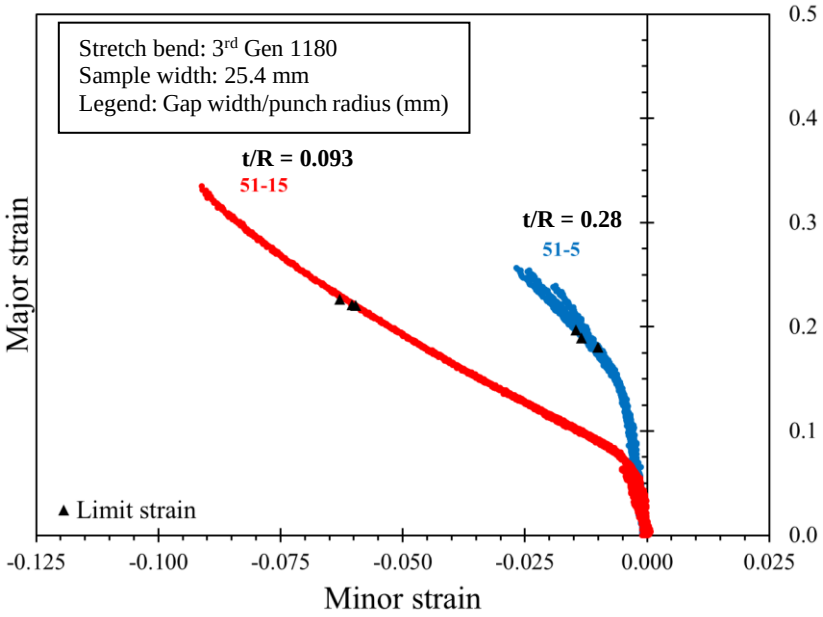

Figure 3-12 - 3rd Gen 1180 strain paths and mod. LBF limit strains, 25.4 mm sample

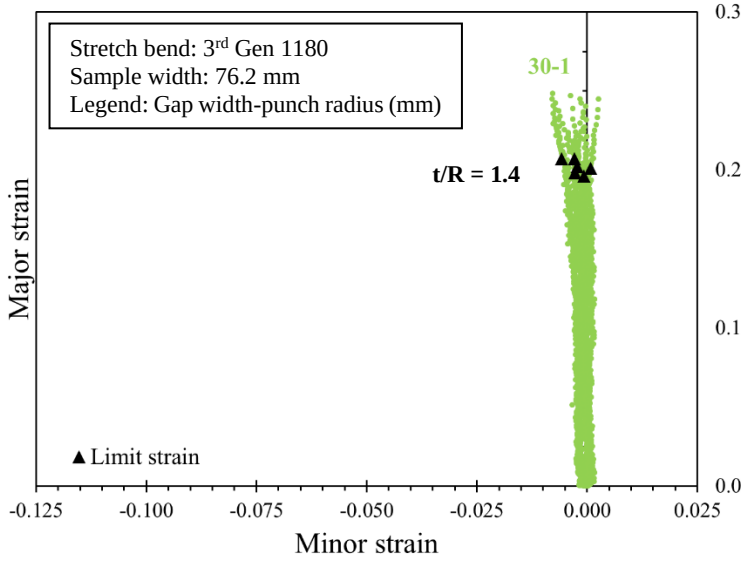

Figure 3-13 - 3rd Gen 1180 strain paths and mod. LBF limit strains, 76.2 mm sample

3.4. Influence of Die Gap

It was expected that the die gap width would show a marked effect on the limit strains as a smaller gap was though to promote a higher degree of bending earlier in the test. However, the influence of the die gap width upon the limit strains appears to be inconclusive based on the results

shown in Section 3.3. To investigate the effect of the die gap on the limit strains further, the standard deviation across gap sizes (i.e. t/R constant) was compared to the standard deviation for each test condition (averaged). If the influence of the die gap is significant, there will be a significant difference in the two standard deviations for each t/R. The average S.D. was calculated using the formula

$$Average\ S.D. = \sqrt{\left(\sum_{i=1}^{n} s_i^2\right) \Big/ n} \tag{3.4.1}$$

where *n* represents the total number of standard deviation values, and *s* represents the S.D. of a test condition. The tabulated results are shown in Table 3-3, where ε_1^* denotes the major limit strain.

Table 3-3 - Major limit strain averages and standard deviations (590R, 76.2 mm sample)

		30 mm gap	51 mm gap	76.2 mm gap	S.D	Average S.D.
$t/R = 1.4$	Average ε_1^*	0.290	0.278	0.301	0.0115	-
	S.D. ε_1^*	0.0255	0.0134	0.0064	-	0.0170
$t/R = 0.28$	Average ε_1^*	0.294	0.319	0.310	0.0127	-
	S.D. ε_1^*	0.0075	0.0140	0.0128	-	0.0118
$t/R = 0.14$	Average ε_1^*	0.316	0.312	0.309	0.0035	-
	S.D. ε_1^*	0.0120	0.0008	0.0057	-	0.0077

As shown in Table 3-3, the S.D. across gap size was similar to the averaged S.D. for each test condition. The absolute value of the difference between the two standard deviation values in Table 3-3 are 0.0055, 0.0009, and 0.0042 for t/R of 1.4, 0.28, and 0.14 respectively. The effect of the die gap width is negligible on the major limit strains since the differences in the standard deviations of the major strain were 0.0055 or lower.

The load-displacement response of the 590R was then used as a second metric to evaluate the influence of die gap width. For the 590R with the 76.2 mm width sample geometry, the bend severity ranged from 0.14 to 1.4. The representative load vs. displacement responses for the low and high bend severity test conditions for all three gap widths are shown in Figure 3-14 and Figure 3-15 up to when the limit strain was detected.

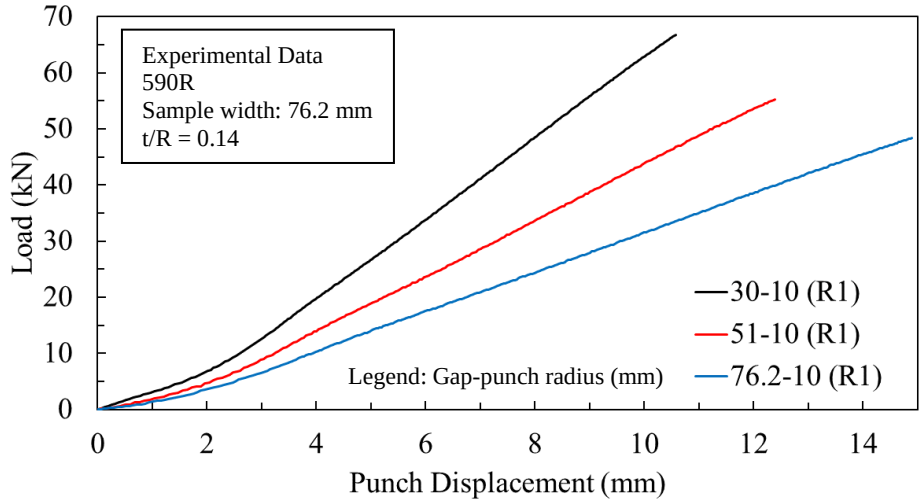

Figure 3-14 - Load vs. displacement for different gap widths at the same t/R, 590R, 76.2 mm sample, t/R = 0.14

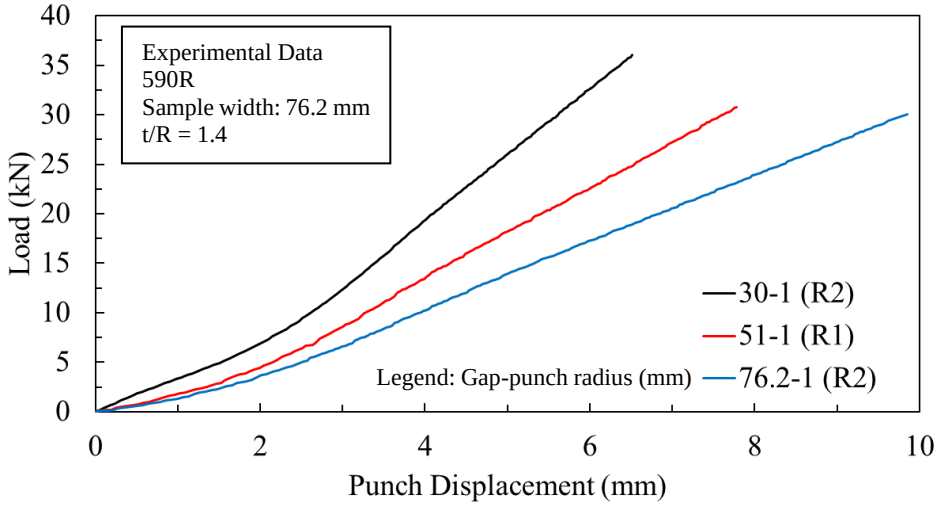

Figure 3-15 - Load vs. displacement for different gap widths at the same t/R, 590R, 76.2 mm sample, t/R = 1.4

A clear trend is observed for both bend severities. As the gap width decreased, the load increased which should also translate to an increase in the local tool contact pressure. The same trend can be seen in in Figure 3-16 for the 590R using the 25.4 mm width samples with a bend severity of 0.14. Furthermore, the same behavior was observed in the 3rd Gen 1180 and DP980 steels.

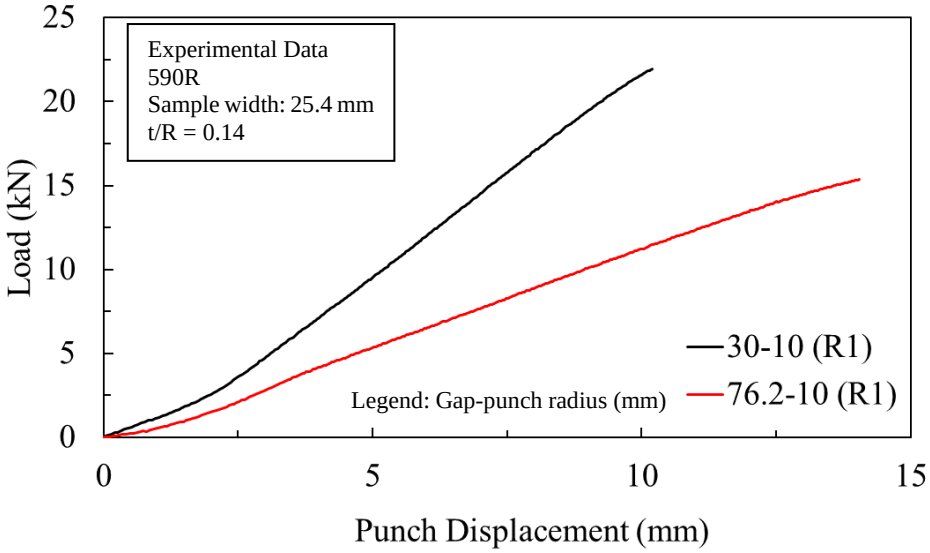

Figure 3-16 - Load vs. displacement for different gap widths. 590R, 25.4 mm sample, t/R = 0.14

The influence of the gap width on the force-displacement was clear although its effect on the limit strains appeared to be negligible, at least for the bend severities considered in the 590R experiments using the 76.2 mm sample. Although it was hoped that the die width would enable a larger range of test conditions for formability characterization, it is still a positive outcome. The ASBT geometry is not standardized and thus the marginal influence of die gap supports the transferability of limit strains between labs and test fixtures. When selecting a gap width, it appears beneficial to select the gap width that is best suited to the finite-element modelling strategy where a larger gap is more amenable to using shell elements that are used by tool and die engineers in industry.

4. Investigation of Analytical Models to Produce Equivalent In-plane Limit Strains

In this chapter the FLC process correction models of Min et al. [17] to account for curvature, non-linear strain path, and tool contact pressure are applied to the stretch bend limit strains for the 590R, 3rd Gen 1180, and the DP980. The corrected stretch-bend limit strains are then compared with the in-plane limit strains obtained by Gutierrez et al. [20] and Noder et al. [22].

4.1. Curvature of the Convex Surface

The major and minor curvatures on the convex (outer surface) of the ASBT specimen were calculated from the DIC surface data to estimate the strain due to bending. Min et al. [17] recommended extracting data along a line with a length of 20 mm based on an analysis of Nakazima tests with punch radii of 25 and 50 mm. The length of the lines is henceforth referred to as the 'fitting window' with an example of the two lines drawn in VIC-3D software in Figure 4-1. The curvature was calculated using DIC data extracted at 0.5 mm increments along the line.

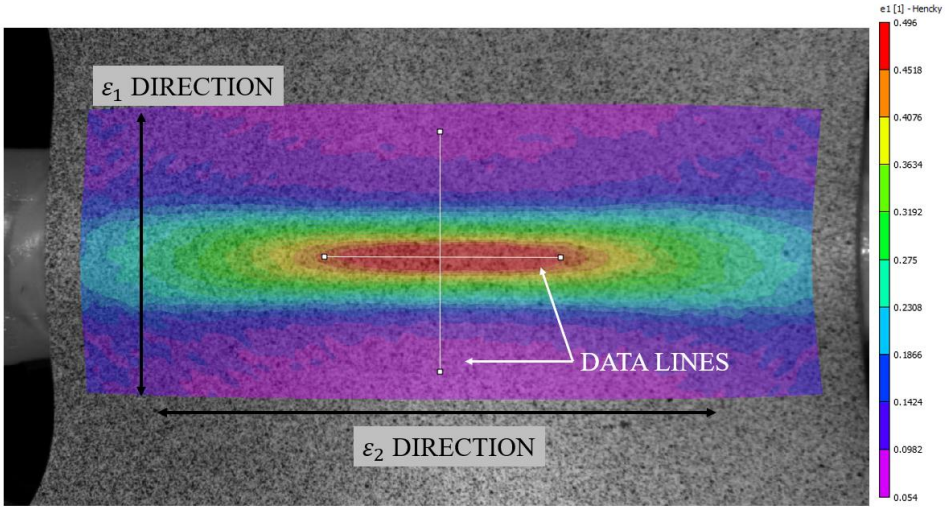

Figure 4-1 - Example of curvature line extraction in VIC-3D software (image just prior to fracture)

For each image, the surface coordinate data was fit using a parabolic equation (5.1.1) and then differentiated to obtain the radius of curvature (5.1.2):

$$z = a + bx + cx^2 \tag{4.1.1}$$

where z is the out-of-plane coordinate and x is the arc length along the line slice and a, b, and c are the coefficients. The curvature, κ, and radius of curvature, R, on the convex surface are:

$$\kappa = \frac{2c}{\left[1+\left(b+2cx\right)^2\right]^{3/2}};\ R = \frac{1}{\kappa}. \tag{4.1.2}$$

The radius of curvature along with the surface strain data will be used in Section 4.2 to estimate the actual thickness of the sheet during stretching and bending.

4.2. Instantaneous Thickness Models

In this section a new model is proposed to estimate the sheet thickness during plane strain stretch bending and compared with the curvature method of Min et al. [17] . The two thickness models were evaluated using data from interrupted stretch bend tests of the 590R steel.

4.2.1. Background on Thickness Models in Literature

Measuring thickness in out-of-plane bending and stretching is challenging since the through-thickness strain gradient is not measured. Only the surface strains on the convex surface are measured with DIC and are only valid to estimate the thickness for in-plane deformation. Min et al. [28] proposed a model to estimate the thickness from surface DIC data. Min's model is based on an initial infinitesimal circular shell element which is shown in Figure 4-2a, with radius r_o, thickness t_o, and points A, A_1, A_2. After deformation the element becomes a 3D shell as shown in Figure 4-2b; the 3D shell in spherical coordinates (R, θ, φ) is shown in Figure 4-2d. The projection of the deformed element is shown in Figure 4-2c.

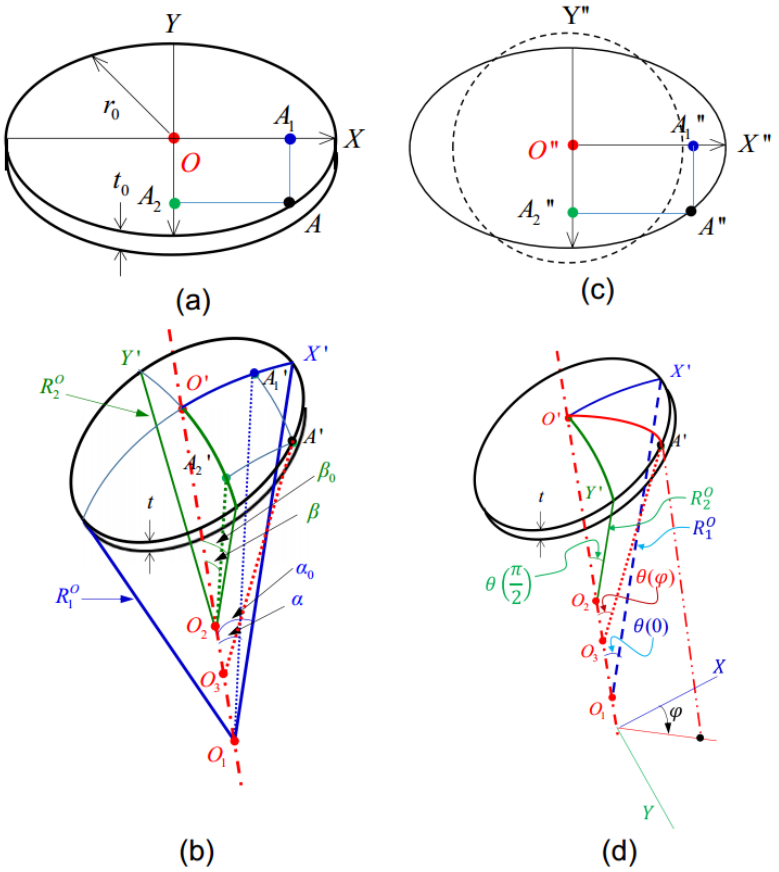

Figure 4-2 - Infinitesimal element used in Min et al. thickness model derivation [28]. (a) circular shell element (b) 3D deformed element (c) projection of the deformed element (d) deformed 3D shell element in spherical coordinates

The volume of the deformed element integrating with respect to R, α and β is

$$V_d = 4\int_{R^I}^{R^O}\int_0^{\alpha_o}\int_0^{\beta} R^2 d\beta d\alpha dR \tag{4.2.1}$$

The inner radius can be expressed as a function of the outer radius and thickness,

$$R^I = R^o - t \tag{4.2.2}$$

Using equations (4.2.1), (4.2.2) and integrating with respect to R:

$$V_d = \frac{\pi\alpha_o\beta_o}{3}t^3 - 4t^2\int_0^{\alpha_0}\int_0^{\beta} R^o d\beta d\alpha + 4t\int_0^{\alpha_0}\int_0^{\beta}\left(R^o\right)^2 d\beta d\alpha \tag{4.2.3}$$

To account for the volume change due to elastic strains,

$$V_d - V_o \exp\left(\varepsilon_V^e\right) = 0 \tag{4.2.4}$$

where ε_V^e is the volume elastic strain. Combining equation (4.2.3) and (4.2.4) leads to a cubic equation:

$$t^3 + \frac{a}{d}t^2 + \frac{b}{d}t + \frac{c}{d} = 0 \tag{4.2.5}$$

where

$$\begin{aligned} a &= -4\int_0^{\alpha_0}\int_0^{\beta} R^o d\beta d\alpha \\ b &= 4\int_0^{\alpha_0}\int_0^{\beta}\left(R^o\right)^2 d\beta d\alpha \\ c &= -\pi r_o^2 t_o \exp\left(\varepsilon_V^e\right) \\ d &= \frac{\pi\alpha_o\beta_o}{3} \end{aligned} \tag{4.2.6}$$

Eq. (4.2.5) and (4.2.6) must be solved using numerical integration. To obtain a more convenient solution method, Min et al. [28] then proposed a curvature-based model by applying constraints on the two outer surface curvatures R_1^o and R_2^o.

The curvature model is given by:

$$t^3 + \frac{a''}{d''}t^2 + \frac{b''}{d''}t + \frac{c''}{d''} = 0 \tag{4.2.7}$$

were

$$
\begin{aligned}
a'' &= -\frac{1}{2}\left[\begin{array}{c} 2\left(R_1^o + R_2^o\right)\exp\left(\varepsilon_1^o + \varepsilon_2^o\right) + \left(5R_1^o + R_2^o\right)\exp\left(2\varepsilon_1^o\right) \\ + \left(5R_2^o + R_1^o\right)\exp\left(2\varepsilon_2^o\right) \end{array}\right] \\
b'' &= R_1^o R_2^o\left[3\exp\left(2\varepsilon_1^o\right) + 3\exp\left(2\varepsilon_2^o\right) + 2\exp\left(\varepsilon_1^o + \varepsilon_2^o\right)\right] \\
c'' &= -8\left(R_1^o\right)^2\left(R_2^o\right)^2 t_o \exp\left(\varepsilon_V^e\right) \\
d'' &= \frac{1}{48R_1^o R_2^o}\left[\begin{array}{l} 2\left(5\left(R_1^o\right)^2 + 5\left(R_2^o\right)^2 + 6R_1^o R_2^o\right)\exp\left(\varepsilon_1^o + \varepsilon_2^o\right) \\ + \left(35\left(R_1^o\right)^2 + 3\left(R_2^o\right)^2 + 10R_1^o R_2^o\right)\exp\left(2\varepsilon_1^o\right) \\ + \left(35\left(R_2^o\right)^2 + 3\left(R_1^o\right)^2 + 10R_1^o R_2^o\right)\exp\left(2\varepsilon_2^o\right) \end{array}\right]
\end{aligned}
\tag{4.2.8}
$$

Min et al. [28] evaluated their models for a biaxial bulge test for two materials: AA5182-O and DP600. The models underpredicted the thickness by ~0.43% and ~1.2% for the AA5182-O and DP600 respectively. Min et al. [28] compared biaxial bulge thickness models in literature (Young et al. [29], Yoshida [30], ISO 16808 [31]) and the error ranged from 1.4% to 2.4% for AA5182-O and 1.1% to 2.1% for DP600 [28]. Elastic dilatancy was found to be negligible with both thickness models providing comparable results in bulge tests.

4.2.2. New Stretch Bend Thickness Model

The mapping-based approaches of Min et al. to estimate the thickness in bending are valid in a geometric sense but also do not account for the complex thinning response of the cross-section that emerges for significant plastic bending. The plastic response is complicated by the hardening response, shift of the neutral layer, kinematic hardening and tool contact pressure which all affect thinning of the cross-section. In the ASBT, deformation is dominated by plane strain tension and uses a cylindrical punch such that the lateral curvature is theoretically zero. The ASBT mechanics are favorable to develop a simple estimation of thinning of the cross-section denoted as the stretch

bend model (SB model). The SB model is also derived from geometrical considerations with a strip of material being deformed into a circular shape as shown in Figure 4-3.

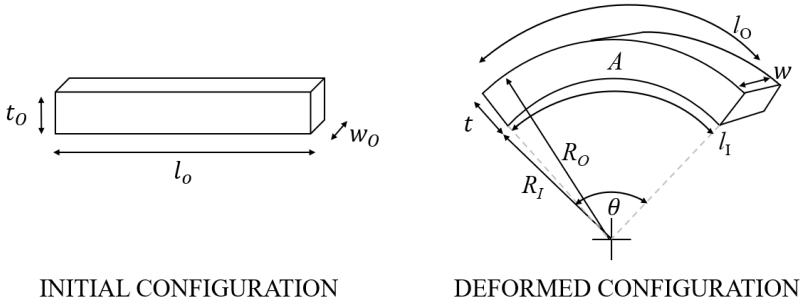

Figure 4-3 - Thickness model (SB model)

The rectangular element has initial dimensions of l_o, w_o, t_o and current dimensions of l_O, l_I, w, t (or A, w). The convex and concave layer lengths are denoted as l_o and l_I respectively. The radius of curvature of the convex and concave layer are denoted R_O and R_I respectively. The volume conservation of a rectangular element can be expressed as

$$l_o w_o t_o = Aw \tag{4.2.9}$$

Thus, the lengths of the convex and concave layers are:

$$l_O = R_O \theta \tag{4.2.10}$$

$$l_I = R_I \theta = \left(R_O - t\right)\theta \tag{4.2.11}$$

Note that the inner radius in Eq. (4.2.11) is expressed as $R_O - t$ since the thickness is assumed to be uniform over the bend. The area of the face *A* can be expressed as the difference in areas between the sector of the circle formed by radii R_I and R_O, with thickness *w:*

$$A = \left[\frac{1}{2}R_O^2\theta - \frac{1}{2}\left(R_O^2 - t\right)^2\theta\right]w \tag{4.2.12}$$

Lastly, substitution of Eq. (4.2.12) into Eq. (4.2.9)

$$l_o w_o t_o = \frac{\theta}{2}\left[R_O^2 - \left(R_O - t\right)^2 \right] w \tag{4.2.13}$$

Eq. (4.2.13) can be further simplified by assuming that the loading is proportional and the strain path is linear [32]. The major and minor strains on the convex surface are

$$\varepsilon_1 = \ln\left(\frac{l}{l_o}\right) \tag{4.2.14}$$

$$\varepsilon_2 = \ln\left(\frac{w}{w_o}\right) \tag{4.2.15}$$

Substituting Eq. (4.2.14) and Eq. (4.2.15) into equation (4.2.13) and using Eq. (4.2.10) to write θ in terms of R_O and l_O, a quadratic expression for the thickness is obtained

$$\frac{t^2 \exp\left(\varepsilon_1 + \varepsilon_2\right)}{2R_O} - t\exp\left(\varepsilon_1 + \varepsilon_2\right) + t_o = 0 \tag{4.2.16}$$

The average strains and thickness must be real numbers so the thickness is:

$$t = \frac{-\exp\left(\varepsilon_1 + \varepsilon_2\right) - \sqrt{\left(-\exp\left(\varepsilon_1 + \varepsilon_2\right)\right)^2 - \dfrac{2\exp\left(\varepsilon_1 + \varepsilon_2\right)t_o}{R_O}}}{\left(\dfrac{\exp\left(\varepsilon_1 + \varepsilon_2\right)}{R_O}\right)} \tag{4.2.17}$$

4.2.3. Evaluation of New Stretch Bend Thickness Model

To evaluate the accuracy of the thickness models, interrupted tests were performed for the 590R steel using the 76.2 mm wide specimen and the 15 mm radius cylindrical punch

$(t/R = 0.093)$. The major limit strain was expected to occur at approximately. $\varepsilon_1 = 0.3$ based upon the characterization in Chapter 3. The punch displacement corresponding to this strain level was identified and used as the upper limit for displacement in the hydraulic press. The local major strains at the apex of the test samples are shown in Figure 4-4 where the major strain ranged from approximately 0.15 to 0.23.

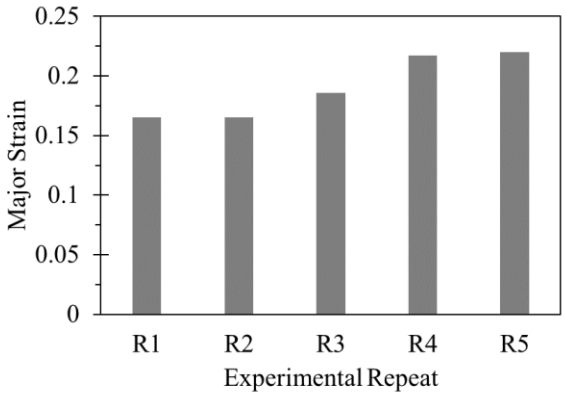

Figure 4-4 - Major strain at apex of sample extracted using a 0.5 mm diameter circle extractor tool

The samples were sectioned as shown in Figure 4-5 and the thickness was measured at the apex of the bend using a microscope. The SB model was then evaluated against the thickness measurements. An example of a microscope image is shown in Figure 4-6, where the thickness was measured along a line normal to the top surface.

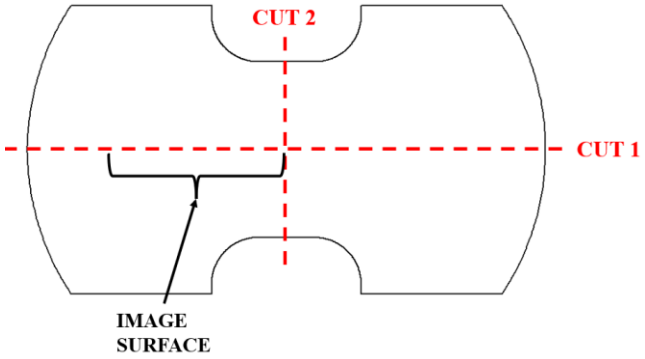

Figure 4-5 - Schematic illustrating how the samples were cut before viewing with the microscope

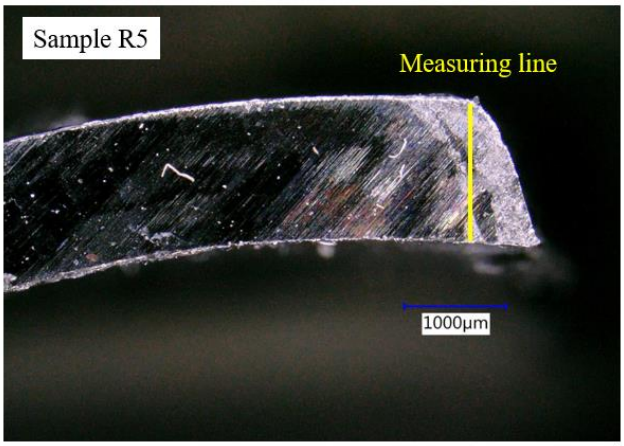

Figure 4-6 - Microscope image and measuring line of 590R sample R5

The comparison between the experimentally measured thickness, the SB model and Min's curvature method is shown in Figure 4-7. The tabulated results are shown in Table 4-1 where the percent difference was calculated using

$$\%Difference = \frac{|model - experimental|}{experimental} \times 100\% \tag{4.3.1}$$

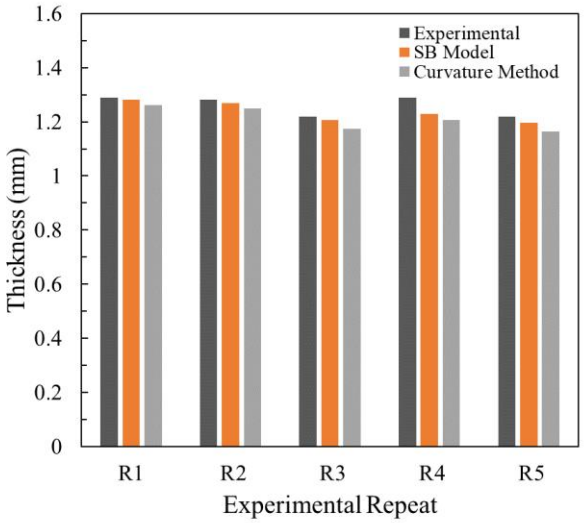

Figure 4-7 - Thickness comparison of 590R experiments, SB model, and curvature method

Table 4-1 - Tabulated comparison of 590R thickness tests, SB model, and curvature method

Repeat	R1	R2	R3	R4	R5	Average
Measured thickness (mm)	1.290	1.281	1.220	1.290	1.219	1.26
SB model thickness (mm)	1.282	1.270	1.206	1.230	1.120	1.22
Curvature method (mm)	1.261	1.250	1.175	1.206	1.164	1.211
% Difference (SB model)	0.63%	0.88%	1.12%	4.67%	1.87%	1.83%
% Difference (Curvature method)	2.27%	2.44%	3.67%	6.54%	4.55%	3.89%

As shown in Figure 4-7, there is good agreement between the experimentally measured thickness and the SB model, which is reflected in the small percent difference of 1.83% averaged across all tests. The more complex curvature method of Min et al. [28] was also accurate in the stretch bend tests where $t/R \geq 0.093$. The average percent difference between the curvature method and the experiments is 3.89%.

To observe the effect of the fitting window on the SB model, two additional fitting windows of lengths 5 and 10 mm were considered with the results shown in Figure 4-8. Decreasing the fitting window decreases the thinning predicted by the SB model, however, the final values for

thickness are quite similar for all fitting windows compared to the experiment. The maximum percent difference of the three curves in Figure 4-12 is on the order of 2%. Due to the low percent difference of the predictions with three different fitting windows the 20 mm fitting window was selected for consistency with the work of Min et al. [17].

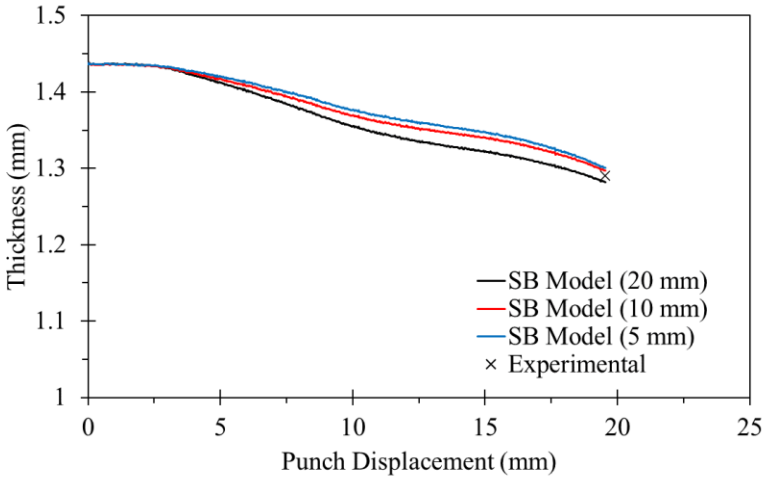

Figure 4-8 - Effect of fitting window on SB Model

4.3. Strain Path on Middle and Inner Layers of the Sheet

The concave side rule (CSR) is a postulate by Tharrett and Stoughton [12] which states that all through-thickness layers of the material must reach their respective limit strains before an acute neck can develop. The middle layer is the approximate neutral layer in stretch bending and thus primarily follows the in-plane FLC. The inner layer, or concave layer, is in contact with the punch and thus has compressive bending strains that delay instability along with the highest contact pressure.

Min et al. [17] proposed that the strain at any layer can be computed from the convex surface and current thickness using a projection of the convex strains. This is an idealization best suited for mild bending under stretch-dominated conditions as it does not account for the complex plastic response within the material during bending. In particular, it does not account for neutral axis

movement and biaxial shift of the strains at the concave layer due to the imposed compressive stress. The middle and inner layer strains are

$$\varepsilon_i^{mid} = \varepsilon_i^{outer} + \ln\left(1 - \frac{t\kappa_i^{outer}}{2}\right) \tag{4.3.2}$$

$$\varepsilon_i^{inner} = \varepsilon_i^{outer} + \ln\left(1 - t\kappa_i^{outer}\right) \tag{4.3.3}$$

The subscript i is either 1 or 2, representing major and minor directions respectively, t the thickness of the blank, and κ is the convex surface curvature measured using stereo DIC. Figure 4-9, Figure 4-10, and Figure 4-11 show the results of Eqs. (4.3.2)-(4.3.3) applied to selected experiments of the 590R material with bend severities of 1.4, 0.28 and 0.14 respectively. The strain paths were spline fit using a cubic piecewise spline to reduce noise. A comparison of the raw data and the spline fit is shown in the Appendix.

The strain path on the convex, middle and concave layers of the sheet are shown in Figure 4-9, Figure 4-10, Figure 4-11 for selected experimental repeats of the 590R at t/R of 1.4, 0.28, and 0.14 respectively. The higher bend severity of 1.4 produces a more severe strain gradient which is reflected by the larger difference in major strain magnitude on each layer relative to the lower bend severities of 0.28 and 0.14. Overall, the results do not appear to be reasonable as all layers are in tension for bend severities ranging from 0.14 to 1.4. Due to the relatively high bend severities in the ASBT, the inner layer was expected to be in compression in the early stages of deformation. Since the model cannot be experimentally verified, the strain projection model will be studied further with the aid of finite element simulation in Chapter 5.

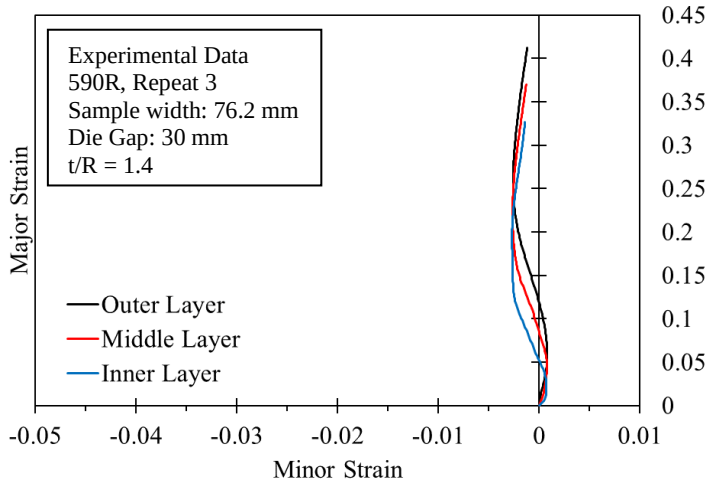

Figure 4-9 - Strain path on layers, 590R, 76.2 mm sample, t/R=1.4

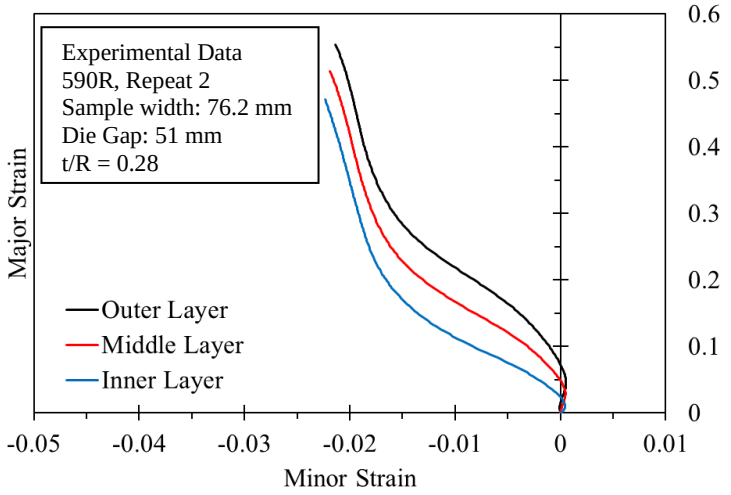

Figure 4-10 - Strain path on layers, 590R, 76.2 mm sample, t/R=0.28

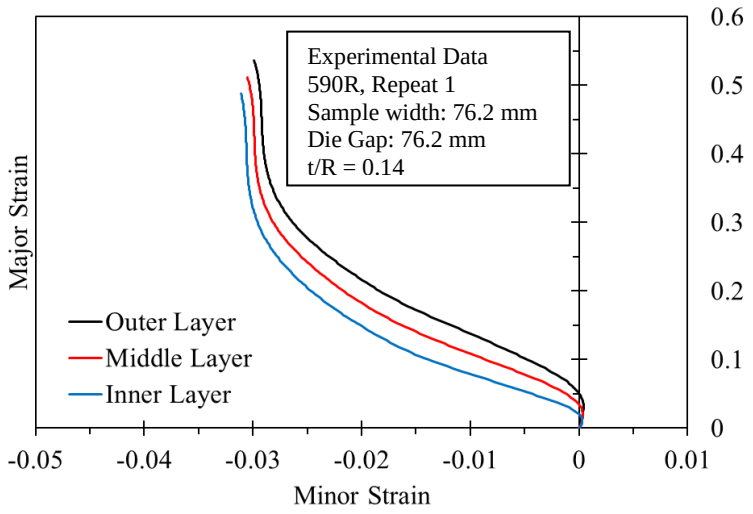

Figure 4-11 - Strain path on layers, 590R, 76.2 mm sample, t/R=0.14

4.4. Non-linear Strain Path (NLSP) Correction

The NLSP correction of Min et al. [17] was implemented in a MATLAB [33] script to post-process the DIC strain path data extracted at the necking location. The DIC strain data was downselected using a major strain increment, $\Delta\varepsilon_1 = 0.0005$, and then fit to a constrained spline using the SLM Toolbox [34] add-on within the MATLAB software. The spline was used to ensure that the thinning and major strain were always increasing during the test. The instantaneous strain path, $d\varepsilon_2/d\varepsilon_1$, was then extracted from the constrained spline and discretized in major strain increments of $\Delta\varepsilon_1 = 0.0025$.

As expected, the NLSP corrections did not play a significant role in correcting the ASBT limit strains since the strain paths were relatively proportional for the bend severities and sample widths considered in this thesis. The tabulated results for all materials and test conditions are provided in the Appendix. The following examples of the NLSP corrections are shown with the in-plane FLC produced using the modified maximum force criterion (MMFC) [35]. The 590R MMFC was evaluated by Noder et al. [22], the 3rd Gen 1180 was evaluated by Gutierrez et al. [20], and the

DP980 was evaluated by Noder et al. [18]. Additionally, corresponding experimental data from the Marciniak tests of Gutierrez et al. [20] and Noder et al. [22] are shown, denoted by the sample gage width.

In the following figures the limit strains are denoted by two numbers separated by a hyphen, denoting gap width and punch radius respectively. For example, ’30-1’ denotes the limit strain produced with a gap width of 30 mm and punch radius of 1 mm. The NLSP corrected limit strains are denoted as ‘NLSP’.

Shown in Figure 4-12 are the limit strains and the NLSP corrected strains for the 590R 76.2 mm samples with a bend severity of 1.4. The NLSP corrected limit strains show a negligible difference in major strain compared to the limit strains. The magnitude of the shift is on the order of 0.5% minor strain which is comparable to the variation in the limit strains.

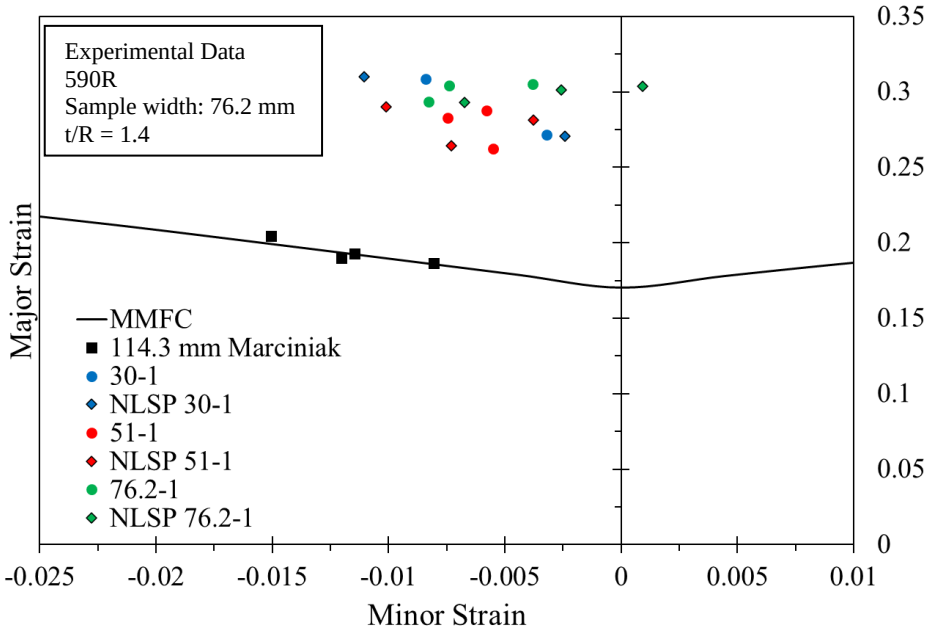

Figure 4-12 - 590R NLSP Corrections, t/R = 1.4, 76.2 mm sample

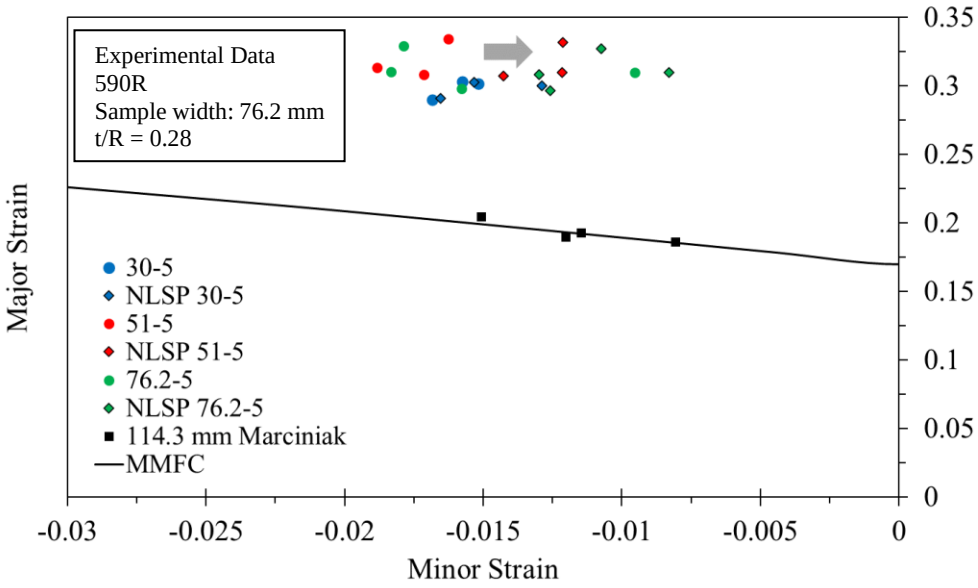

Figure 4-13 – 590R NLSP Corrections, t/R = 0.28, 76.2 mm sample – Arrow denotes general shift of limit strains after NLSP correction

For the 76.2 mm samples of 590R with a bend severity of 0.28, the limit strains are shifted to the stretch side of the FLC, whereas the NLSP corrections for the 0.14 bend severity produced a

larger shift as shown in Figure 4-14. Unlike the milder bend severity of 0.28, the limit strains are shifted by a similar amount regardless of gap width.

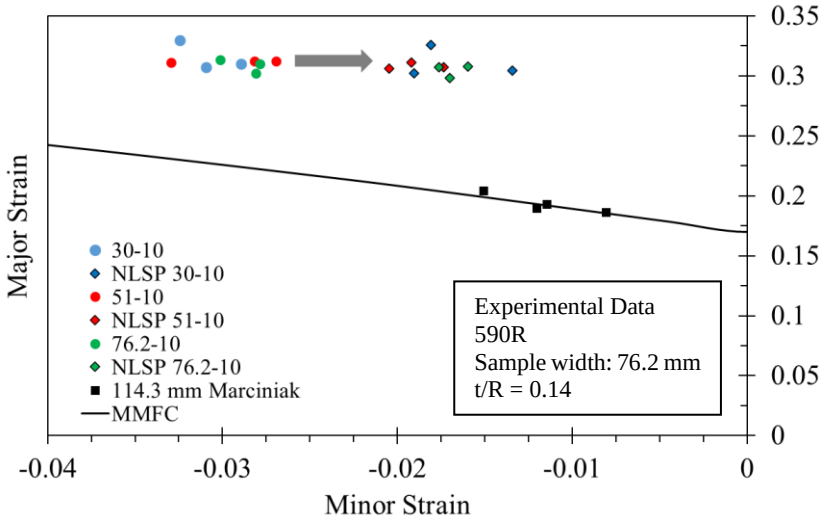

Figure 4-14 – 590R NLSP Corrections, t/R = 0.14, 76.2 mm sample – Arrow denotes general shift of limit strains after NLSP correction

The NLSP corrections applied to the 3rd Gen 1180 for the 76.2 mm width sample at a bend severity of 1.4 increased the variance in the minor strains as shown in Figure 4-15. No general trend in the shift was observed. Some limits strains were shifted toward the stretch-side, and other towards the draw-side. Even with the added variance it is important to note that the magnitude of the change in minor strain is still relatively small. The largest shift in minor strain was 2%.

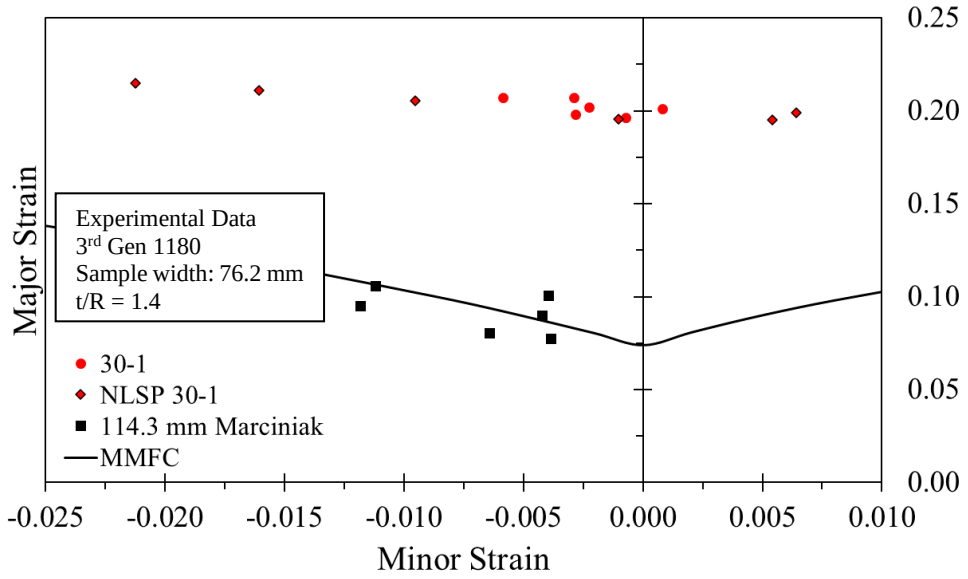

Figure 4-15 - 3rd Gen 1180 NLSP Corrections, t/R = 1.4, 76.2 mm sample

The NLSP corrected limit strains for the 3rd Gen 1180 using the 25.4 mm width are shown in Figure 4-16 for bend severities of 0.28 and 0.093. The corrected limit strains are shifted towards the draw-side of the FLC but the overall magnitude of the shift is minor as observed with the 76.2 mm width geometry. Overall, it is unclear whether the NLSP corrections for the 3rd Gen 1180 provides any value due to the dispersion in the data.

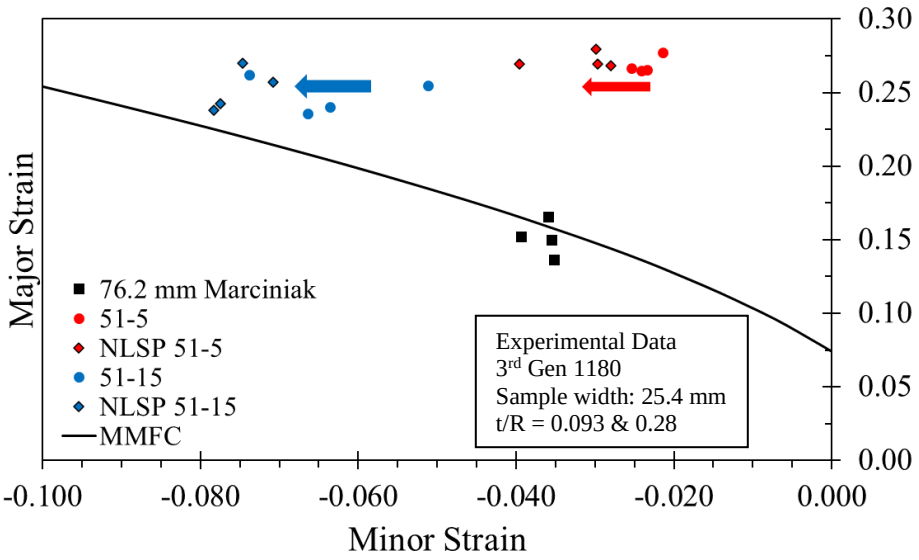

Figure 4-16 - 3rd Gen 1180 NLSP Corrections, 25.4 mm sample – Arrow denotes general shift of limit strains after NLSP correction

The NLSP corrections for the DP980 using the 76.2 and 25.4 mm width tests are shown in

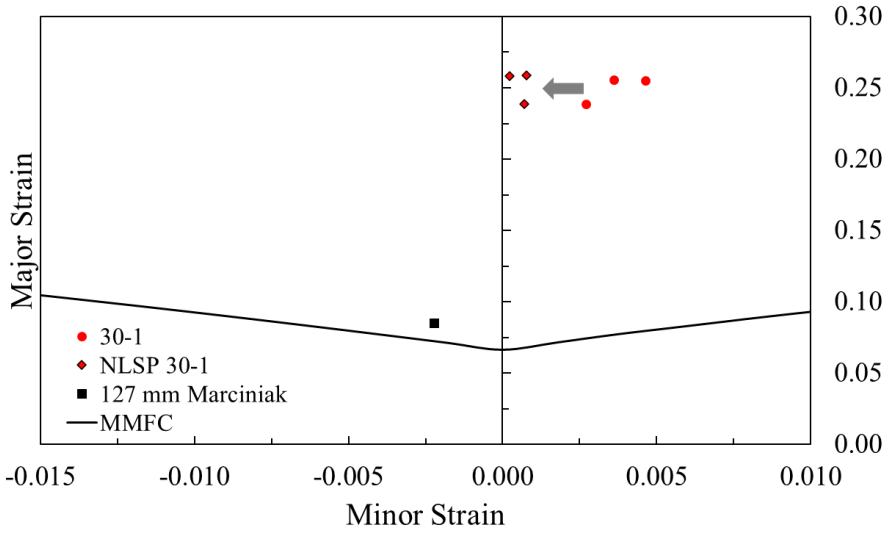

Figure 4-17 and Figure 4-18, respectively. For the 76.2 mm width sample with a bend severity of 1.4, there is a clear shift of the limit strains after the NLSP correction to the draw-side of the FLC. The 25.4 mm width samples with a bend severity of 0.093 show a shift towards the stretch-side of the FLC. The samples with a bend severity of 0.28 show the opposite trend with a shift towards

plane strain. This is attributed to the limit strain being ‘late’ to identify the neck in this formation with the strain path already changing towards plane strain.

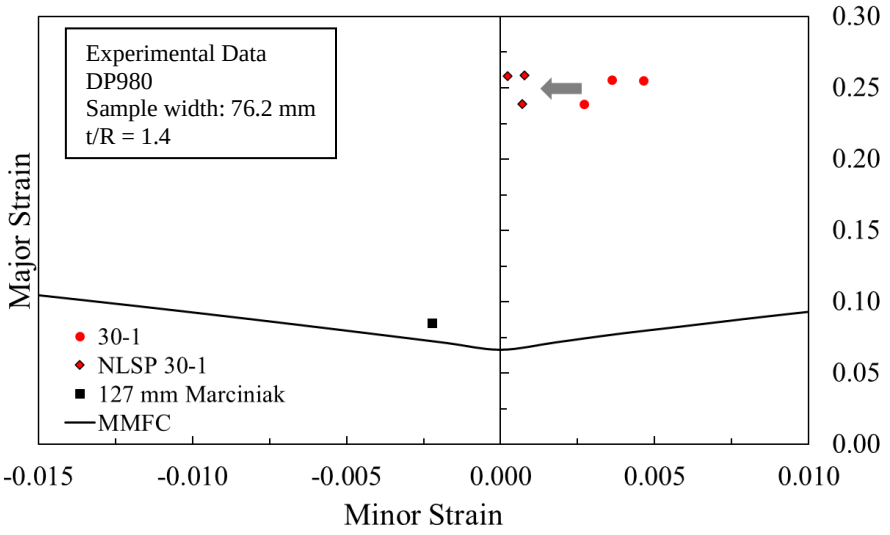

Figure 4-17 - DP980 NLSP corrections, t/R=1.4, 76.2 mm sample - Arrow denotes general shift of limit strains after NLSP correction

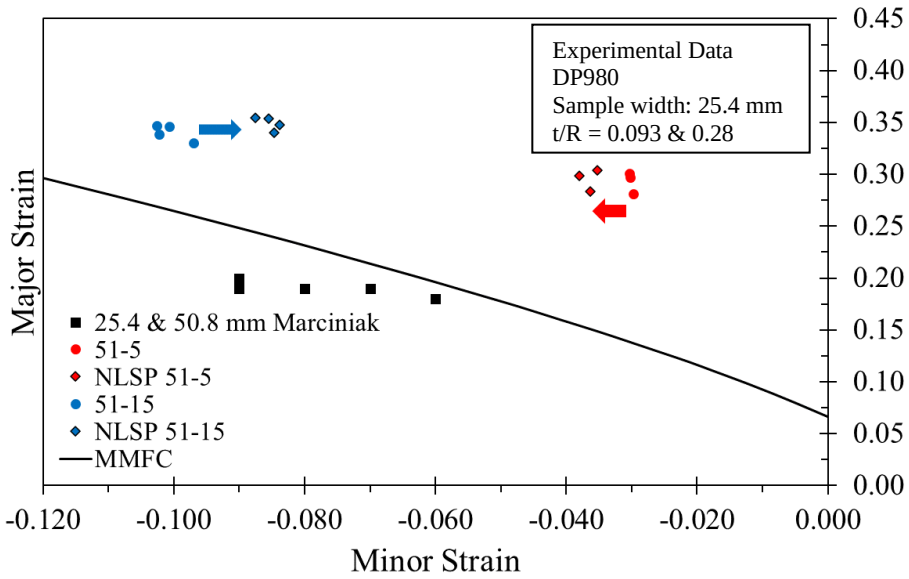

Figure 4-18 -DP980 NLSP corrections, t/R=0.093 & 0.28, 25.4 mm sample - Arrows denote general shift of limit strains after NLSP correction

In conclusion, the NLSP correction in the ASBT appears to play a secondary role with the magnitude of the shift being on the order of 2% minor strain or less for the materials considered.

Aside from the additional data processing required, the NLSP corrections are not without their own assumptions and can be very sensitive to the limit strain detection method employed and post-processing of the strain data. Ultimately, it is the decision of the analyst to decide whether the NSLP and its related uncertainty is worth the potential improvement in the limit strain data. The NLSP has been found to play a larger role in Nakazima testing as shown by Min et al. [17] and Noder et al. [18]. For the ABST, it does not appear the NLSP provides a meaningful improvement for the steels considered.

4.5. Contact Pressure Calculation and Contact Pressure Modified Limit Strains

To apply the contact pressure corrections proposed by Min et al. [17], the 3-dimensional stress state must be determined. The generalized form of the pressure corrections were adapted from Noder et al. [18]. The 3-dimensional stress state can be expressed using the in-plane stress ratio, α, and through-thickness stress ratio

$$\chi = \frac{\sigma_3}{\sigma_1} \tag{4.5.1}$$

Where σ_1, σ_2, and σ_3 are the principal stresses. Assuming an associated flow rule, the yield function and hardening law in general form are

$$\sigma_{eq} = \sigma_{eq}(\alpha, \chi) \tag{4.5.2}$$

$$\bar{\sigma}\left(\varepsilon_{eq}^{p}\right) = \sigma_{eq}(\alpha, \chi) \tag{4.5.3}$$

The principal strain ratio measured using DIC on the convex layer is

$$\rho^{\exp}(\alpha, \chi) = \frac{d\varepsilon_2}{d\varepsilon_1} = \frac{d\sigma_{eq}/d\sigma_2}{d\sigma_{eq}/d\sigma_1} \tag{4.5.4}$$

and the equivalent plastic strain increment is

$$d\varepsilon_{eq}^{p}(\alpha,\chi)=k(\alpha,\chi)\left[1+\alpha\rho^{\exp}-\chi\left(1+\rho^{\exp}\right)\right]d\varepsilon_1 \tag{4.5.5}$$

The contact pressure calculation given by Min et al. [17] is a force equilibrium of tool contact pressure and internal force of an infinitesimal element of material being stretched over a punch with radii of curvatures R_1^O and R_2^O in the major and minor strain direction respectively:

$$\chi=\frac{\sigma_3}{\sigma_1}=\frac{t}{R_1^O}\left(1+\frac{t}{2R_2^O}\right)-\frac{t\alpha}{R_2^O}\left(1+\frac{t}{2R_1^O}\right) \tag{4.5.6}$$

To compensate for the effect of contact pressure, the method of Min et al. [17] is based on a stress mapping which maps the limit strains between 3-dimensional and plane stress states such that

$$\left(\sigma_1,\sigma_2,\sigma_3\right)^{3D}\rightarrow\left(\sigma_1,\sigma_2,0\right)^{2D} \tag{4.5.7}$$

The equivalent strain in the effective plane stress (2D) state, ε_{eq}^{PS} is

$$\tilde{\sigma}\left(\varepsilon_{eq}^{PS}\right)=\frac{\sigma_1}{k(\alpha)} \tag{4.5.8}$$

and the principal strain ratio (assuming an associated flow rule) under the equivalent plane stress state is

$$\rho^{PS}=(\alpha,0)=\frac{N_2}{N_1}=\frac{d\sigma_{eq}/d\sigma_2}{d\sigma_{eq}/d\sigma_1} \tag{4.5.9}$$

Then the plane stress limit strains are determined

$$\varepsilon_1^{PS}=\frac{\varepsilon_{eq}^{PS}}{\phi(\alpha)\left[1+\alpha\rho^{PS}\right]} \tag{4.5.10}$$

$$\varepsilon_2^{PS} = \rho^{PS}\varepsilon_1^{PS} \tag{4.5.11}$$

4.5.1. Stretch Bend Limit Strains with Contact Pressure Correction

In this section, the pressure corrections are shown for various bend severities to illustrate their effect on the limit strains. The gap width and punch radius are denoted directly on the legend, representing the limit strain for that test condition. The pressure corrected limit strains are labeled with a 'P' followed by the gap width-punch radius in millimeter (mm). The pressure corrected limit strains for the 590R 76.2 mm width samples with a bend severity of 1.4 are shown in Figure 4-19 and for a bend severity of 0.28 are shown in Figure 4-20 .

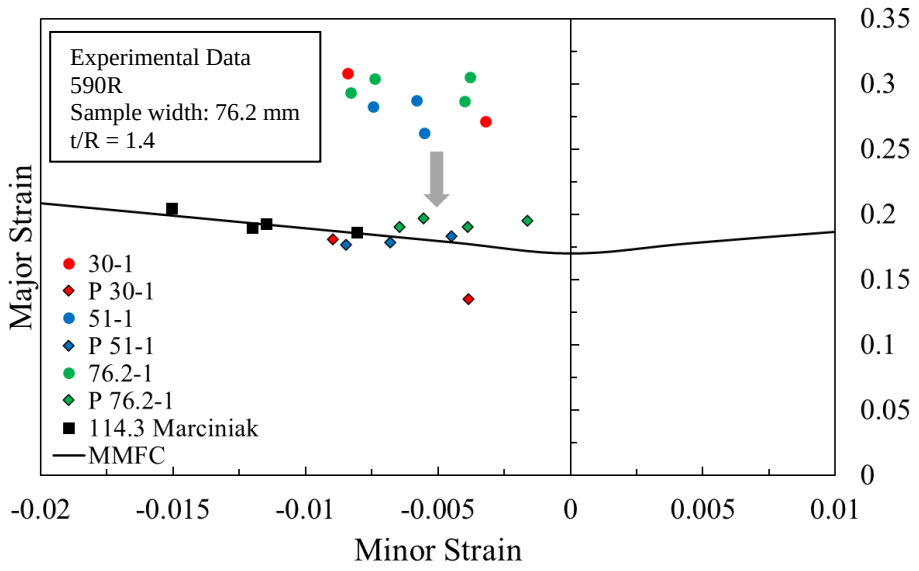

Figure 4-19 - 590R Pressure Corrected Limit Strains, t/R = 1.4, 76.2 mm sample – arrow denotes general shift of limit strains after pressure correction

The pressure corrected limit strains show relative agreement with the in-plane FLC for a bend severity of 1.4 (excluding a notable outlier with one of the 30-1 samples). For the bend severity of 0.28, the pressure correction works to some extent but is too severe for 30 mm gap width tests. The trend for overcompensation of the limit strains continues for the lowest bend severity of 0.14

shown in Figure 4-21. As the gap width decreases, the *magnitude* of the pressure correction increases resulting in over-corrections of the limit strains.

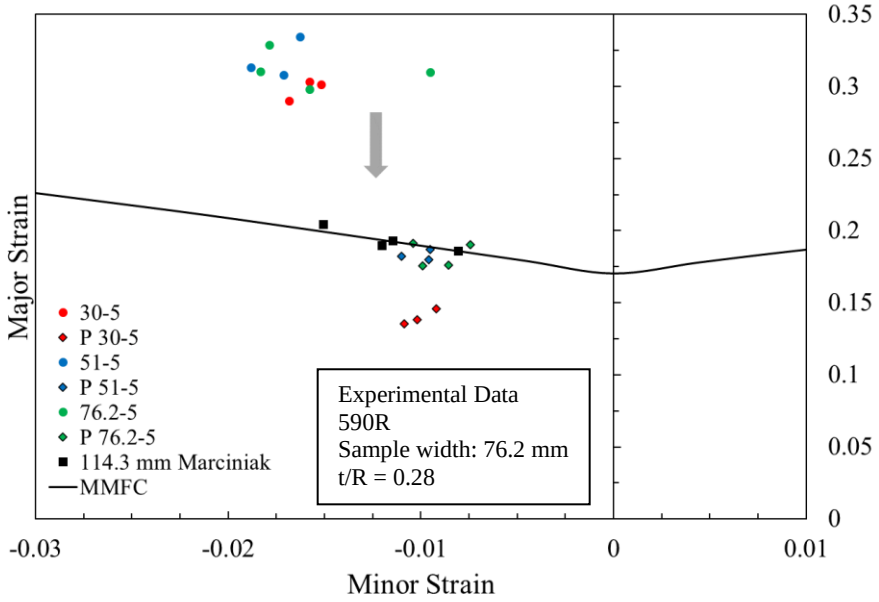

Figure 4-20 - 590R Pressure Corrected Limit Strains, t/R = 0.28, 76.2 mm sample - arrow denotes general shift of limit strains after pressure correction

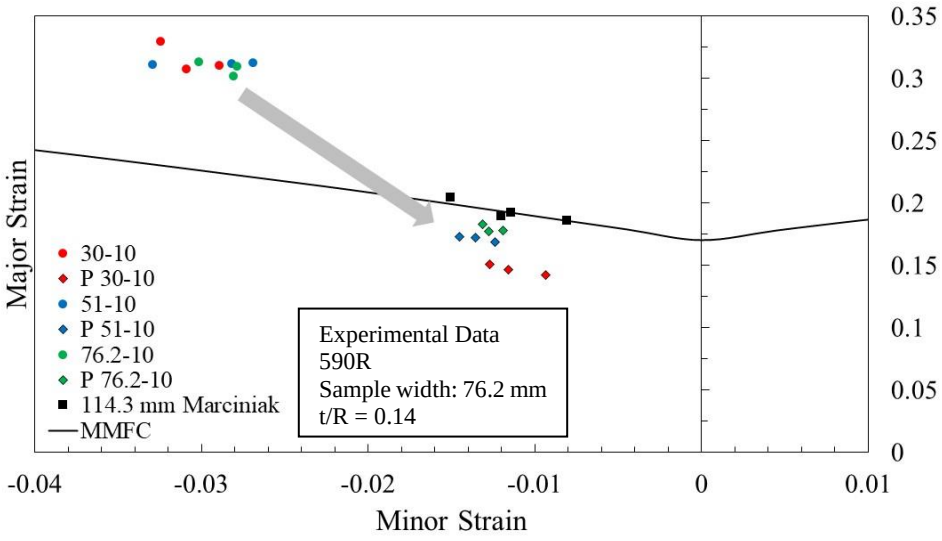

Figure 4-21 - 590R Pressure Corrected Limit Strains, t/R = 0.14, 76.2 mm sample - arrow denotes general shift of limit strains after pressure correction

Turning to the 3rd Gen 1180 pressure corrections shown in Figure 4-22 for the 76.2 mm width sample with a bend severity of 1.4, the results show relative agreement with the in-plane FLC.

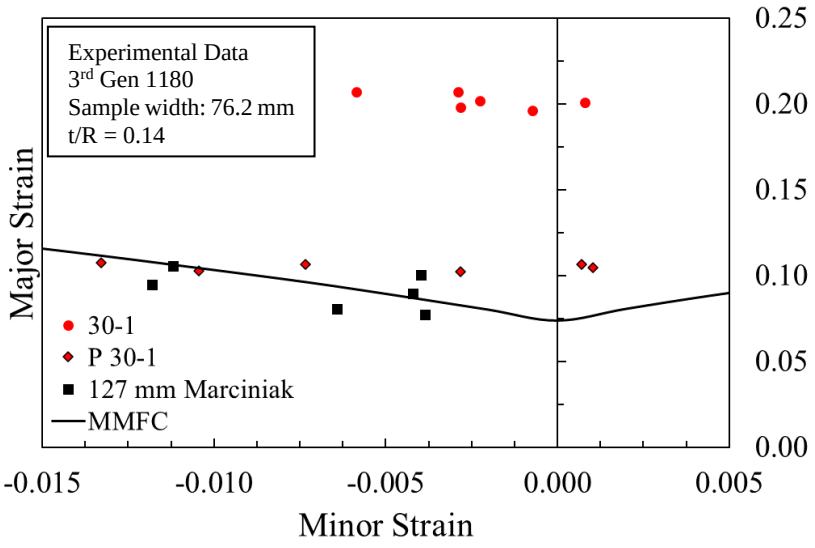

Figure 4-22 - 3rd Gen 1180 Pressure Corrected Limit Strains, t/R = 1.4, 76.2 mm sample

The pressure corrected limit strains for the 25.4 mm width samples are shown in Figure 4-23. The correction is too severe for the lower bend severity of 0.093 but the 0.28 bend severity is in good agreement with the in-plane FLC.

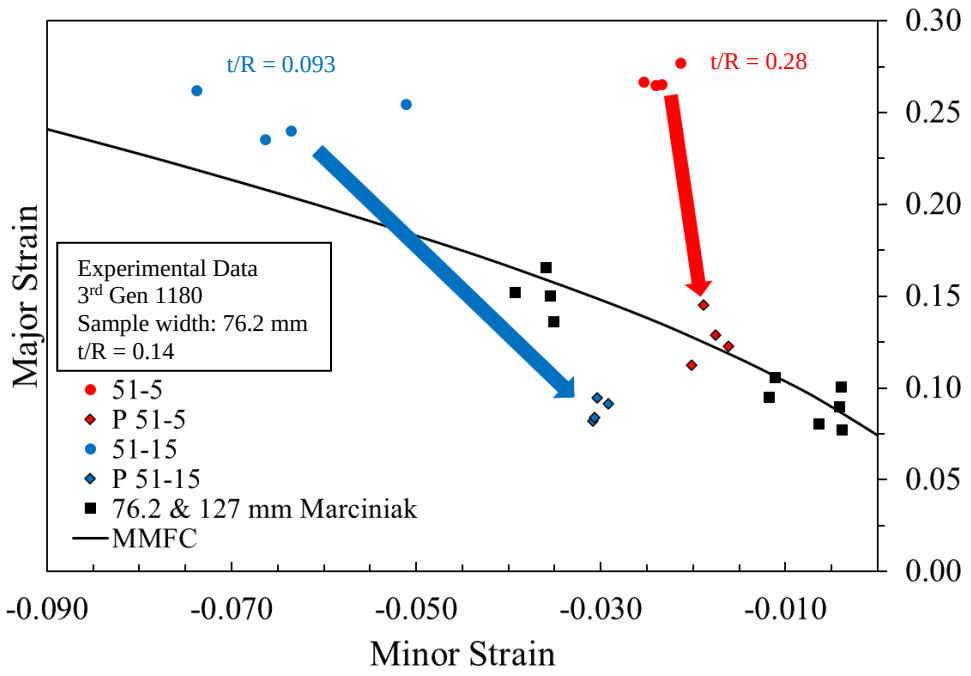

Figure 4-23 - 3rd Gen 1180 Pressure Corrected Limit Strains, 25.4 mm sample - arrow denotes general shift of limit strains after pressure correction

Overall, the contact pressure correction method of Min et al. [17], which is equivalent to that of Smith et al. [36], has struggled with the ABST results. It is unclear if the cases of good agreement is due to coincidence. The general trend is that the magnitude of the limit strain correction increased as the bend severity decreased which is counter to the expected trends. The lower bend severity cases were expected to be most amenable to the correction process since the contact pressure is lower and deformation is closer to in-plane. In contrast, the high bend severity cases of 1.4 and 0.28 performed better than the 0.093. The lower the bend severity, the greater the probability that the contact pressure correction would be excessive, resulting in inadmissible limit strains that fall below that of the in-plane FLC.

The contact pressure model was not evaluated using finite-element analysis in the work of Min et al. [17] but derived from a simplified assumption of equilibrium that did not account for

the through-thickness stress distribution. The contact pressure will be investigated further with the aid of numerical simulation in Chapter 5.

5. Stretch Bend Simulation – Development of Finite Element Model and Analysis

In this chapter, a finite element model of the ASBT was developed using the commercial finite-element software LS-DYNA [37] and Altair HyperMesh [38]. A bend severity of unity and the smallest die gap width of 30 mm was selected for model development. This geometry represents the most severe through-thickness strain gradients for the finite-element model to resolve.

This chapter is divided into subsections to chronicle model development. Section 5.1 involves the development of a solid element model required for detailed analysis of the through-thickness gradients. Section 5.2 considers a shell element model since shell elements are extensively used within the automotive forming industry. Identifying the limitations of shell elements with respect to the solid elements is important to understand how to transfer the outcomes of the research to industry. In Section 5.3 an investigation of the chosen simulation solver and contact algorithm was performed. A study on obtaining contact pressure was conducted to support the evaluation of the through-thickness strain and contact pressure models for process-corrections of the limit strains in Section 5.4.

5.1. Identification of the Number of Through-thickness Solid Elements in Stretch Bending

The minimum number of through-thickness elements required to resolve the through-thickness strain gradient is an important modelling parameter. The LS-DYNA implicit solver was chosen to reduce the computational cost of running solid element simulations without the need to artificially increase the mass of the model. The LS-DYNA explicit and implicit solvers are

compared later in Section 5.3. The so-called mortar contact option was used as recommended in the LS-DYNA manual for implicit contact. Additional contact options are evaluated in Section 5.3.

5.1.1. Finite-element Model Setup

A narrow strip of material was modelled with a plane strain boundary condition enforced on the width. The initial thickness of the strip was the same as the sheet thickness of 1 mm. A schematic of the model is shown below in Figure 5-1 with the positive X and Y axes denoted. The blank was modeled with fully integrated brick elements (type -2 as recommended by LS-DYNA [39] for implicit simulations).

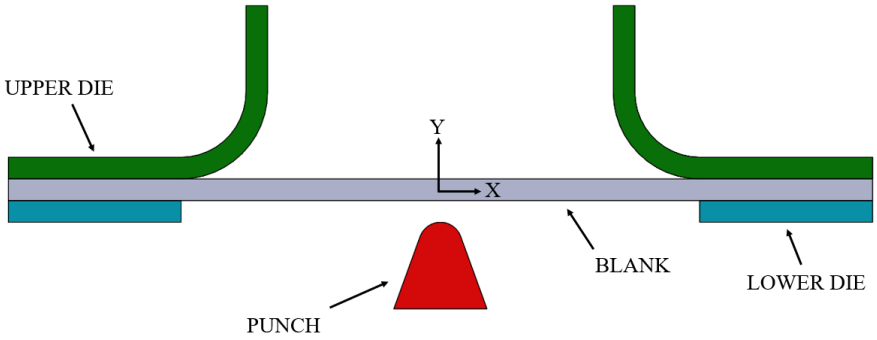

Figure 5-1 - Schematic of the ASBT model

The mesh included a refinement zone where the aspect ratio of all the elements inside the zone are unity. The refinement zone was equal to 8 times the punch radius in length along the x-direction (8 mm), shown in Figure 5-2 and listed in Table 5-1. A coarser mesh of 0.5 mm was used outside the refinement zone where the strains were significantly lower.

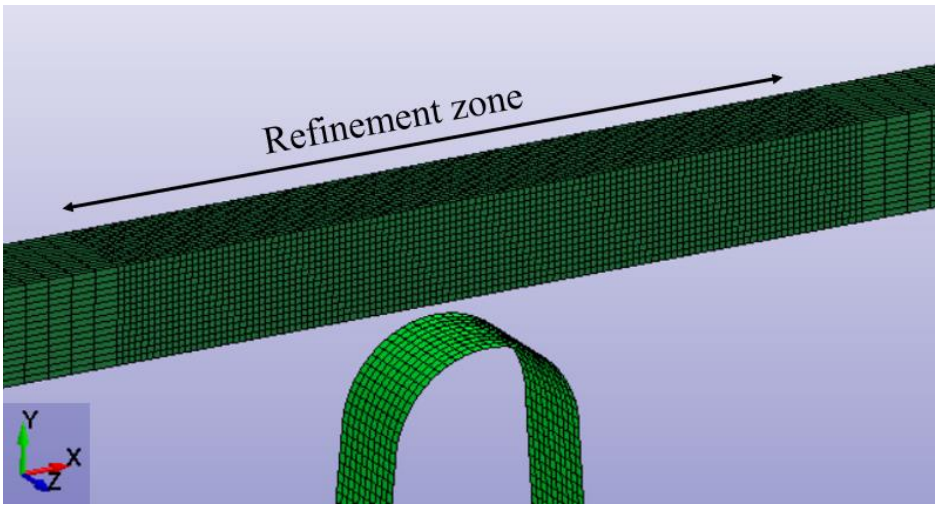

Figure 5-2 - Detail view of mesh in ASBT mesh convergence model

Table 5-1 - Mesh sizes for mesh convergence study

Number of Through-thickness Elements (N)	Element size in refinement zone (mm)
4	0.25
5	0.2
10	0.1
15	0.067
20	0.05

The blank was assumed to isotropically harden according to the Ludwik power-law hardening model

$$\bar{\sigma} = \sigma_y + K\left(\varepsilon_{eq}^{p}\right)^{n} \tag{5.1.1}$$

The power-law hardening model was selected because it is simple to understand how the hardening behaviour changes with the parameters *K* and *n*. The strength coefficient *K* governs the strength while the hardening exponent, *n*, controls the hardening rate. For in-plane uniaxial and plane strain tension, the onset of diffuse necking occurs when $\varepsilon_1 = n$.

Both σ_y and *K* were set to 500 MPa, and the strain hardening exponent *n* was set to 0.1. The stress-strain response is shown in Figure 5-3 along with the same power-law model with a strain

hardening exponent of 0.3. For the work in this chapter only the power-law model with $n = 0.1$ is used since it represents a broad range of automotive sheet metals used in structural components. The strain hardening exponent of 0.3 is often found in low strength, high ductility materials such as deep draw quality (DDQ) steels and is evaluated later in Chapter 5.

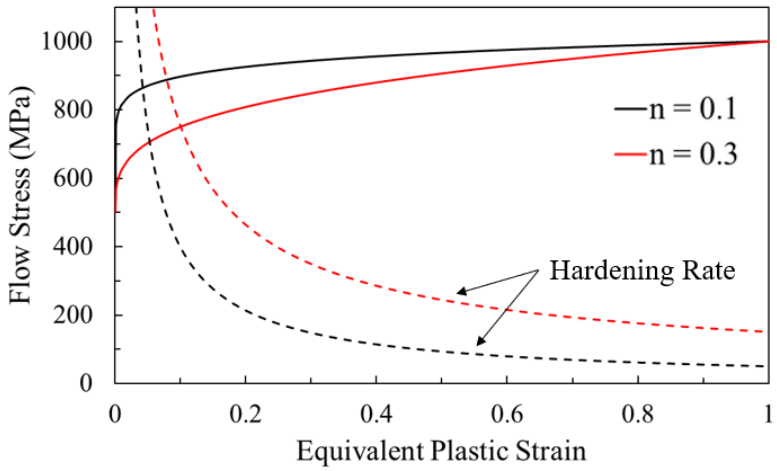

Figure 5-3 – Stress-strain response and hardening rate of power-law material used in simulations, $K = \sigma_y = 500$ MPa

5.1.2. Convergence of Load-displacement Response

The load-displacement response is shown in Figure 5-4 for all mesh sizes considered from 0.25 to 0.05 mm. The load response was relatively insensitive to the mesh size but should not be used alone to define mesh convergence for instability or fracture modelling. It will be shown that the through-thickness stress and strain gradients are very sensitive to the element size in contrast to the load response.

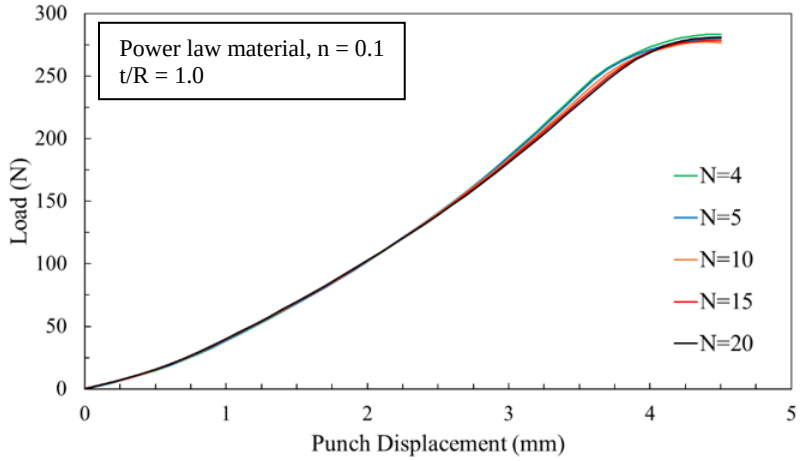

Figure 5-4 – Variation of load vs. displacement response with number of elements through-thickness

5.1.3. Thickness Strain of the Cross-Section

The evolution of the thickness strain of the cross-section is shown in Figure 5-5 and defined as

$$\varepsilon_3 = \ln\left(\frac{t}{t_0}\right) \tag{5.1.2}$$

The thickness strain of the cross-section is measured from a node-to-node measurement between the upper and lower surfaces of the sheet. It is emphasized that due to bending and contact pressure, the thinning strain at each element or 'layer' of material will be different. In pure bending without a superimposed tension force, the thickness strains would be negative above the neutral layer in tension to indicate thinning and be positive in compression below the neutral layer where the layers thicken. The initial position of the neutral layer in pure bending is at the sheet mid-thickness but shifts down toward the inner concave layer during deformation.

The evolution of the thickness strain of the cross-section is shown in Figure 5-5 with the limit strains obtained from the models using the mod. LBF method. The trend for thinning was similar for all simulations with the thinning rate rapidly increasing as localization occurs. The thickness

strain of the cross-section does not appear sensitive to the number of elements and like the punch force, is not suitable to evaluate mesh convergence.

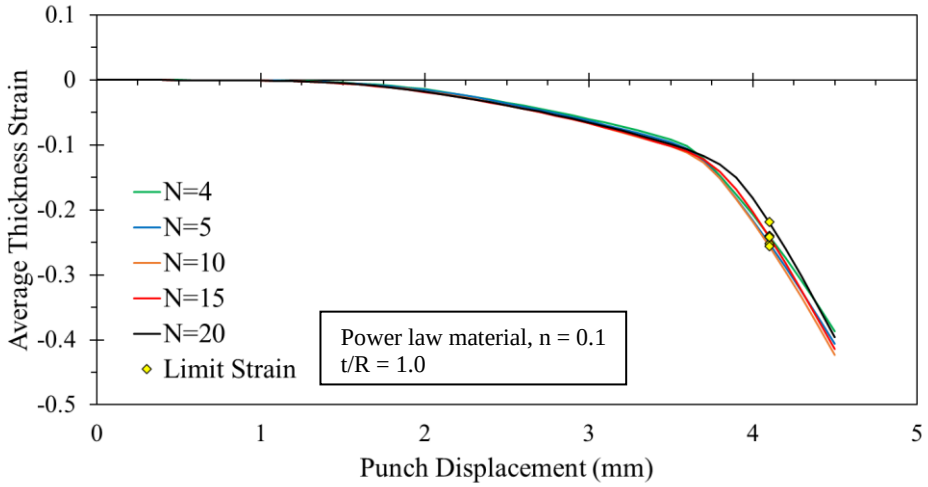

Figure 5-5 – Variation of thickness strain with number of elements through-thickness plotted against punch displacement

5.1.4. Through-Thickness Major Strain Distribution for Mesh Convergence

The variation of the major strain through the thickness of the blank can be investigated at various levels of punch displacement to assess mesh convergence. The major strain distribution was obtained at 100%, 75%, and 50% of the punch displacement when the peak load occurred (4.5, 3.4, 2.3 mm respectively) and shown in Figure 5-6 - Figure 5-8, respectively. The normalized thickness values of one and zero corresponds to the top (convex) surface and bottom (concave) surface in contact with the punch. Note that the through-thickness data is taken from each element as the average value from its 8 integration points.

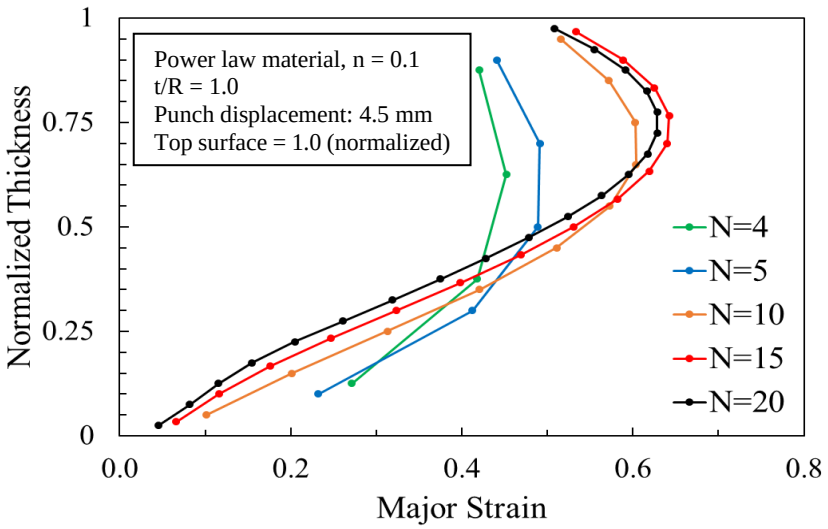

Figure 5-6 - Variation of the major strain through-thickness of the sheet with number of elements at the peak load

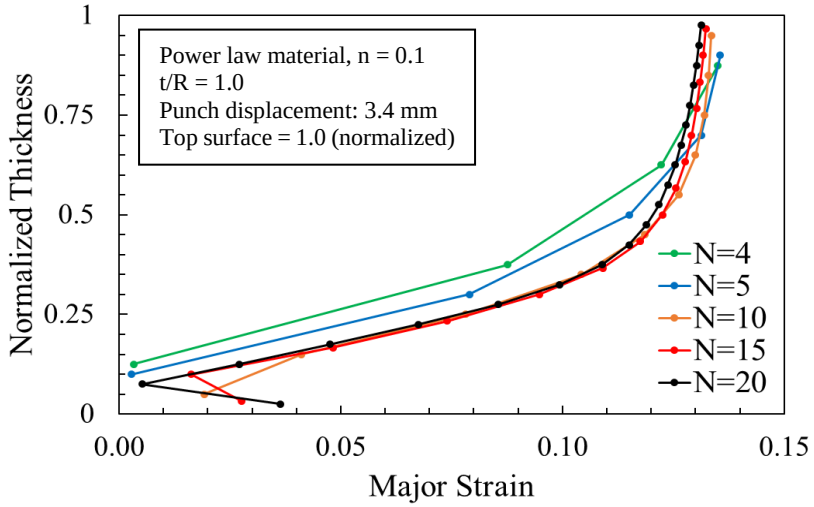

Figure 5-7 – Variation of the major strain through-thickness of the sheet with number of elements at 75% max. load punch displacement

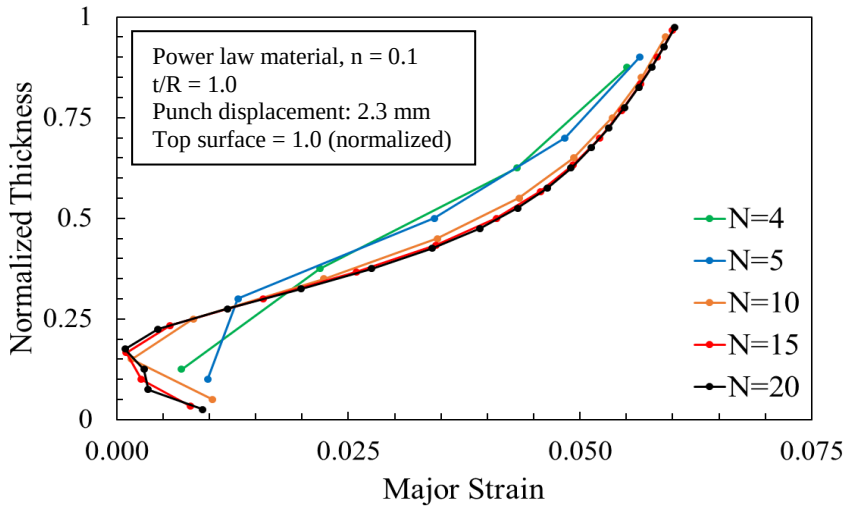

Figure 5-8 - Variation of the major strain through-thickness of the sheet with number of elements at 50% max. load punch displacement

It is evident that a minimum of 10 elements per millimeter of blank thickness is required to reliably characterize the through-thickness strain gradient for the bend severity of unity. This mesh density would be sufficient for less severe bending but would otherwise require additional mesh convergence studies.

5.2. Evaluation of Shell Elements in Stretch-bending

The automotive forming industry seldom uses solid elements due to their computation cost and instead uses plane stress shell elements. Shell elements employ different mathematical formulations to predict the through-thickness strain and corresponding strain gradients in bending. To understand how the results of the thesis that involve solid elements can be generalized to industry, a parametric evaluation of shell element types was also considered for the solid element convergence study $(t/R = 1)$. It is important to note that a t/R of unity is a severe case for shell elements and it is expected that the shell elements will struggle with this bend severity. The rule-of-thumb in automotive finite-element modelling is that shells are best suited for deformation with bending when $t/R < 0.2$.

5.2.1. Background on Shell Elements

The following background is a brief explanation of the LS-DYNA shell types considered in the study A detailed explanation of shell element formulations is outside the scope of this thesis.

The type 2 shell element is a Belytschko-Lin-Tsay shell element [40], [41] and the default element type in the LS-DYNA explicit solver due to its computational efficiency. The type 2 shell element is a reduced integration element with one integration point located at the center of the element.

The type 16 shell is a fully integrated shell element that is approximately 2-3 times more expensive than the type 2 shell [42]. The type 16 shell has 4 in-plane integration points (2x2) to resist spurious zero-energy modes such as hourglassing that affect reduced integration elements such as the type 2 shell [39]. The type 16 shell is commonly used for sheet metal forming simulations and has largely replaced the type 2 as computational power has increased in recent years.

The conventional ‘thin’ shells such as the type 2 and 16 shells enforce a plane stress condition. So-called ‘thickness enhanced’ or ‘thick-thin’ shells do not enforce a plane stress condition and can support a linear strain gradient through the thickness. The thickness enhanced shell used in this comparison is the type 26 shell element which is a fully integrated shell element with thickness stretch.

In addition to the element types described above, an additional setting within LS-DYNA was investigated referred to as the ‘IDOF’ setting. The IDOF setting for the type 2 and 16 shell by default is set to zero and does not alter the behaviour of the element. However, if IDOF is set to 3, the contact pressure can influence the stress and produce thickness changes [39]. For the type 26

shell element, IDOF has a different meaning and is set to 1 by default which produces a continuous thickness field and is recommended for sheet metal forming [42]. With IDOF set to 2 the thickness field is discontinuous which is recommended for crash applications [42].

5.2.2. Finite-element model of the ASB using shell elements

The shell element model ASBT setup is kept as close to the solid element convergence study setup as possible to allow comparison between the shell and solid element simulations. The tooling, boundary conditions, and material properties are identical. The blank was meshed with the converged element size of 0.067 mm to compare with the solid element simulation with 15 through-thickness elements. Due to the lower computational cost of shell elements, the refinement zone was not necessary for the blank. The number of through-thickness integration points was set to 10 as this is the maximum permitted number of integration points usable with Lobatto integration [39]. Lobatto integration was chosen instead of the default Gauss integration since extrapolation of the strain field to the surfaces of the shell is avoided. The shell element types used are shown in Table 5-2.

Table 5-2 - Shell element and IDOF settings used in shell element study

Shell type (LS-DYNA)	Description	IDOF setting
2	Default shell formulation	0 and 3
16	Fully integrated shell	0 and 3
26	Thickness enhanced shell	1 and 2

5.2.3. Load-displacement Response

The load-displacement response for the shell element simulation and the solid element simulation (N=15) is shown in Figure 5-9. Notably, the peak load does not match for the ‘thin’ shells and the thickness enhanced shell elements. The type 2, 16, and 26 (IDOF=2) shell element

models all experience dramatic load drops before the solid elements. As expected, the conventional thin shells (type 2 and 16) had poor agreement with the solid elements and are not recommended to model high bend severities. The thickness enhanced shell (type 26) with IDOF = 1 provided the closest agreement to the solid elements but overestimated the peak force. Only the type 26 shell element with IDOF = 1 will be studied further.

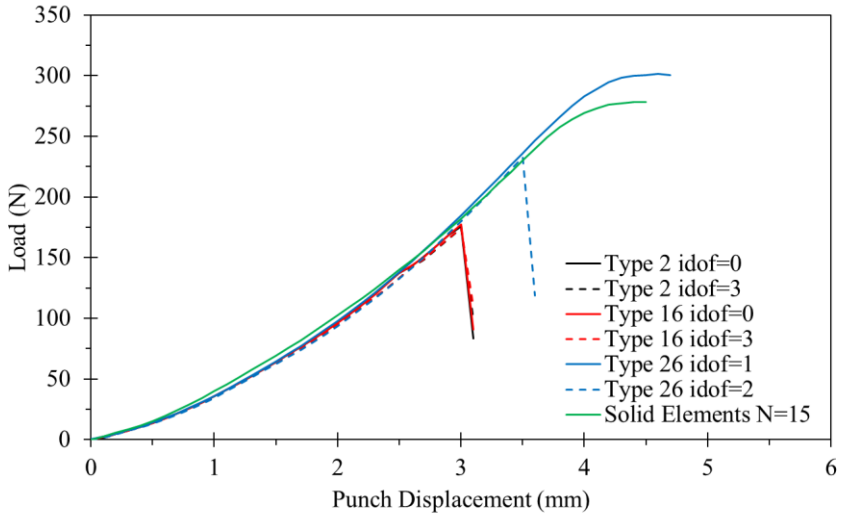

Figure 5-9 - Load-displacement response comparison of shells vs. solids

5.2.4. Through-thickness Equivalent Strain and Normal Stress Distributions

The through-thickness equivalent strain distribution of the shell element simulations was plotted against the normalized thickness. The evolution of the strain distribution with the three punch displacement levels of 50%, 75% and 100% of the peak load displacement are shown in Figure 5-10 - Figure 5-12.

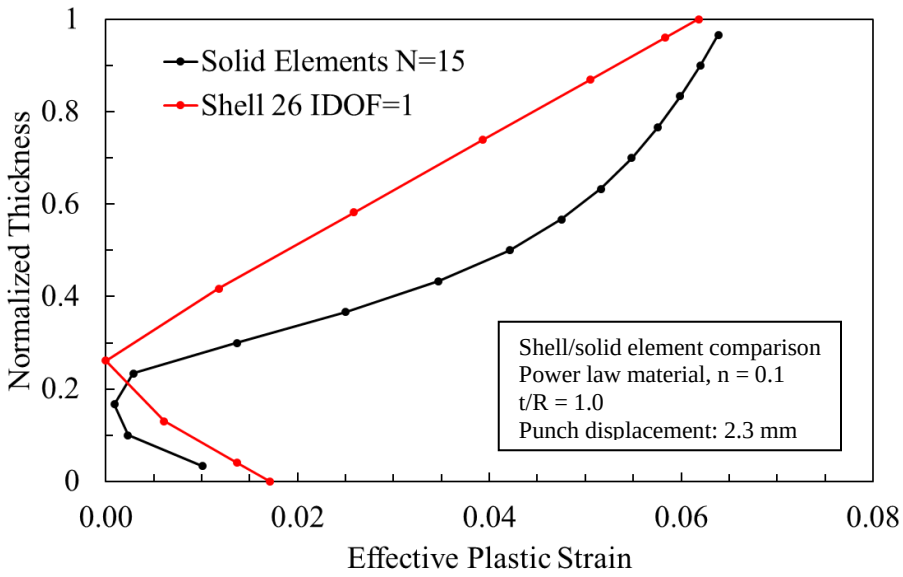

Figure 5-10 - Through-thickness strain comparison, 2.3 mm punch displacement

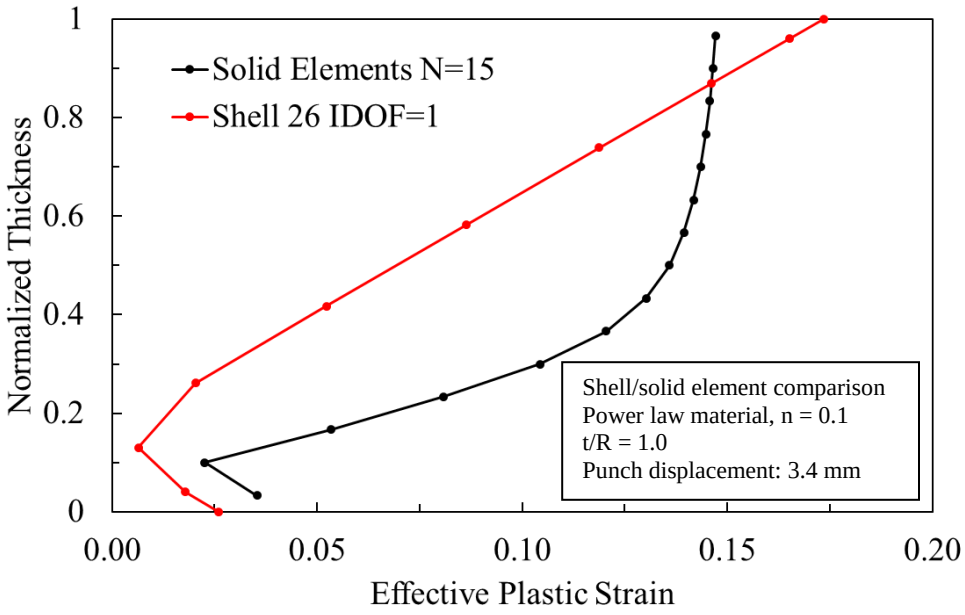

Figure 5-11 - Through-thickness strain comparison, 3.4 mm punch displacement

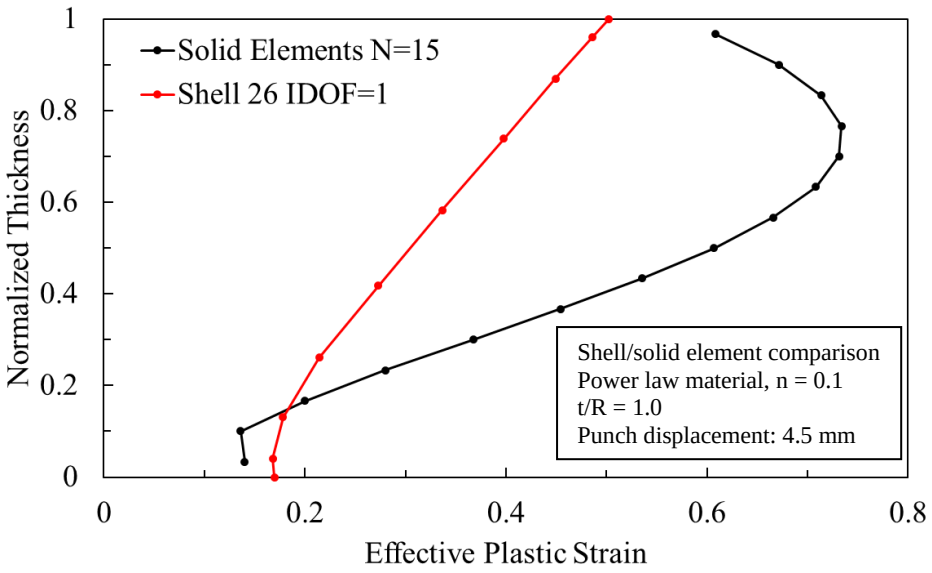

Figure 5-12 - Through-thickness strain comparison, 4.5 mm punch displacement

The agreement between the shell and solid elements is poor. Although the punch load-displacement response can be adequately predicted using the Type 26 shell element, it does not predict the through thickness strain gradient accurately.

Shown in Figure 5-13, Figure 5-14, and Figure 5-15 are the through-thickness stress distributions at 50%, 75% and 100% peak load punch displacement respectively. The type 26 shell produces non-physical results as the normal stress at the free surface is non-zero. Generally, agreement with the solid element simulation is poor for the other points through the thickness. Furthermore, the stress through the thickness changes drastically between the bottom integration points for the type 26 shell at the lower punch displacements (Figure 5-10 and Figure 5-11).

Note that in Figure 5-14 and Figure 5-15, the solid element simulation shows that the through-thickness stress, or normal stress, on the concave surface is decreasing with greater punch displacement. This was due to the sheet gradually lifting off the punch with increased strain, shifting the maximum normal stress location away from the centre.

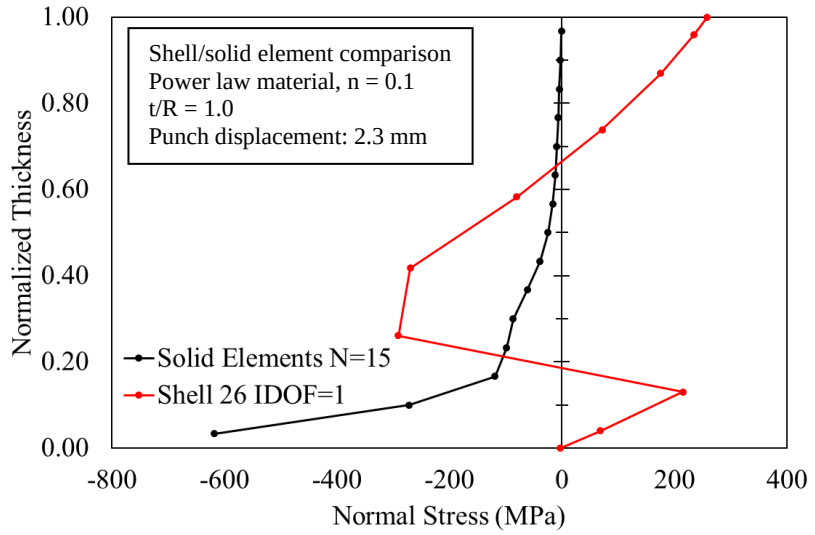

Figure 5-13 – Through-thickness stress comparison, 2.3 mm punch displacement

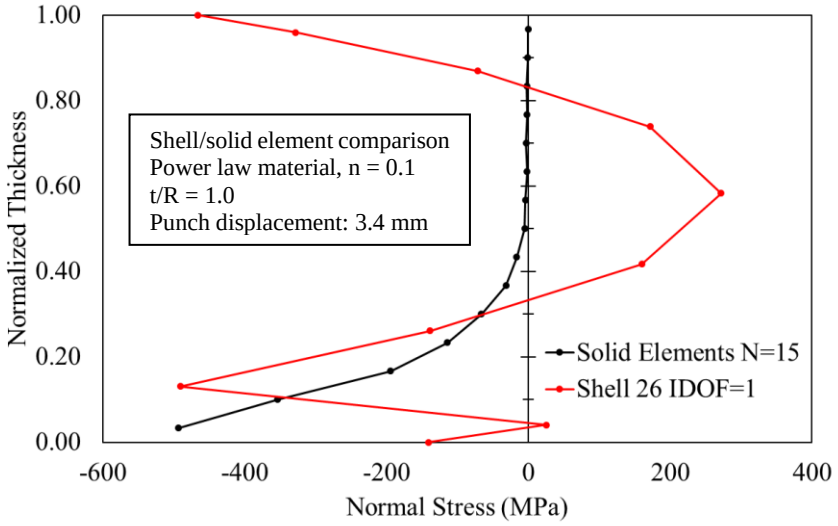

Figure 5-14 – Through-thickness stress comparison, 3.4 mm punch displacement

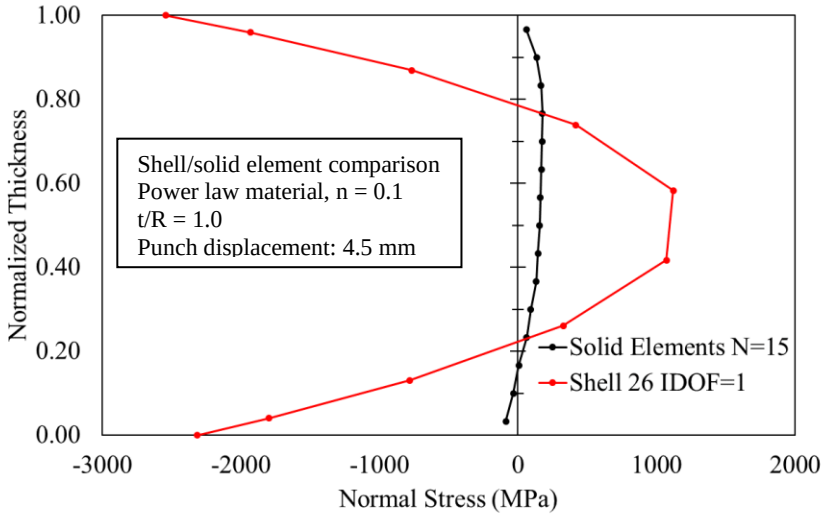

Figure 5-15 – Through-thickness stress comparison, 4.5 mm punch displacement

To summarize the shell element comparison, the type 2 and 16 shells ('thin' shells) and type 26 shell ('thick-thin' shell) with IDOF set to 2 are not suitable for use as the load-displacement response is significantly underpredicted. The type 26 shell with IDOF set to 1 was able to provide relatively good agreement in the force response with the solid element simulations. Unfortunately, the through-thickness strain distribution was not well captured but the overall magnitudes were closer.

The normal stress distribution of the type 26 shell was also in significant error with the stress overpredicted by three orders of magnitude yielding stress values greater than 2000 MPa in compression. It is also concerning that the type 26 shell produced a non-zero normal stress on the convex surface of the blank, which is a free surface and should have zero normal stress. It was expected that shell elements would be challenged by the bend severity of unity but was hoped that better agreement would have been possible with the newer type 26 enhanced shell. Certainly, lower bend severities would be more amenable for shell elements but since this thesis spans bend severities up to 1.4, shell elements will not be considered further. Future work will be required on

how to improve the shell element formulations and to compensate for the errors at the integration point level to predict necking in stretch-bending modes.

5.3. Investigation of Simulation Solver, Contact Type, and Measurement of the Contact Pressure

The previous work in this chapter was completed using the LS-DYNA implicit solver and the mortar contact option. The LS-DYNA implicit/explicit solver and different contact types are compared in this section along with the methodology to extract the contact pressure, which is not as straightforward as it may first appear.

A quarter symmetry model was used to compare to the 590R experiments using the 590R constitutive model (see Section 2.1), the von Mises yield surface, 76.2 mm sample width, 30 mm die gap width, and 1 mm radius punch. This test condition was selected for the high amount of bending produced which requires more elements to accurately capture the bending behaviour. The model geometry is shown below in Figure 5-16.

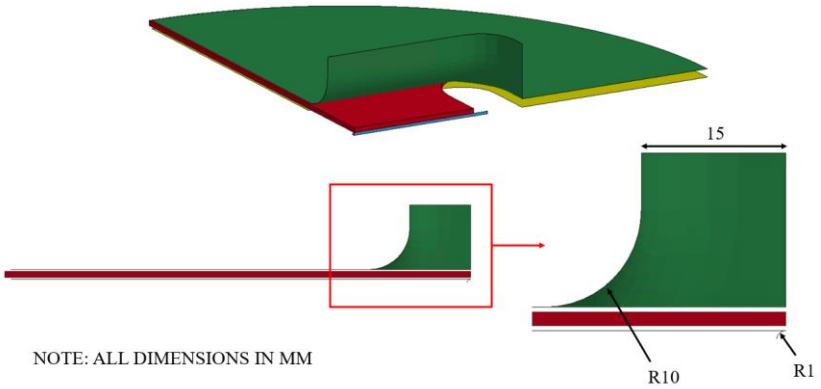

Figure 5-16 - Quarter symmetry model with 76.2 mm sample, 30 mm die gap, and 1 mm radius punch

5.3.1. Comparison of Load-Displacement Response with Experimental Data

The number of through thickness solid elements was set to 15 (element height = 0.067 mm) based on the simulation study of the material strip in Section 5.1. Since the contact pressure

calculation will depend upon the area of the element in contact with the punch, the in-plane dimensions of the element were varied. The term, 'uniform', refers to using a 1:1 ratio of the element length to width for sizes of 0.5, 0.75, and 1 mm. A non-uniform mesh with a bias towards the center of the blank was also considered with a cubic element size of 0.067 mm at the center of the blank. A comparison of the experimental and predicted load-surface displacement responses for each mesh pattern are shown in Figure 5-17. The predicted force response was identical for all mesh patterns except for differences in peak load. Overall, the predicted load history was slightly overestimated for all mesh patterns over the first 4 mm of displacement.

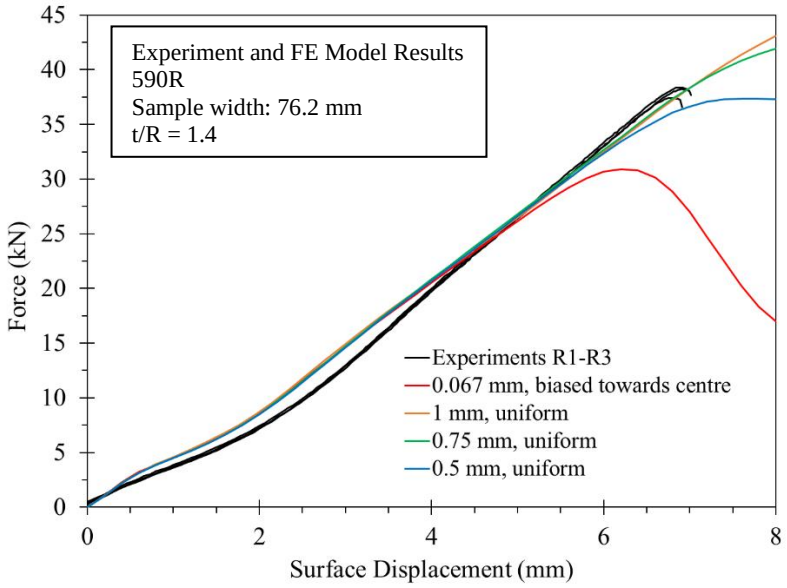

Figure 5-17 – Load-surface displacement response of various meshes

5.3.2. Comparison of Surface Strains with Mesh Pattern and Size

To choose a suitable mesh, the surface major strain data along a line along the length of the sample was compared. A schematic of the data collection line is shown below in Figure 5-18.

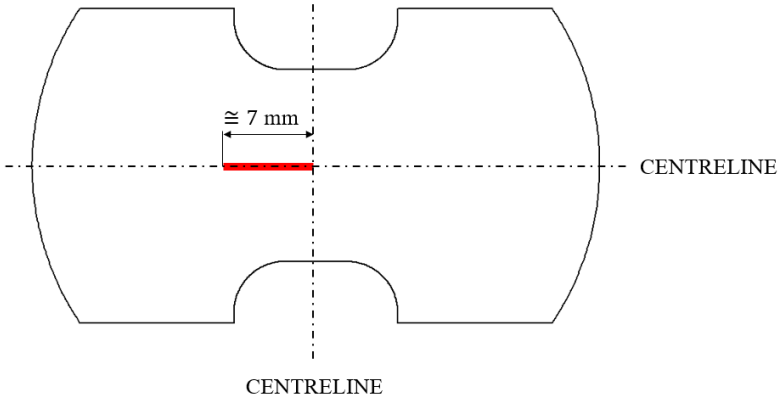

Figure 5-18 - Schematic showing data collection line for major strain on the surface

The simulation major strain data was compared to the experimental data at three punch displacements. The results are shown in Figure 5-19, Figure 5-20, and Figure 5-21 for respective displacements of 2, 4, and 6 mm. The displacement of 6 mm corresponds to the experimental displacement of the limit strains. The 0.067 and 0.5 mm meshes overestimate the major strain at large deformations, however, the virtual strain gage length of the experimental data was 1.1 mm. Therefore, it is expected that the smaller meshes will report higher strain magnitudes compared to the DIC. The 0.75 and 1 mm meshes predicted similar strain distributions and are in better agreement with DIC strain data. The 1 mm mesh was chosen over the 0.75 mm due to its similar strain distribution and lower computational cost.

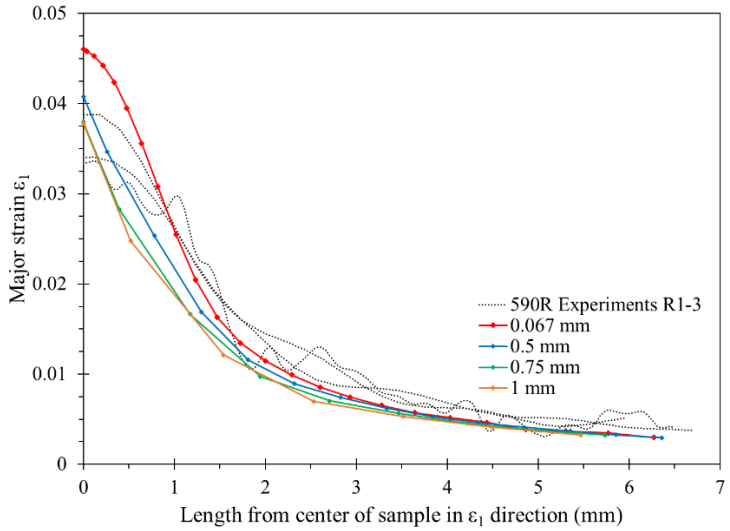

Figure 5-19 - Surface major strain comparison - 2 mm punch displacement

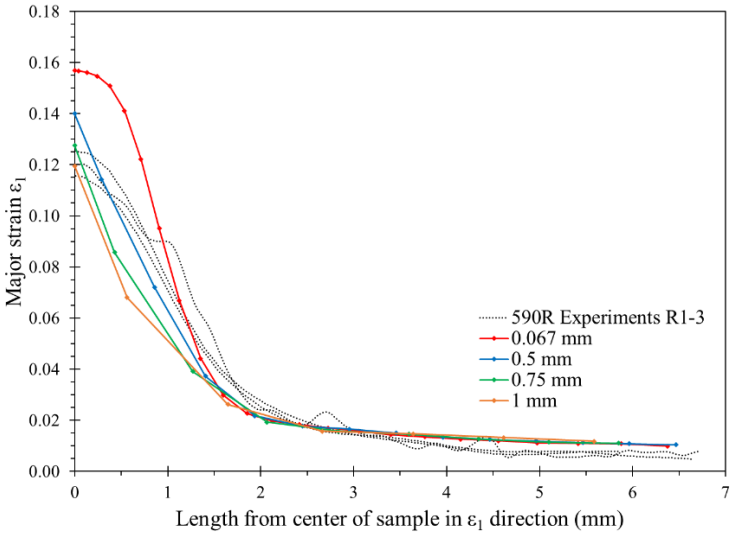

Figure 5-20 - Surface major strain comparison - 4 mm punch displacement

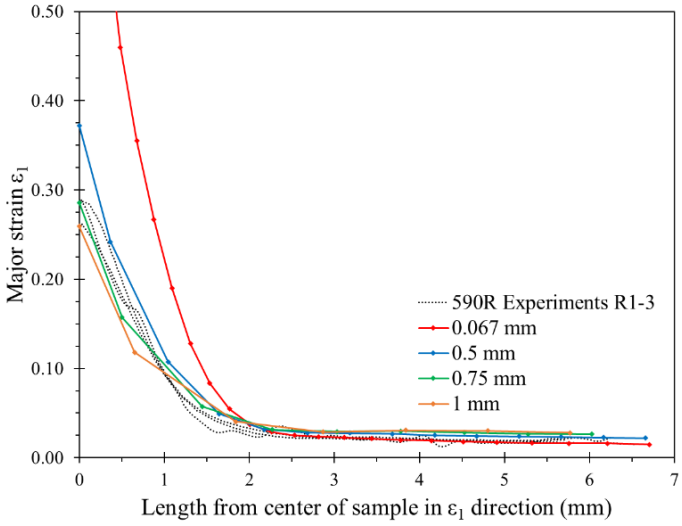

Figure 5-21 - Surface major strain comparison - 6 mm punch displacement - experimental limit strain

5.3.3. Evaluation of Simulation Consistency with Implicit/Explicit Solvers and Contact Algorithms

Implicit finite-element analysis has been used throughout the thesis since the ABST can be considered quasi-static to reduce computational cost. However, the treatment of contact within implicit solvers is a present concern within the automotive industry as explicit solvers are preferred to model contact and avoid erroneous deformation modes. Two penalty-based contact algorithms have been selected, the automatic surface-to-surface contact, and mortar contact, within LS-DYNA. The mortar contact is a modified version of the automatic surface-to-surface contact recommended for implicit analysis.

In LS-DYNA, contact is based on potential penetrations of slave nodes through a master segment. The user specifies areas to search for contact (i.e., contact between two parts), and LS-DYNA performs a contact search in each timestep using a contact algorithm. For penalty-based contacts, when penetration is detected, a force proportional to the penetration depth is applied to resist the penetration. The contacts considered in this thesis are denoted in LS-DYNA as ‘surface-

to-surface' contacts which mean that each slave node is checked for penetration through the master surface – these contacts can be 'automatic' or 'non-automatic'. Non-automatic contacts search for penetration only in the normal direction of the shell whereas automatic contact searches both sides.

The penalty stiffness calculation in LS-DYNA can be modified using the 'SOFT' parameter. When SOFT=0 (default), the penalty stiffness is a function of material properties and segment contact area:

$$k_{SOFT=0} = \frac{\alpha K A^2}{V} \tag{5.3.1}$$

where α is a scale factor, K is the bulk modulus of the contacted element, A is the area of the contacted segment, and V is the volume of the element.

An alternative stiffness calculation based on a local system made of two contacted segments is

$$k_{SOFT=1} = SOFSCL \frac{m^*}{\Delta t^2} \tag{5.3.2}$$

where SOFSCL is a scale factor, m^* is a function of the slave and master node masses and Δt is the time step size. When SOFT=1 the larger of the two stiffnesses calculated with Eqs. (5.3.1) and (5.3.2) is used.

Segment-to-segment based contact can be invoked by setting SOFT=2. Segment-to-segment contact can provide a more realistic distribution of contact forces [39]. For example, if two four-node segments come into contact, forces that resist penetration are applied to eight nodes. The stiffness is a function of segment masses and the timestep size

$$k_{SOFT=2} = \alpha \left(\frac{m_1 m_2}{m_1 + m_2} \right) \frac{1}{\Delta t^2} \tag{5.3.3}$$

where m_1 and m_2 are segment masses. The mortar contact in LS-DYNA does not utilize the SOFT parameter and Eq. (5.3.3) is used to calculated the penalty stiffness. The details for contact settings used in the simulations are shown in Table 5-3.

Table 5-3 - Simulation Details to compare solver and contact type

LS-DYNA Solver	Contact Type	Contact Description	SOFT	Abbreviation
Implicit	Mortar	Surface-to-surface	Default	imp mortar s2s
Explicit	2-way automatic	Surface-to-surface	Default	exp auto s2s
Explicit	1-way automatic	Surface-to-surface	Default	exp auto 1way
Explicit	1-way automatic	Surface-to-surface	SOFT=1	exp auto soft=1
Explicit	1-way automatic	Surface-to-surface	SOFT=2	exp auto soft=2

The predicted load-displacement responses for the different analysis settings are shown in in Figure 5-22. The 2-way automatic contact formulation led to improved agreement with the experimental response for both the implicit and explicit analysis compared to the mortar contact definition. The explicit 1-way contact produced nearly identical results to the explicit 2-way contact and is not shown in Figure 5-22 for clarity.

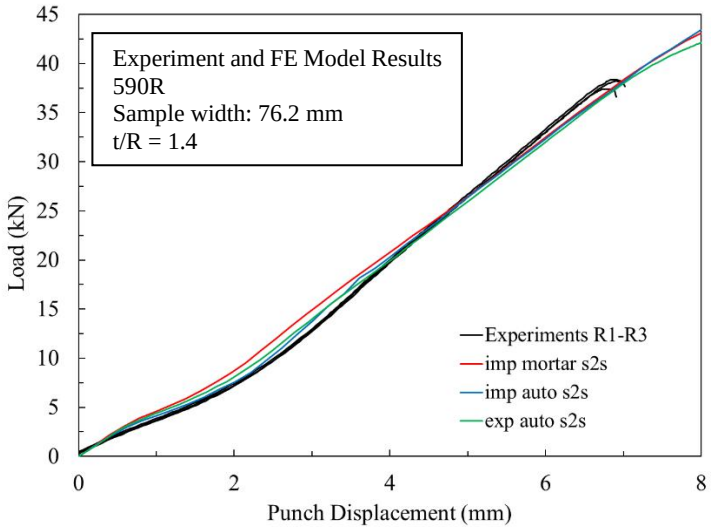

Figure 5-22 - Load-displacement response of 2-way contacts, 1 mm mesh

The explicit 1-way and implicit mortar contact predictions of the force response are shown in Figure 5-23. Activation of the SOFT contact option effectively stiffened the response to where it is nearly identical to the results of the implicit mortar simulations. This is expected since the SOFT contact option invokes segment-to-segment contact that is also used in the mortar contact algorithm [39]. From the perspective of computational efficiency, there appears to be no benefit to using the 2-way contact or SOFT options when using LS-DYNA explicit to model the ASBT. Explicit 1-way contact appears sufficient and provided the best agreement with the experiment. The implicit solutions are attractive for their low run-time and overall close agreement with the explicit solution, although they appear to be slightly stiffer in the force response.

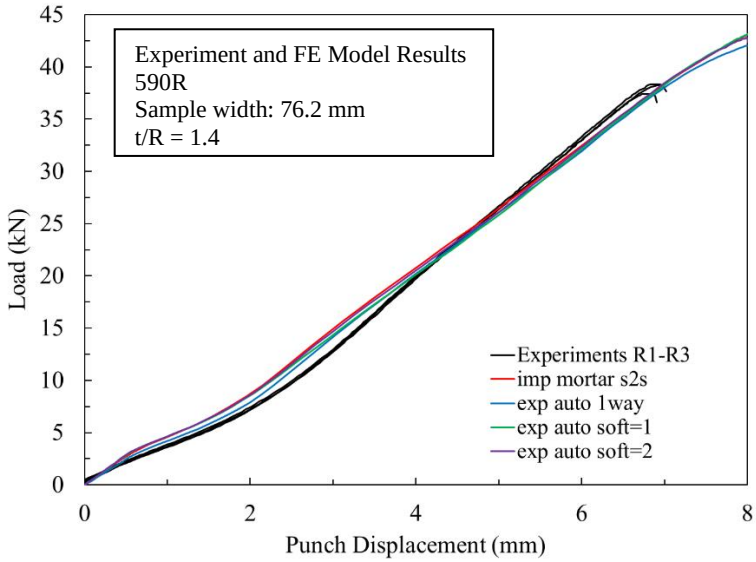

Figure 5-23 - Load-displacement response of 1-way contacts and implicit for reference, 1 mm mesh

5.3.4. Comparison of Simulation Contact Pressure

The contact pressure was investigated to gain more insight into the explicit/implicit solvers and contact algorithms. Using LS-DYNA, contact interface and contact area data was used to determine the contact pressure. The implicit mortar simulation is used along with the explicit simulation using 1-way automatic contact.

The contact area in LS-DYNA is based on the element size, meaning that an element in contact with an area of 1 mm^2 will produce a contact area of 1 mm^2 even if the element is only partially in contact. This leads to discontinuities in the contact area data and affects the contact pressure calculation. The interface pressure normalized by the yield stress is shown for the implicit mortar simulation and the explicit 1-way automatic contact simulation in Figure 5-24. Note that due to discontinuities in the contact area at small punch displacements, the explicit simulation data is plotted starting at 0.5 mm of punch displacement. Overall, the contact pressure history is similar for explicit 1-way contact and implicit mortar contact although the peak pressure was slightly higher for implicit.

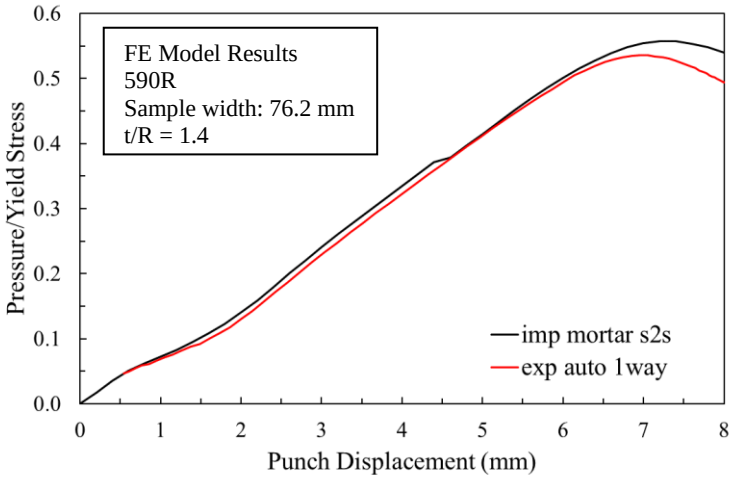

Figure 5-24 - Normalized interface pressure comparison, 1 mm mesh

5.3.5. Contact Area Convergence Study

The contact area output from LS-DYNA is discontinuous but should improve with mesh refinement of the surface area of the elements. Refining the blank mesh to improve the contact area data is an option but as seen in Section 5.3.2 the strain localizes earlier with decreasing mesh size. The load-displacement response will also change as discussed in Section 5.3.1. Instead, the mesh of the punch can be refined which reduces computational cost compared to refining the blank as the punch can be idealized as rigid or elastic. Punch mesh sizes with element sizes ranging from 0.05 – 0.2 mm were considered with the sizes tabulated in Table 5-4 and visualized in Figure 5-25.

Table 5-4 - Punch mesh element sizes

Length (mm)	Width (mm)	Abbreviation
0.2	0.2	0.2 × 0.2
0.1	0.2	0.1 × 0.2
0.1	0.1	0.1 × 0.1
0.05	0.2	0.05 × 0.2
0.05	0.1	0.05 × 0.1
0.05	0.05	0.05 × 0.05

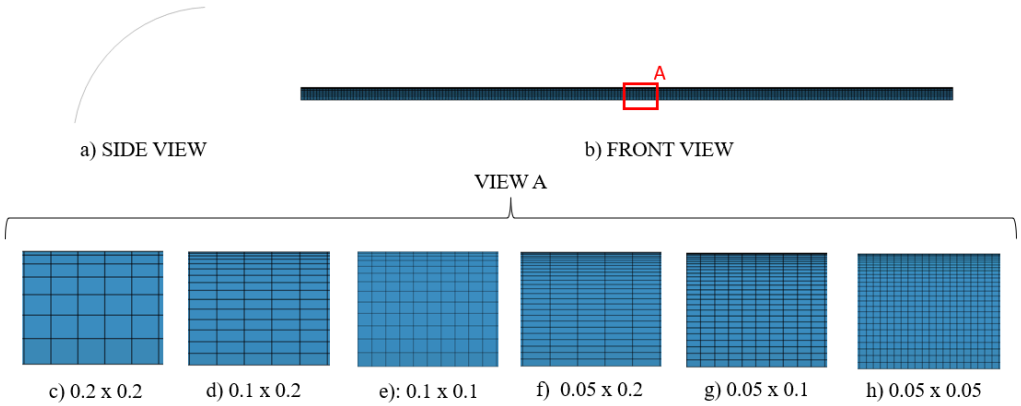

Figure 5-25 - Punch mesh detail for contact area convergence study

The contact areas extracted from LS-DYNA for the various punch mesh sizes is shown in Figure 5-26 where there is approximate convergence for element lengths of 0.05 mm for widths of 0.05 to 0.20 mm.

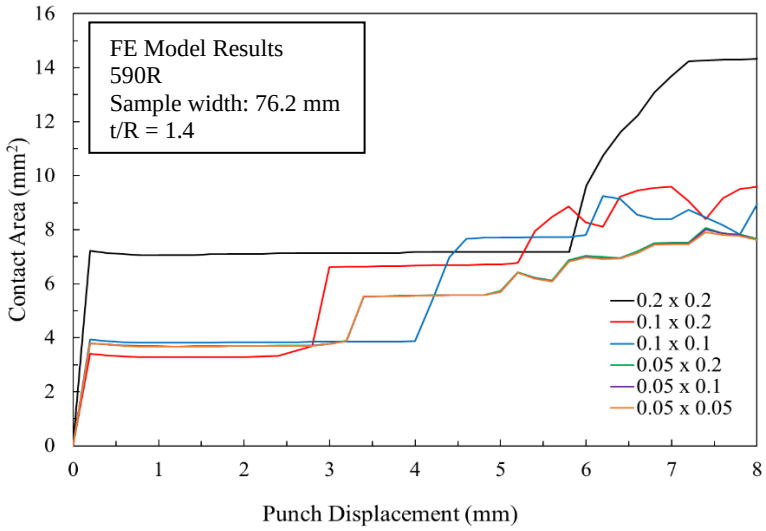

Figure 5-26 - Punch contact area for various punch mesh sizes - raw data from LS-DYNA

5.3.6. Improving Simulation Contact Area Curves with Lines of Best Fit

The discontinuous contact area data extracted from LS-DYNA is not amenable for evaluating analytical models for the contact pressure. To estimate the underlying trend a cubic polynomial was selected and calibrated to the contact area history. The cubic equation for the contact area is

$$A_c = ad^3 + bd^2 + cd + A_0 \tag{5.3.4}$$

where d is the punch displacement, A_0 is the initial contact area, and a, b, c are the cubic coefficients. The trendlines are shown as dotted lines in Figure 5-27 and the cubic coefficients are shown in the Appendix.

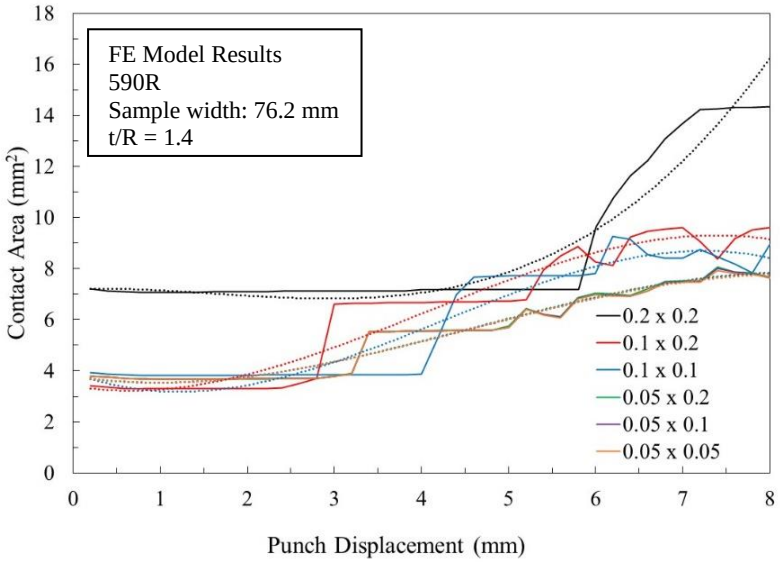

Figure 5-27 - Punch contact areas, trendlines dotted

To illustrate the effect of contact area and the cubic trendline on contact pressure, the normalized contact pressure of the 1.0×1.0 mm blank mesh and 0.05×0.2 mm punch mesh calculated with both the raw and cubic trendline contact area is shown in Figure 5-28 (plotted until experimental limit strain punch displacement). The benefit is clear for the contact pressure of the punch computed with the cubic trendline. It is noteworthy that the contact pressure of the blank and punch differs by a factor of 5. For subsequent simulations in this chapter, the punch mesh size of 0.05×0.2 mm was used and the punch contact area calculated using the cubic trendline.

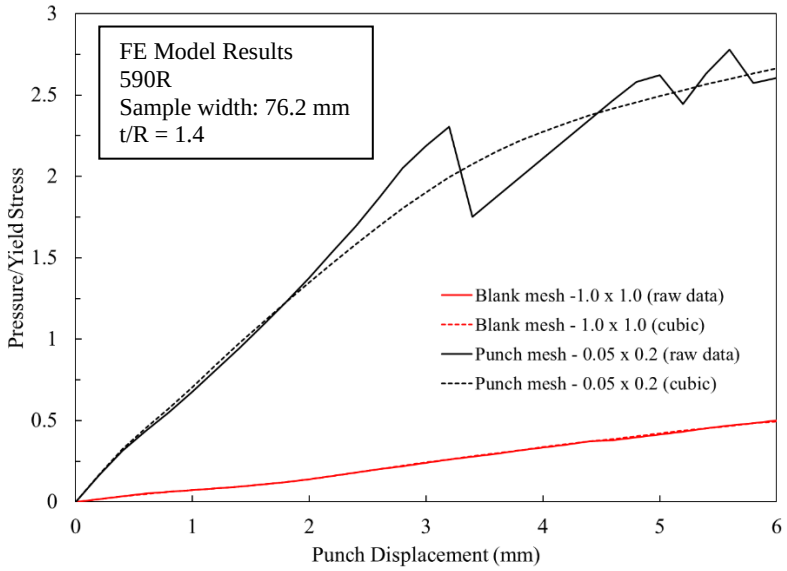

Figure 5-28 - Contact pressure comparison of raw simulation data and cubic trendline method - blank mesh vs. punch mesh

5.4. Investigation of Through-thickness Strain and Contact Pressure

The objective of this section is to revisit the process corrections of Min et al. [17], that were applied experimentally in Chapter 4, using finite-element analysis to evaluate their validity. The effect of an elastic punch was also investigated as it is expected to affect contact pressure. Two bend severities were investigated (with the same die gap width) using the 76.2 mm sample geometry and a 1.4 mm sample thickness. The sample thickness was set to 1.4 mm to achieve the same $t/R = 1.4$ and $t/R = 0.14$ ratios as in the experiments with the corresponding punch sizes. Two power-law materials with different hardening rates were used (Eq. (5.1.1) in Section 5.1.1.) with the von Mises yield criterion. The simulation details are tabulated in Table 5-5.

Table 5-5 - Power-law simulation details (gap width 30 mm)

Gap width – punch radius (mm)	t/R	n-value	Punch material	Abbreviation
30 - 1	1.4	0.1	rigid	30-1_n=0.1_rigid
30 - 1	1.4	0.1	elastic	30-1_n=0.1_elastic
30 - 1	1.4	0.3	rigid	30-1_n=0.3_rigid
30 - 1	1.4	0.3	elastic	30-1_n=0.3_elastic
30 - 10	0.14	0.1	rigid	30-10_n=0.1_rigid
30 – 10	0.14	0.1	elastic	30-10_n=0.1_elastic
30 – 10	0.14	0.3	rigid	30-10_n=0.3_rigid
30 – 10	0.14	0.3	elastic	30-10_n=0.3_elastic

5.4.1. Comparison of Load-displacement Response

The load-displacement response and limit strains are shown in Figure 5-29. The tabulated limit strains are provided in the Appendix.

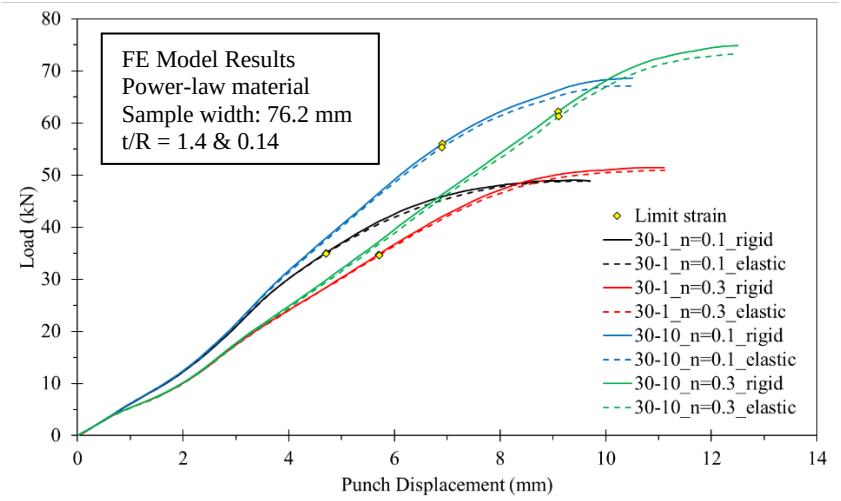

Figure 5-29 - Load-displacement response and limit strains of all power-law material simulations

The effect of elastic tooling is negligible on the load-displacement response which was expected given that the load response did not appear to be sensitive to the finite-element parameters

such as the mesh size. However, it is expected to play a larger role upon the local contact pressure history of the blank on the inner layer used in the process corrections.

5.4.2. Through-thickness Major Strain Distributions

To obtain a through-thickness snapshot of the major strain distribution, four states were plotted for each simulation that correspond to 25%, 50%, 75% and 100% of the limit strain punch displacement. These states are referred to as d_1, d_2, d_3, and LBF respectively, and the punch displacement values are shown in the Appendix. The through-thickness major strain distribution was plotted against the normalized thickness defined as

$$t_{norm} = \frac{y}{t} \tag{5.4.1}$$

where *y* is the thickness coordinate and *t* is the current thickness. The concave or bottom surface in contact with the punch corresponds to y = 0.

The through-thickness major strain distributions for the $t/R = 1.4$ simulations are shown in Figure 5-30 and Figure 5-31 and the $t/R = 0.14$ simulations are shown in Figure 5-32 and Figure 5-33.

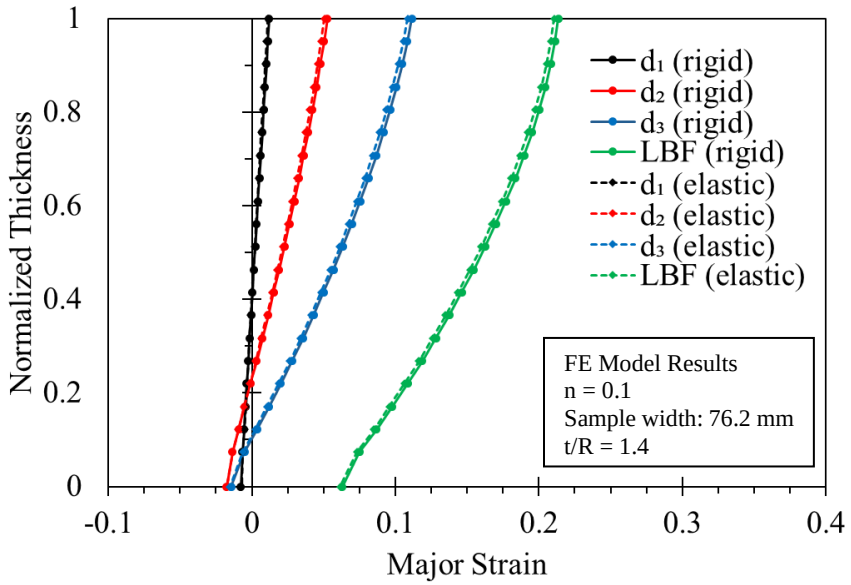

Figure 5-30 - Through-thickness major strain distribution, n=0.1, t/R=1.4

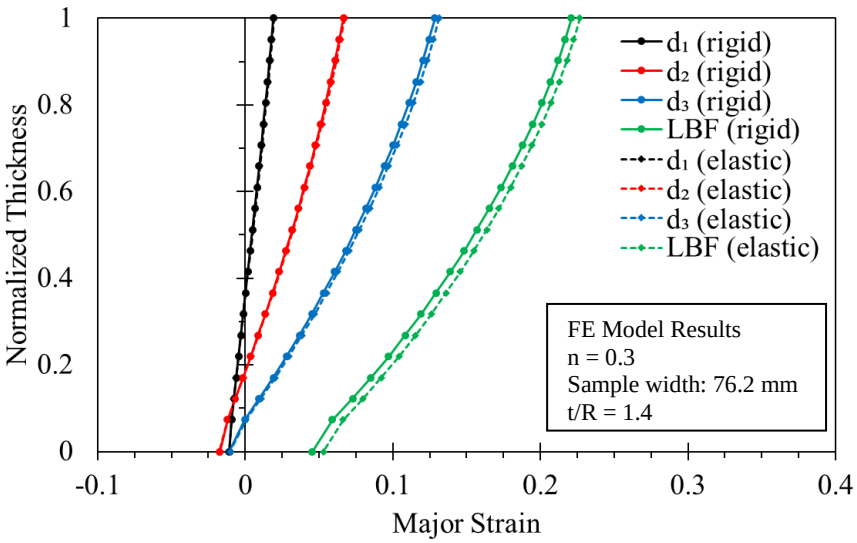

Figure 5-31 - Through-thickness major strain distribution, n=0.3, t/R=1.4

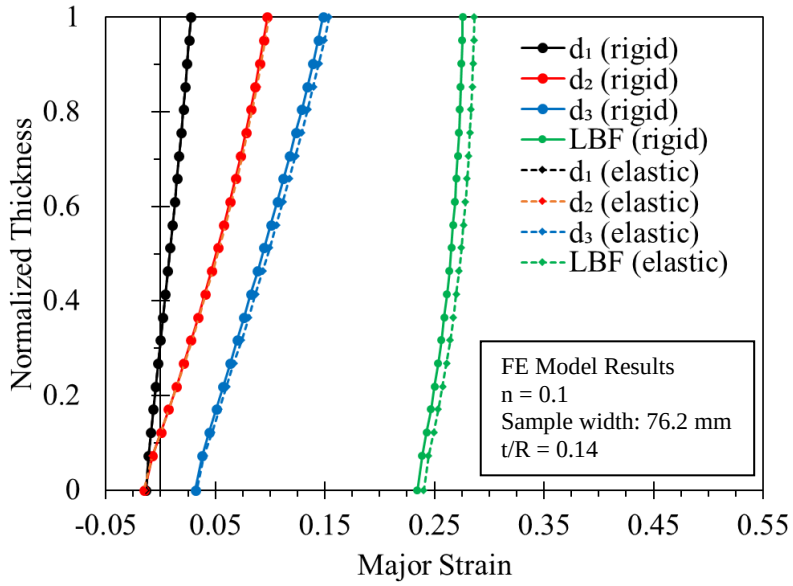

Figure 5-32 - Through-thickness major strain distribution, n=0.1, t/R=0.14

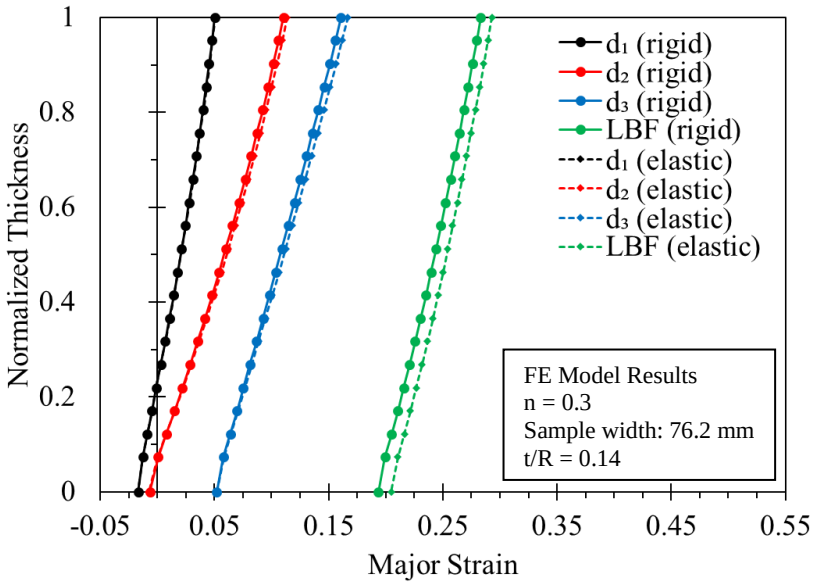

Figure 5-33 - Through-thickness major strain distribution, n=0.3, t/R=0.14

For the $n = 0.1$ material with $t/R = 1.4$, the difference in through-thickness major strain distribution produced by rigid vs. elastic tooling is negligible. For the $n = 0.3$ material with $t/R = 1.4$, the major strain is higher through-the-thickness at higher deformation levels (limit strain) with the elastic tooling. The through-thickness major strain distribution of the $n = 0.3$ material shows a higher degree of non-linearity relative to the $n = 0.1$ material. These same trends are observed

for the $t/R = 0.14$ simulations. When comparing the through-thickness strain distribution of high bend severity to lower bend severity, the distribution is less non-linear. This is an expected trend as more non-linearity in the strain distribution is expected as the bend severity increases.

The effect of elastic tooling in the ASBT with $t/R = 1.4$ or $t/R = 0.14$ on the through-thickness major strain distribution is only significant for a relatively high ductility material (power-law material with $n = 0.3$ vs. $n = 0.1$ in this case) at larger strains. As expected, the non-linearity of the strain distribution increases with increasing bend severity.

5.4.3. Strain Path on Middle and Inner Layers of the Sheet

A method to calculate the strains on the middle and inner layers of the sheet was given by Min et al. [17] and was applied to experimental data in Chapter 4. The middle and inner layer strains produced by the model could not be experimentally verified and the model is investigated further here. The relevant equations are restated for convenience:

$$\varepsilon_i^{mid} = \varepsilon_i^{outer} + \ln\left(1 - \frac{t\kappa_i^{outer}}{2}\right) \tag{5.4.2}$$

$$\varepsilon_i^{inner} = \varepsilon_i^{outer} + \ln\left(1 - t\kappa_i^{outer}\right) \tag{5.4.3}$$

where the subscript *i* is either 1 or 2, representing major and minor directions respectively, *t* the thickness of the blank, and κ is the convex surface curvature.

The strain data for the outer surface is collected from the centre element at the top of the blank in the simulation. The strain and surface coordinate data are then used to calculate the curvature using the quadratic fit method and sheet thickness using the SB model (unless otherwise specified

a 20 mm fitting window was used). The strain model quantities were calculated using only data that would be available in an experiment using DIC strain measurement.

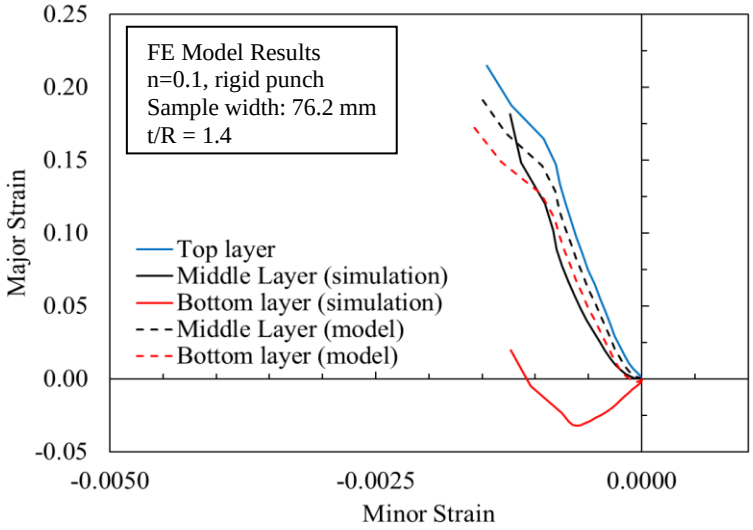

Figure 5-34 - Strain path on layers comparison, n=0.1, t/R=1.4, rigid punch

The strain comparison for the $n = 0.1$ material with a bend severity of 1.4 using the rigid punch is shown in Figure 5-34. The agreement between the strain model and simulation is poor. Notably, the strain model does not capture the strain reversal that occurs on the bottom surface, and the magnitude of the major strain on the bottom layer is severely overpredicted. In general, the strain model strain paths appear as scaled versions of the outer strain path, and no characteristics of the differing strain path on the middle and inner layers are captured.

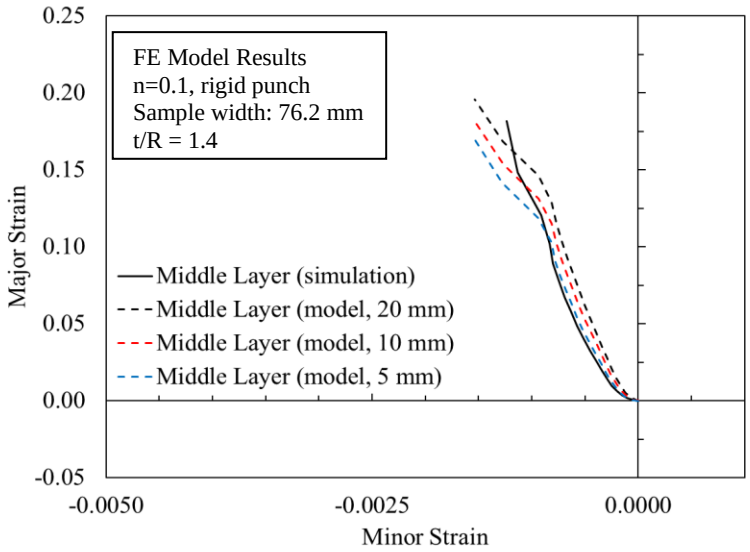

Figure 5-35 - Effect of fitting interval on strain model, n=0.1, t/R=1.4, rigid punch

The effect of the fitting window on the strain model is shown in Figure 5-35 ($n = 0.1, t/R = 1.4$, rigid punch), with the simulation values shown as a reference (middle layer only from Figure 5-34). The strain model is sensitive to the fitting interval with respect to the magnitude of strains predicted. However, all the strain paths have the same characteristics of the outer layer (see Figure 5-34).

To gain further insight to the effectiveness of the quadratic fit method to obtain the curvature, the quadratic fits were overlaid over the simulation coordinate data at the limit strain for the $n = 0.1$ material with the rigid punch. The results are shown for $t/R = 1.4$ in Figure 5-36 and $t/R = 0.14$ in Figure 5-37. The quadratic fit of the $t/R = 1.4$ simulation in Figure 5-36 shows noticeable variation between the 20 mm fitting window recommended by Min et al. [17] from bulge testing, and the two smaller fitting windows of 10 and 6 mm. For the $t/R = 0.14$ simulation in Figure 5-37, all three fitting windows provide good agreement with the simulation data. Overall, the 20 mm fitting window appears to be the best out of the three windows tested; future work using higher bend severities may require a smaller fitting window.

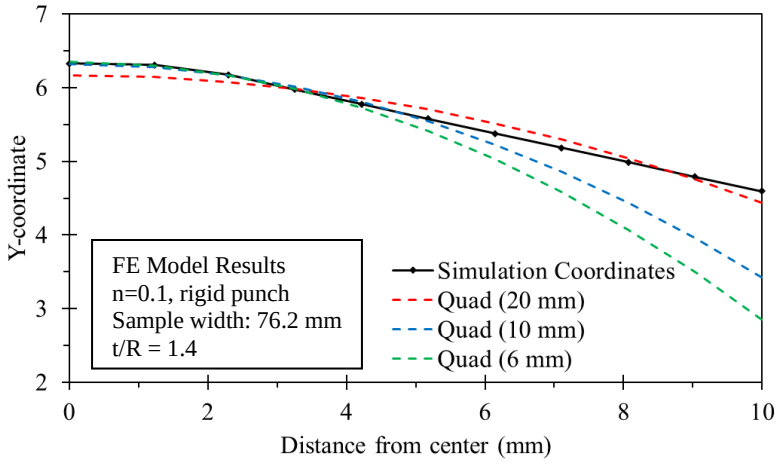

Figure 5-36 - Simulation coordinate data and quadratic fits, n=0.1, t/R=1.4, rigid punch

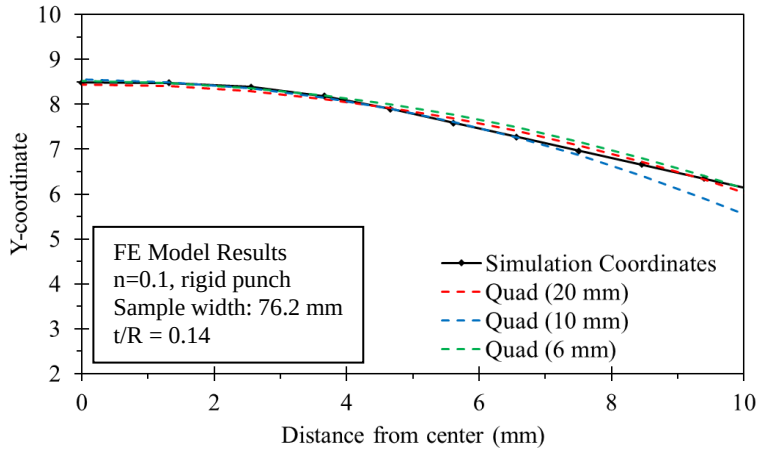

Figure 5-37 - Simulation coordinate data and quadratic fits, n=0.1, t/R=0.14, rigid punch

Shown in Figure 5-38 is the $n = 0.1$ material ($t/R = 1.4$) with the elastic punch. The difference of both the simulation and model strains are negligible between the rigid and elastic punches (corresponding test condition with rigid punch shown in Figure 5-34), and the strain model shows no improvement with respect to the rigid punch simulations.

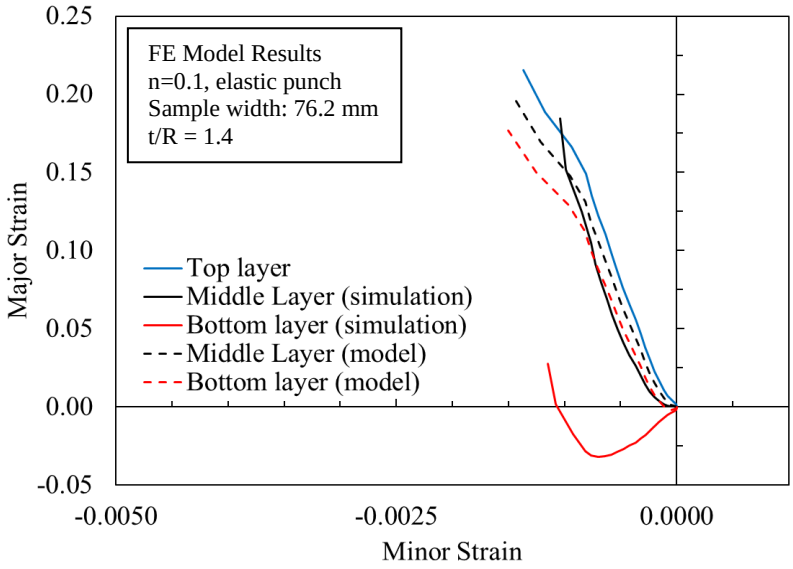

Figure 5-38 - Strain path on layers comparison, n=0.1, t/R=1.4, elastic punch

The strain path on the layers for the $n = 0.1$ material with a bend severity of 0.14 using the rigid punch is shown in Figure 5-39. The same trends are observable when compared to the higher bend severity of 1.4 shown in Figure 5-34; the strain model is in poor agreement with the simulation. The bottom layer strain reversal is not captured by the strain model, and the magnitude of the major strain is underpredicted by a non-negligible amount for both the middle and bottom layers.

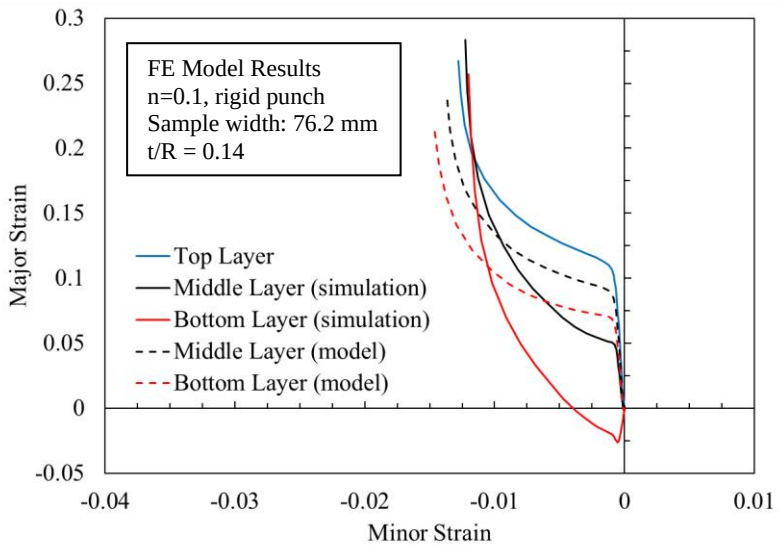

Figure 5-39 - Strain path on layers comparison, n=0.1, t/R=0.14, rigid punch

The strain projection model produces strain paths on the middle and inner layers that are scaled versions of the outer layer strain path. The simulation shows markedly different strain paths in both magnitude and curvature and adjusting the fitting window does not improve the model. Thus, the strain projection model is not recommended for the ASBT.

5.4.4. Contact Pressure Model Investigation

Contact pressure is highly dependent on the calculation of the contact area in the simulation. The use of a rigid punch in the simulations does not account for small deformations of the tool which affects the contact area. Thus, the effect of a rigid and elastic punch on contact pressure was investigated and compared with the predictions of the analytical model of Min et al. [17]. The punch mesh size was set to 0.05×0.2 mm for the rigid shell element punch based on the contact area convergence study in Section 5.3.5. The elastic punch used solid elements. The raw data for the punch contact areas are shown in Figure 5-40 and the corresponding trendlines which were used for calculating contact pressure are shown in Figure 5-41. The tabulated punch contact area and trendlines for each simulation are shown in the Appendix.

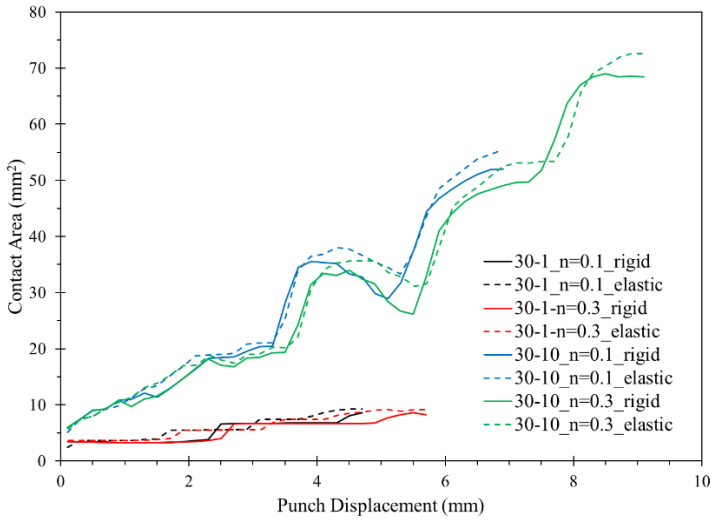

Figure 5-40 - Punch contact area for rigid/elastic tooling simulations

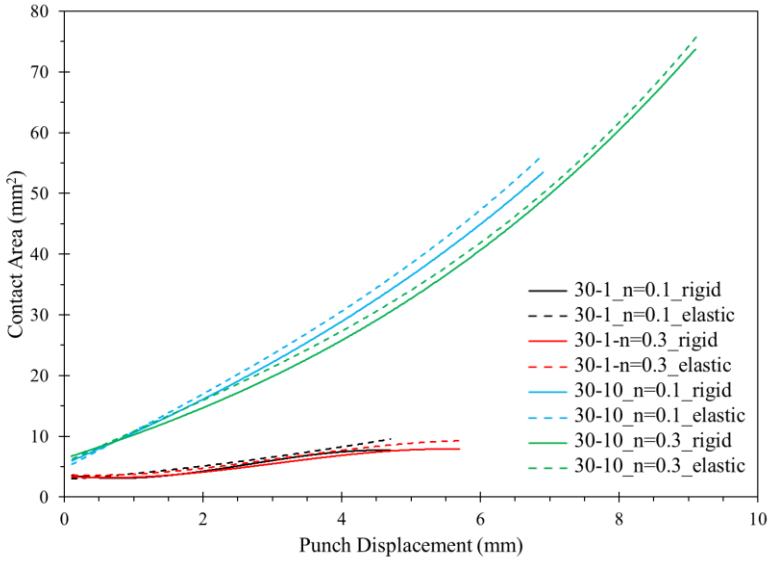

Figure 5-41 - Punch contact area trendlines for rigid/elastic tooling simulations

The contact pressure normalized by the yield stress is shown for the $t/R = 1.4$ and $t/R = 0.14$ cases in Figure 5-42 and Figure 5-43 respectively.

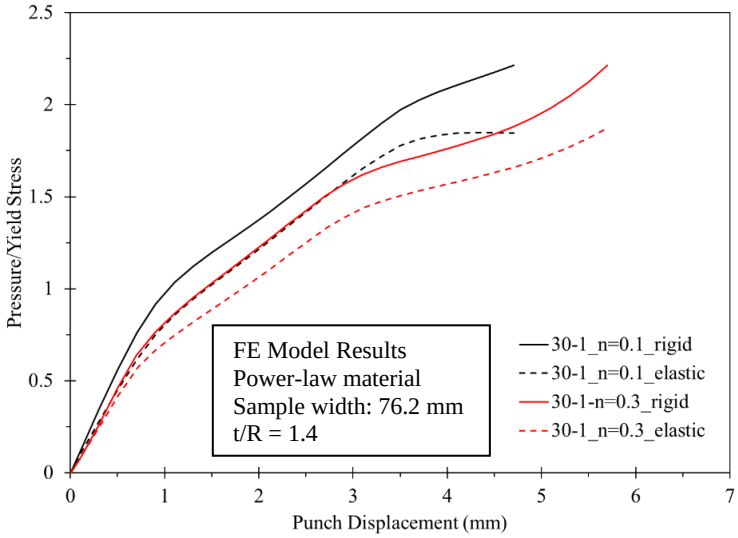

Figure 5-42 - Normalized contact pressure, t/R = 1.4 Simulations

The contact pressure differs significantly between the rigid and elastic punch. Recall that the punch load was similar for the rigid and elastic tooling in Section 5.4.1. It is the deformation of the elastic punch with its increased contact area that produces the lower contact pressure.

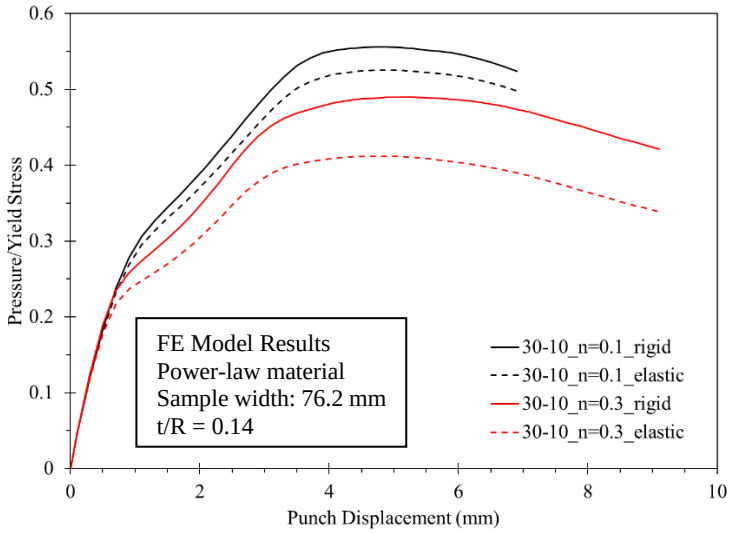

Figure 5-43 - Normalized contact pressure, t/R = 0.14 Simulations

To compare the two power-law materials, the simulation pressure was normalized by the flow stress and plotted against the equivalent plastic strain of the element at the convex surface at the apex of the bend. The results are shown in Figure 5-44 and Figure 5-45 for the rigid and elastic

tooling respectively. Generally, the simulation contact pressure normalized by the flow stress shows relative agreement between both materials for each bend severity. Future work could involve verifying if the contact pressures of materials normalized by the flow stress are in general agreement at the same bend severity.

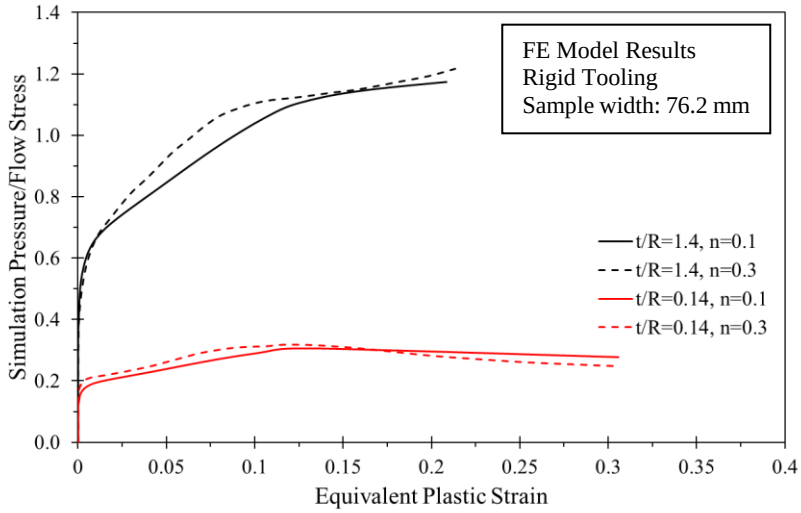

Figure 5-44 - Simulation pressure normalized by flow stress, rigid tooling simulations

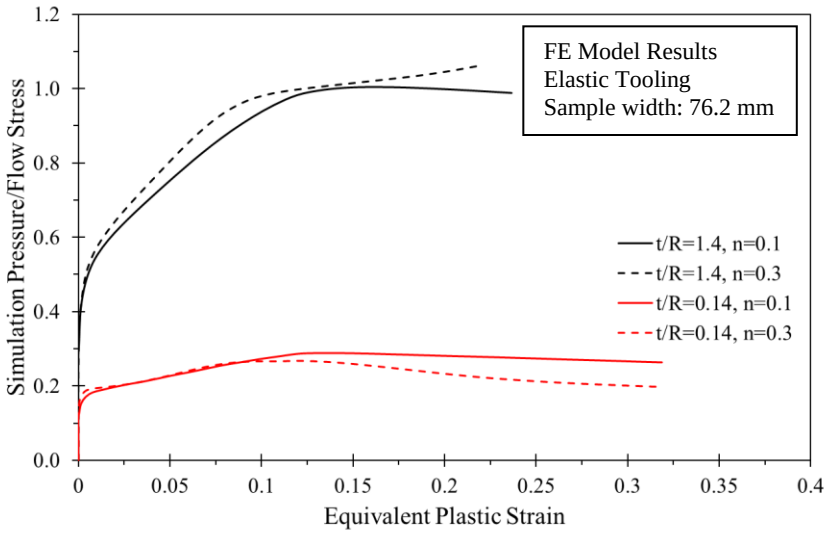

Figure 5-45 - Simulation pressure normalized by flow stress, elastic tooling simulations

The contact pressure predicted by the analytical model of Min et al. [17] , henceforth referred to as the 'Min model, was provided in Chapter 4, Eq. (4.5.6). For convenience, the contact pressure equation is restated here

$$\sigma_3 = \sigma_1 \left\{ \frac{t}{R_1^O}\left(1+\frac{t}{2R_2^O}\right) - \frac{t\alpha}{R_2^O}\left(1+\frac{t}{2R_1^O}\right)\right\} \tag{5.4.4}$$

Three fitting windows were used relative to the 30 mm die gap width: $2/3$, $1/3$, $1/5$, which correspond to 20, 10, and 6 mm respectively. Based on Eq. (5.4.4) if only the fitting window is changed, the thickness value from the SB model will remain very similar as shown in Chapter 4. Since the ASBT has nominally zero curvature in the minor strain direction, the limit of Eq. (5.4.4) as $R_2^O \to \infty$ can be taken to gain insight to the behaviour of the Min model with varying the fitting window:

$$\sigma_3(R_2^O \to \infty) = \sigma_1 \left\{ \frac{t}{R_1^O} \right\} \tag{5.4.5}$$

The Min model predicts a linear relationship between the contact stress and bend severity such that a larger fitting window size will effectively reduce the contact pressure by increasing the radius. Shown in Figure 5-46 and Figure 5-47 is the contact pressure comparison for the $n = 0.1$ material using the rigid and elastic punch respectively. The Min model underpredicts the simulation pressure significantly and is not suitable for use at a bend severity of 1.4. The dependence of the Min model on the fitting window of the radius is also clear.

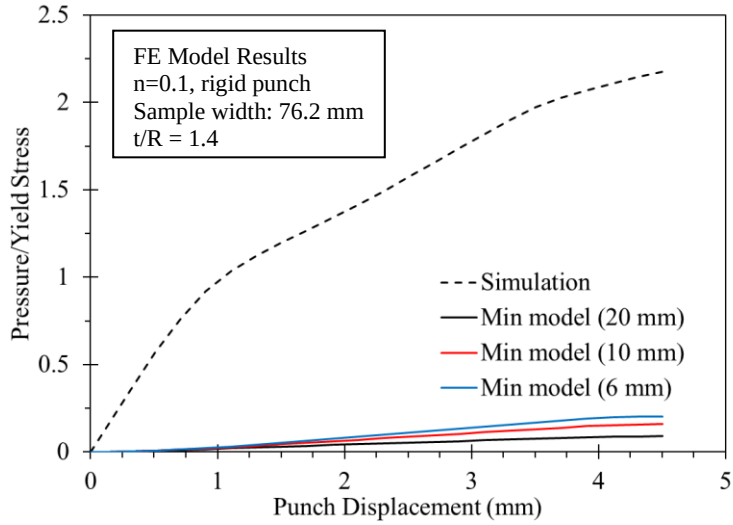

Figure 5-46 - Simulation vs. Min model contact pressure, n=0.1, t/R=1.4, rigid punch

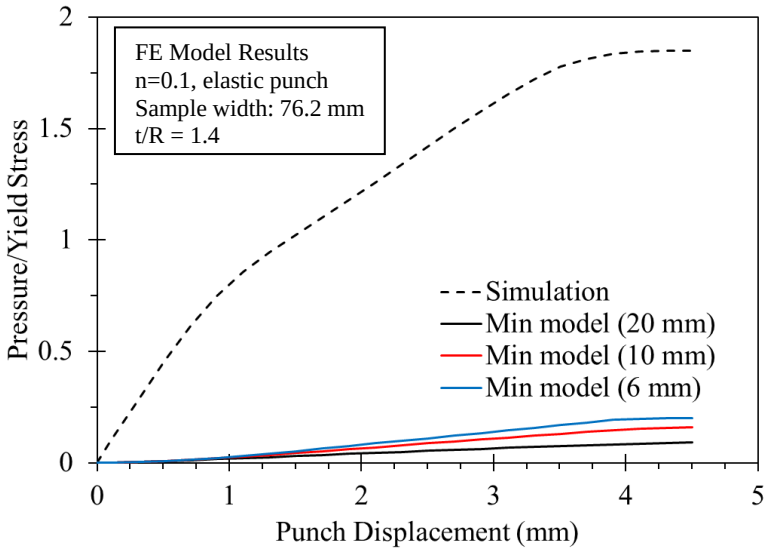

Figure 5-47 - Simulation vs. Min model contact pressure, n=0.1, t/R=1.4, elastic punch

The pressure comparison for the $n = 0.3$ material with a bend severity of 1.4 with the rigid and elastic punch is shown in Figure 5-48 and Figure 5-49 respectively. The simulation data shows contact pressure multiple orders of magnitude greater than the Min model for all test conditions at a bend severity of 1.4. Based on the simulation data, the Min model should not be used for the ASBT when the bend severity is 1.4 or greater $(t/R \geq 1.4)$.

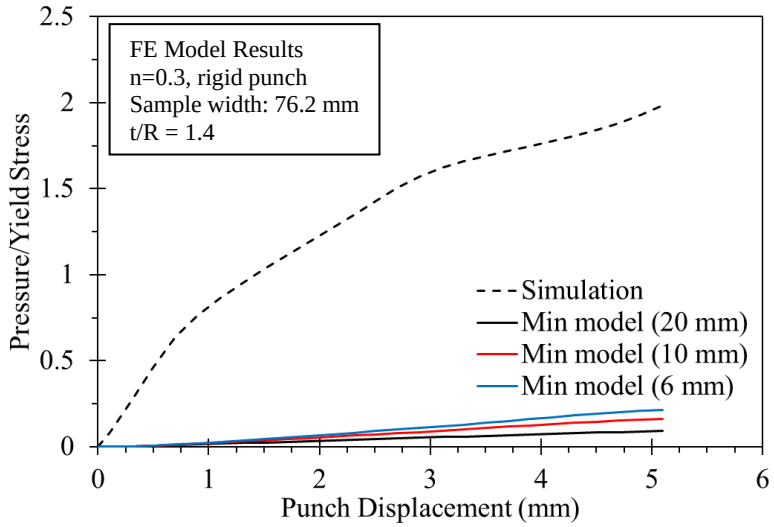

Figure 5-48 - Simulation vs. Min model contact pressure, n=0.3, t/R=1.4, rigid punch

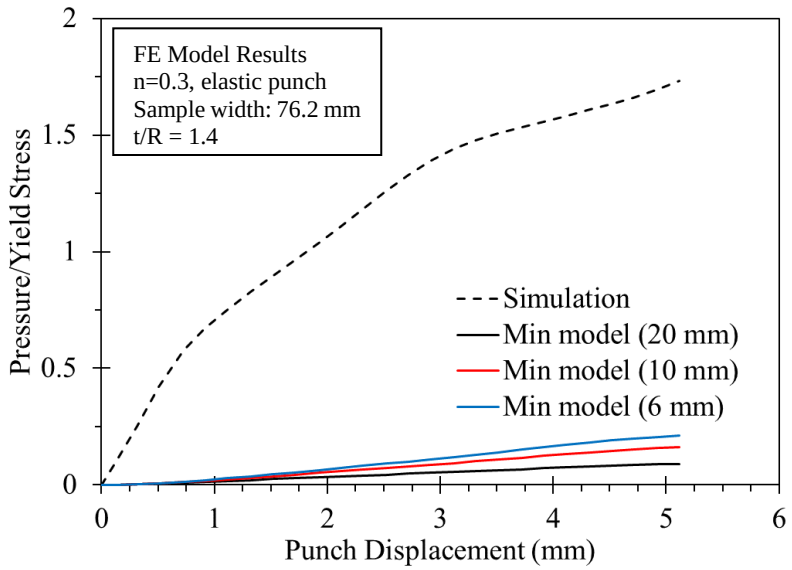

Figure 5-49 - Simulation vs. Min model contact pressure, n=0.3, t/R=1.4, elastic punch

Shown in Figure 5-50 and Figure 5-51 is the $n = 0.1$ material with a bend severity of 0.14 using the rigid and elastic punch respectively. The Min model predicted pressures are much closer in magnitude to the simulation pressure compared to the bend severity of 1.4 but the agreement between simulation data and the Min model is poor.

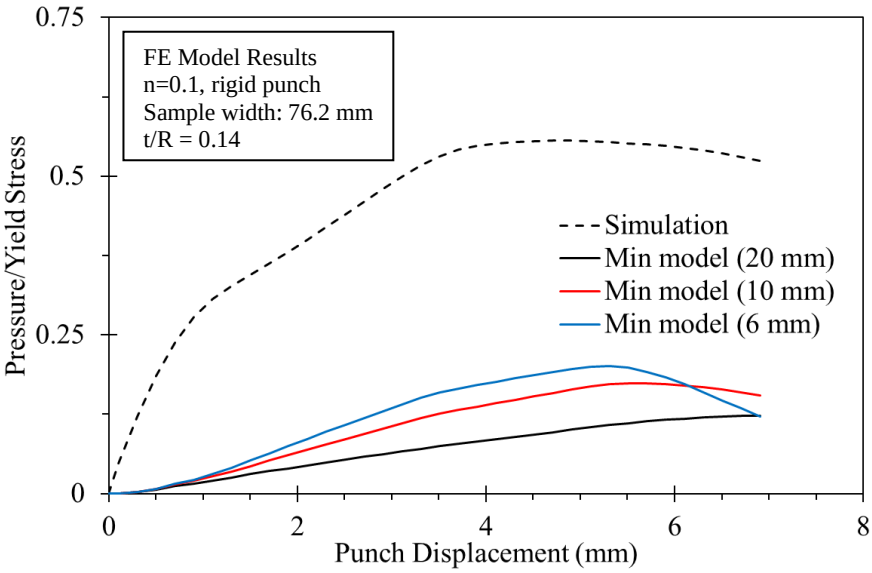

Figure 5-50 - Simulation vs. Min model contact pressure, n=0.1, t/R=0.14, rigid punch

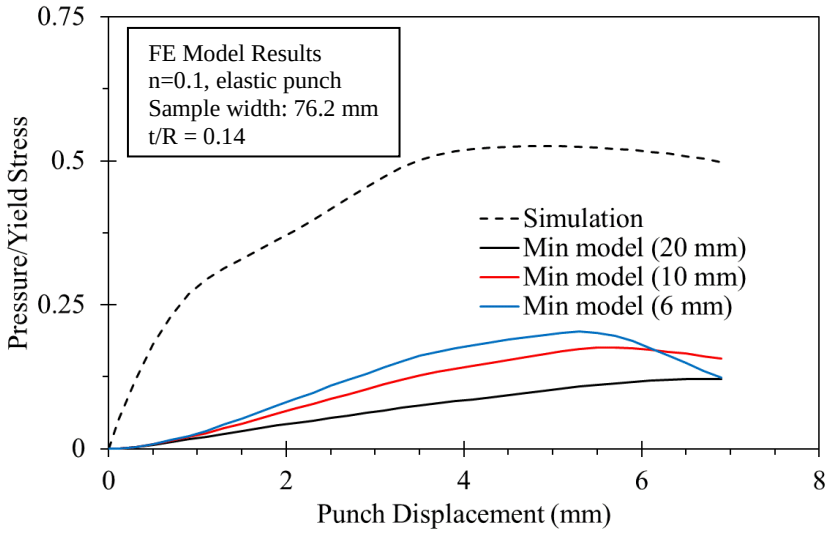

Figure 5-51 - Simulation vs. Min model contact pressure, n=0.1, t/R=0.14, elastic punch

Shown in Figure 5-52 and Figure 5-53 is the $n = 0.3$ material with a bend severity of 0.14 using the rigid and elastic punch respectively. The results are similar to the $n = 0.1$ material and the sensitivity of the model to the fitting window is evident, as the curvature change using the smallest fitting window produces a drop in pressure near the limit strain.

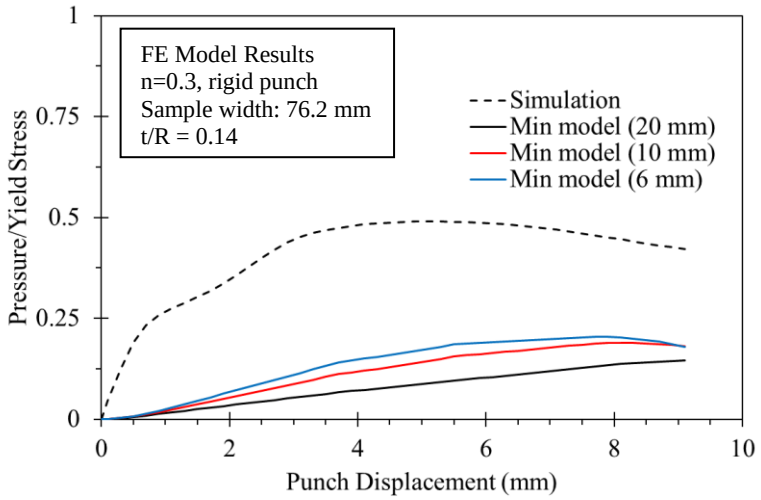

Figure 5-52 - Simulation vs. Min model contact pressure, n=0.3, t/R=0.14, rigid punch

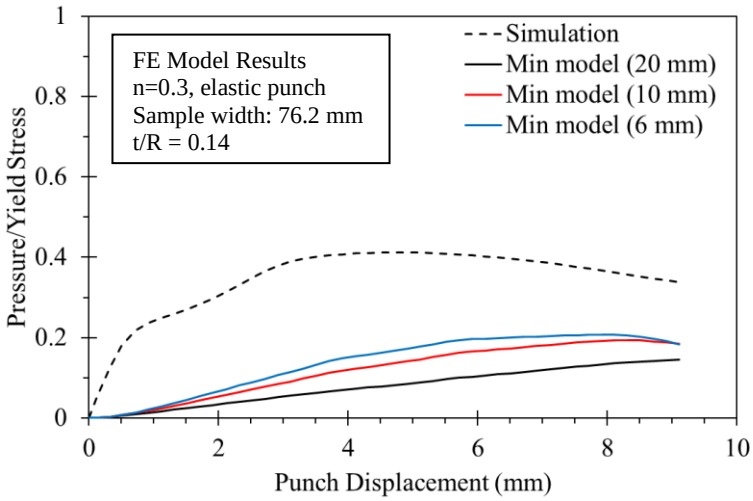

Figure 5-53 - Simulation vs. Min model contact pressure, n=0.3, t/R=0.14, elastic punch

5.4.5. Alternative Pressure Model Investigation - Hertz Contact Pressure

Due to the poor agreement between the Min model and contact pressure obtained from the finite-element models, it was decided to also consider the Hertz contact pressure model. The Hertz contact pressure model has an intuitive physical basis, and implementation of the model is straightforward although it was derived for elastic isotropic materials and not plastic forming. The ASBT resembles the Hertz solution for a cylinder in contact with another cylinder on its inner

surface which is shown in Figure 5-54a. Figure 5-54b shows a schematic of the ASBT overlaid with the Hertz radii. The Hertz expression for the contact shown in Figure 5-54a is

$$\sigma_3 = \sigma_z = \frac{-P_{\max}}{\sqrt{1 + z^2 / b^2}} \tag{5.4.6}$$

$$P_{\max} = \frac{2F}{\pi b l}, \tag{5.4.7}$$

$$b = \sqrt{\frac{4F}{\pi l} \frac{\left(1-\nu_1^2\right)/E_1 + \left(1-\nu_2^2\right)/E_2}{1/R_1 + 1/\left(-R_2\right)}}, \tag{5.4.8}$$

where b and l are the width and length of the contact area respectively, F is the contact force, and z is the coordinate through the thickness. The subscripts 1 and 2 denote the punch and blank respectively. Note the negative sign on the punch radius which denotes contact on an inner cylinder as shown in Figure 5-54. Therefore, equation (5.4.6) can be expressed as a function of z, where $\sigma_3(0)$ and $\sigma_3(1)$ yield the bottom and top surface pressures respectively.

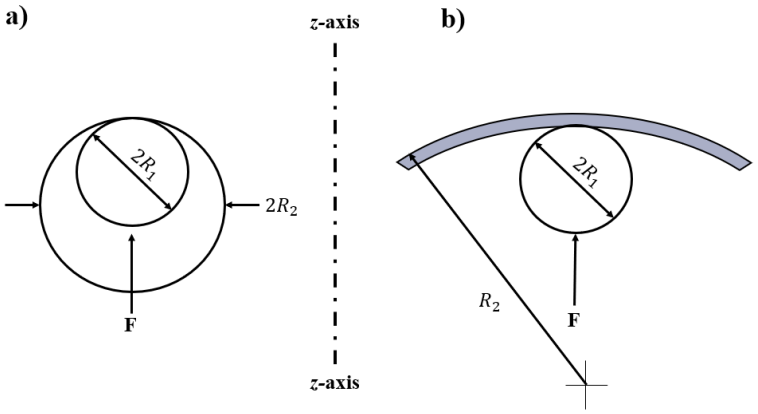

Figure 5-54 - Hertz contact pressure: a) cylinder contact with inner cylinder. b) schematic of ASBT

As a first approximation, the elastic constants of the punch and blank, and the punch force from the simulation are directly substituted into equations (5.4.6)-(5.4.8). The Hertz pressure

model predicts very high pressure with respect to the simulation as shown in Figure 5-55. Three fitting windows were used to calculate the radius of curvature R_2 in Eq. (5.4.8) and had negligible effects on the Hertz pressure model.

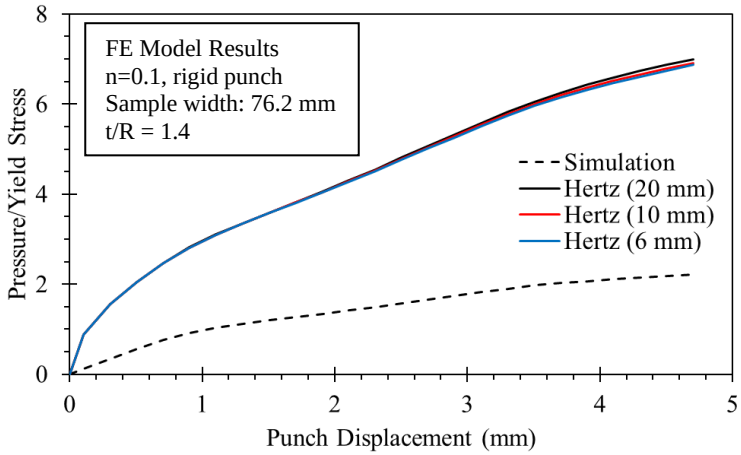

Figure 5-55 - Simulation pressure vs. Hertz, n=0.1, t/R=1.4, rigid punch

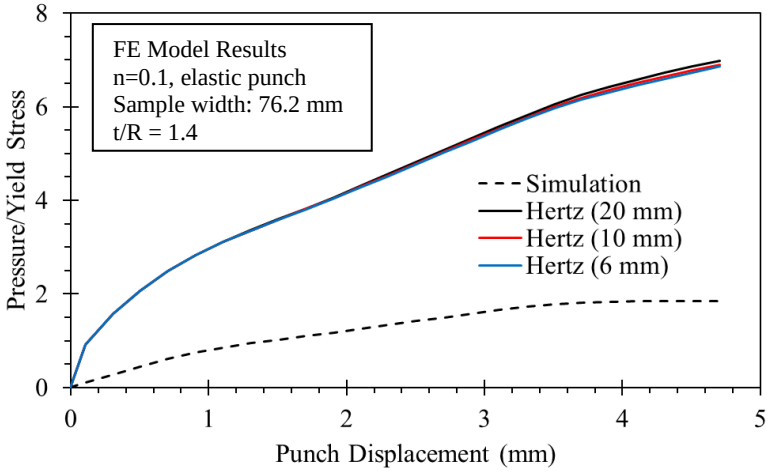

Figure 5-56 - Simulation pressure vs. Hertz, n=0.1, t/R=1.4, elastic punch

It was hypothesized that substituting the hardening rate for the modulus of elasticity - term E_2 in equation (5.4.8) - would provide more realistic contact pressures. In other words, the Hertz contact pressure is expected to decrease when the term E_2 becomes smaller since *b* is proportional to $\sqrt{1/E_2}$ and the pressure is inversely proportional to *b*.

As a first step in validating the hypothesis above, the value of E_2 is solved for by using the pressure from the finite-element model and working backwards using the Hertz equations. Comparing the computed E_2 value to the analytical hardening rate will determine if the hypothesis is valid. The process for computing E_2 was:

1) Using the simulation pressure and force values, rearrange equation (5.4.7) to solve for the half-width of contact, *b*
2) Rearrange equation (5.4.8) to solve for E_2
3) Use the equivalent plastic strain value from the simulation (top element at the centre)
4) Compare simulation calculated E_2 parameter vs. equivalent plastic strain with the actual hardening rate of the power-law model used (either $n = 0.1$ or $n = 0.3$)

The hardening rate of the power-law hardening model shown in equation (5.1.1) is

$$\frac{d\bar{\sigma}}{d\varepsilon_{eq}^{p}} = Kn\left(\varepsilon_{eq}^{p}\right)^{n-1}. \tag{5.4.9}$$

The method above was performed on the $n = 0.1$ material with $t/R = 1.4$ for rigid and elastic tooling and the results are shown in Figure 5-57.

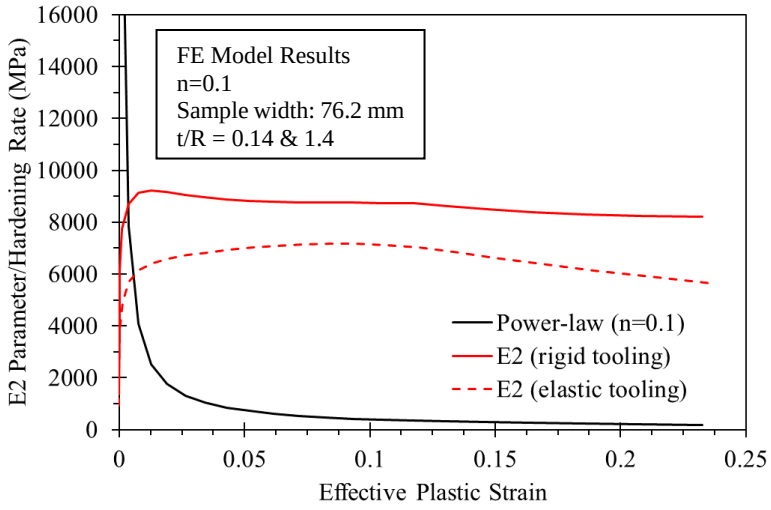

Figure 5-57 - Power-law and E_2 parameter comparison, n = 0.1 material

The differences between the power-law hardening rate and the calculated E_2 parameter are significant for both materials and both bend severities. The E_2 parameter for both materials was dissimilar when comparing the rigid and elastic tooling. The agreement between the E_2 parameter and analytical hardening rate is poor. However, the relatively consistent value of the backwards calculated E_2 parameter suggests that a constant value of E_2 would be a reasonable approximation for the contact pressure.

A first approximation for a constant value of E_2 was taken as the average of the back-calculated E_2 values from above (Figure 5-57) from 0.002 plastic strain up to the limit strain. This average value was then substituted into Eq. (5.4.8) to calculate the Hertz pressure which is denoted as modified Hertz pressure in Figure 5-58 and Figure 5-59 for the $n = 0.1$ material, and Figure 5-60 and Figure 5-61 for the $n = 0.3$ material. The approximation using the average of the back-calculated E_2 provides a very close result to the simulation pressure. The lower bend severity for both rigid and elastic tooling show much better agreement than the Min model.

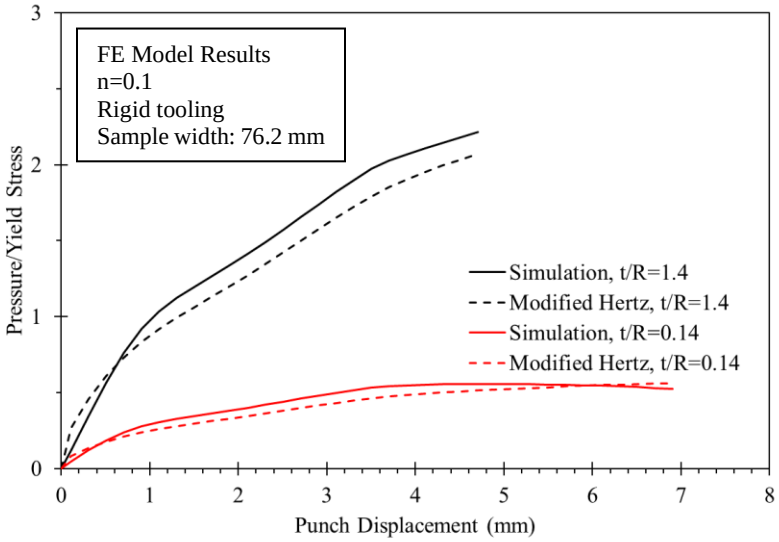

Figure 5-58 - Simulation and Modified Hertz Pressure, n=0.1 material, rigid tooling

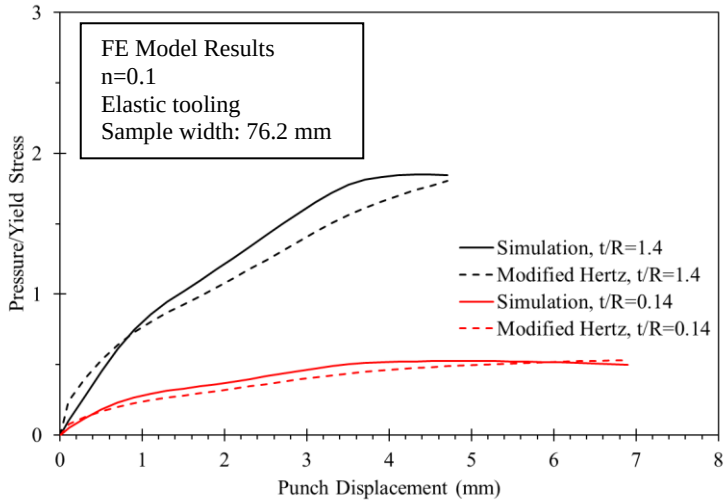

Figure 5-59 - Simulation and modified Hertz pressure, n=0.1 material, elastic tooling

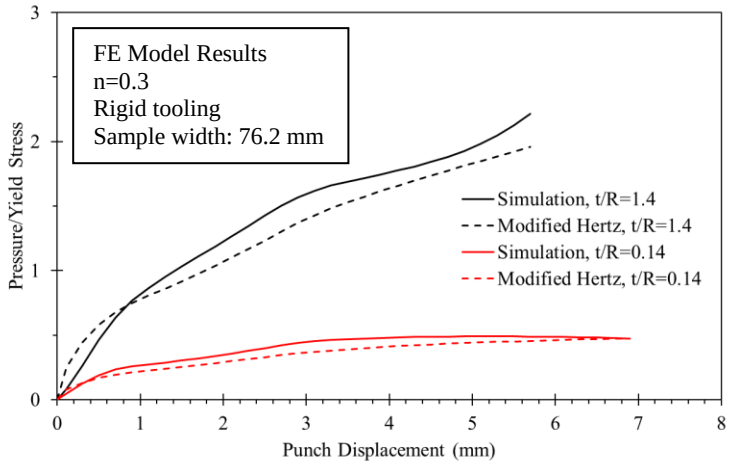

Figure 5-60 – Simulation and modified Hertz pressure, n=0.3 material, rigid tooling

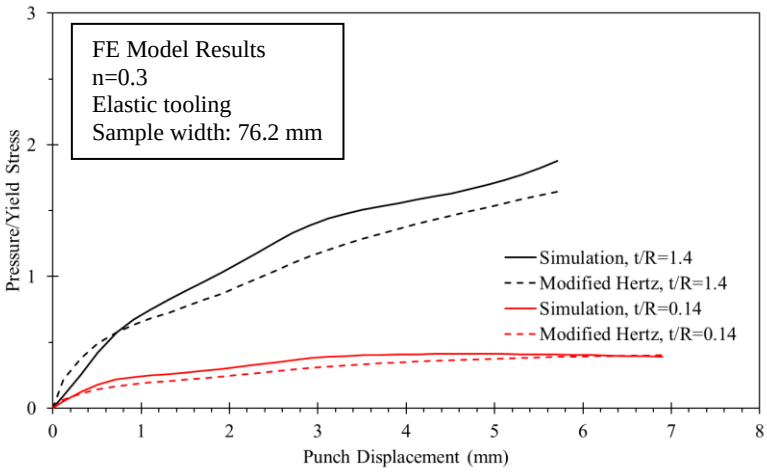

Figure 5-61 – Simulation and modified Hertz pressure, n=0.3 material, elastic tooling

The average values for the effective E_2 , denoted as E_2^* parameter for all cases considered re shown below in Table 5-6.

Table 5-6 – Average E_2 parameter

t/R	n-value	Tooling type	E_2^*
1.4	0.1	Elastic	6550.58
1.4	0.3	Elastic	5506.23
0.14	0.1	Elastic	6683.35
0.14	0.3	Elastic	4846.93
1.4	0.1	Rigid	8686.64
1.4	0.3	Rigid	7840.16
0.14	0.1	Rigid	7354.14
0.14	0.3	Rigid	6621.96

6. Conclusions and Recommendations

6.1. Conclusions

The current work focused upon the mechanics of the angular stretch bend test for formability characterization with an emphasis upon finite-element analysis and evaluation of models in the literature to convert between in-plane and out-of-plane forming limit curves. The experimental work focused upon the characterization of three grades of automotive steel: 590R, DP980, and 3rd Gen 1180.

Analytical models were evaluated in the ASBT that calculate curvature, thickness, through-thickness strain gradients, compensate for non-linear strain path and contact pressure. The curvature and thickness models were found to be suitable for the ASBT while the non-linear strain path corrections appeared to be negligible for the bend severities considered. The strain gradient and contact pressure models were not able to be experimentally verified and were subject to further analysis using finite element simulation. Overall, the analytical models for the strain at the middle and concave (inner layers) along with the contact pressure were in poor agreement with the simulation data. The errors were substantial in the contact pressure with it significantly underestimating the magnitude of the pressure.

Although there were less test conditions for the 3rd Gen 1180 and DP980 relative to the 590R, there is high confidence that the conclusions stated above are transferable for various materials and test conditions. The curvature model is not material dependent, and the SB model relies only on the surface strain distribution and the curvature and good agreement with experimental data is expected for a wide range of materials and bend severities. In the case of NLSP, the NLSP corrections are negligible at the bend severities tested, and the same results would be expected

using the 3rd Gen 1180 and DP980 with identical test conditions to the 590R. One exception is the contact pressure model, where a trend of underprediction of the limit strains was evident when decreasing the die gap width.

The finite element model of the ASBT was developed by first determining the number of elements required through-the-thickness using solid elements. Shell elements were not suitable to model the ASBT at bend severities of unity or higher. The choice of contact algorithm in LS-DYNA and implicit solver was evaluated against common alternatives and rigid and elastic tooling was compared. The use of elastic tooling had a negligible effect on the load and through-thickness strain distribution but had significant effect on contact pressure.

The following specific conclusions from this thesis can be drawn:

1) The bend severity (t/R) affected the experimental strain paths while the die gap width had a negligible effect on strain path.
2) To reduce the effect of tool contact pressure, larger gap sizes may be used. Note that this will have a negligible effect on strain path if the bend severity is held constant.
3) The load-displacement response is not a suitable metric to evaluate the finite-element model as it was relatively insensitive to mesh size and could be well predicted, for specific bend severities, using shell elements. The through-thickness strain distributions must be used with a recommended minimum density of 10 elements per millimeter for a bend severity of unity.
4) The quadratic fit method for obtaining surface curvature provides good agreement with the blank side-profile and is simple to implement, however, consistency of the fitting window should be enforced when comparing results.

5) The new proposed SB model for obtaining the thickness provides excellent agreement with experimental data and is suitable for use with the ASBT. Alternatively, the so-called curvature method for obtaining thickness proposed by Min et al. [17], [28] is also suitable for use with the ASBT.
6) The NLSP corrections produced small to negligible changes to the unmodified limit strains. It is recommended to avoid the NLSP due to the additional uncertainty it adds and its related assumptions.
7) The pressure corrections of Min et al. [17] had moderate success at converting the experimental ASBT limit strains to that of the in-plane forming limit curve. Interestingly, the agreement was best for a bend severity of 1.4 while the corrections were overestimated for a bend severity of 0.28 and 0.14. Despite the general agreement, the use of the process corrections for ASBT is discouraged. The results were inconsistent across the three die gap widths, and the finite-element simulations revealed the Min model drastically underestimated the contact pressure.
8) The strain calculation given by Min et al. [17] to produce the middle and inner layer strains could not be verified experimentally and produced poor agreement with the simulation. Therefore, the strain projection method of Min et al. [17] is not recommended for the ASBT.
9) The Hertz contact pressure model using an effective constant modulus for deformation of the blank was able to give realistic predictions of the contact pressure with respect to the simulation contact pressure.

6.2. Recommendations

1) At the time of writing no industry accepted standard similar to ISO-12004-2 [8] regarding limit strain detection for the ASBT has been published, and the method defined in ISO-12004-2 [8]. The LBF method provided consistent result across multiple bend severities for three different grades of steel and is recommended for limit strain detection for the ASBT.
2) The 590R was used across a wide range of test conditions, and conclusions were drawn on the effect of die gap width based on these experiments. More materials with varying properties (i.e., ductility) should be tested in a similar manner.
3) Curvature acquisition is paramount when applying the process-correction models used in this thesis. The strain and pressure models were shown to be sensitive to the curvature values (due to using different fitting windows). If too large, the fitting window will not accurately capture the curvature near the center of the blank. In extreme cases where the fitting window was small, the formation of a neck valley may be detected which would result in curvature decreasing. In this thesis, a 20 mm fitting window provided good agreement but should be revisited in future work to determine if it is appropriate across different punch geometries and bend severities.
4) The effect of elastic tooling in the simulations on contact pressure was significant. Elastic tooling should be used in ASBT simulation where contact pressure is studied. The punch mesh should be as fine as is practical as it will increase the accuracy of the contact pressure data.
5) The modified Hertz contact pressure model seems promising when using an average E_2 parameter. Future work could involve finding a correlation for the average E_2 parameter

with respect to t/R and n as discussed in Section 5.4.5.Elastic tooling is recommended to perform any such correlation.

References

[1] M. Shome and M. Tumuluru, *Welding and Joining of Advanced High Strength Steels*, 1st ed. Woodhead Publishing, 2015.

[2] C. D. Horvath, "Advanced Steels for Lightweight Automotive Structures," in *Materials, Design, and Manufacturing for Lightweight Vehicles*, 1st ed., P. K. Mallick, Ed. Woodhead Publishing, 2010, pp. 35–78.

[3] T. B. Hilditch, T. de Souza, and P. D. Hodgson, "Properties and Automotive Applications of Advanced High-strength Steels," in *Welding and Joining of Advanced High Strength Steels*, Woodhead Publishing, 2015, pp. 9–28.

[4] D. Banabic, *Sheet Metal Forming Processes - Constituitive Modelling and Numerical Simulation*. Springer, 2010.

[5] S. P. Keeler, "Determination of forming limits in automotive stampings," *SAE Tech. Pap.*, 1965, doi: 10.4271/650535.

[6] G. M. Goodwin, "Application of strain analysis to sheet metal forming problems in the press shop," *SAE Tech. Pap.*, pp. 380–387, 1968, doi: 10.4271/680093.

[7] S. K. Paul, "Theoretical analysis of strain- and stress-based forming limit diagrams," *J. Strain Anal. Eng. Des.*, vol. 48, no. 3, pp. 177–188, 2013, doi: 10.1177/0309324712468524.

[8] "ISO 12004-2 Metallic materials - Sheet and strip - Determination of forming-limit curves." International Organization for Standardization, 2008.

[9] W. Volk and P. Hora, "New algorithm for a robust user-independent evaluation of beginning instability for the experimental FLC determination," *Int. J. Mater. Form.*, vol. 4,

no. 3, pp. 339–346, Sep. 2011, doi: 10.1007/s12289-010-1012-9.

[10] J. Noder, J. Dykeman, and C. Butcher, “New Methodologies for Fracture Detection of Automotive Steels in Tight Radius Bending: Application to the VDA 238–100 V-Bend Test,” *Exp. Mech.*, 2020, doi: 10.1007/s11340-020-00627-z.

[11] F. M. Neuhauser, O. Terrazas, N. Manopulo, P. Hora, and C. Van Tyne, “The bending dependency of forming limit diagrams,” *Int. J. Mater. Form.*, vol. 12, no. 5, pp. 815–825, 2019, doi: 10.1007/s12289-018-1452-1.

[12] M. R. Tharrett and T. B. Stoughton, “Stretch-bend forming limits of 1008 AK steel,” *SAE Tech. Pap.*, no. 724, 2003, doi: 10.4271/2003-01-1157.

[13] D. Kitting, A. Ofenheimer, H. Pauli, and E. T. Till, “Experimental characterization of stretch-bending formability of AHSS sheets,” *AIP Conf. Proc.*, vol. 1353, no. April, pp. 1589–1594, 2011, doi: 10.1063/1.3589743.

[14] D. Morales-Palma, C. Vallellano, and F. J. García-Lomas, “Assessment of the effect of the through-thickness strain/stress gradient on the formability of stretch-bend metal sheets,” *Mater. Des.*, vol. 50, pp. 798–809, Sep. 2013, doi: 10.1016/j.matdes.2013.03.086.

[15] D. K. Cheong, “On the Influence of the Through-Thickness Strain Gradients for Characterization of Formability and Fracture of Sheet Metal Alloys,” University of Waterloo, 2019.

[16] D. Kitting, M. Koplenig, A. Ofenheimer, H. Pauli, and E. T. Till, “Application of a ‘Concave-Side Rule’ approach for assessing formability of stretch-bent steel sheets,” *Int. J. Mater. Form.*, vol. 2, no. SUPPL. 1, pp. 427–430, 2009, doi: 10.1007/s12289-009-0483-z.

[17] J. Min, T. B. Stoughton, J. E. Carsley, and J. Lin, “Compensation for process-dependent effects in the determination of localized necking limits,” *Int. J. Mech. Sci.*, vol. 117, pp. 115–134, Oct. 2016, doi: 10.1016/j.ijmecsci.2016.08.008.

[18] J. Noder and C. Butcher, “A comparative investigation into the influence of the constitutive model on the prediction of in-plane formability for Nakazima and Marciniak tests,” *Int. J. Mech. Sci.*, vol. 163, no. February, 2019, doi: 10.1016/j.ijmecsci.2019.105138.

[19] J. Noder, “Plastic Instability and Failure of Sheet Metals Subjected to Complex Stress States by,” University of Waterloo, 2022.

[20] J. E. Gutierrez, J. Noder, and C. Butcher, “Experimental characterization and deterministic prediction of in-plane formability of 3rd generation advanced high strength steels,” *Metals (Basel).*, vol. 10, no. 7, pp. 1–34, 2020, doi: 10.3390/met10070902.

[21] C. Butcher, F. Khameneh, A. Abedini, D. Connolly, and S. Kurukuri, “On the experimental characterization of sheet metal formability and the consistent calibration of the MK model for biaxial stretching in plane stress,” *J. Mater. Process. Technol.*, vol. 287, no. September 2020, p. 116887, 2021, doi: 10.1016/j.jmatprotec.2020.116887.

[22] J. Noder, J. E. Gutierrez, A. Zhumagulov, J. Dykeman, H. Ezzat, and C. Butcher, “A Comparative Evaluation of Third-Generation Advanced High-Strength Steels for Automotive Forming and Crash Applications,” *Materials (Basel).*, vol. 14, 2021.

[23] T. Rahmaan, A. Abedini, C. Butcher, N. Pathak, and M. J. Worswick, “Investigation into the shear stress, localization and fracture behaviour of DP600 and AA5182-O sheet metal alloys under elevated strain rates,” *Int. J. Impact Eng.*, vol. 108, pp. 303–321, 2017, doi: 10.1016/j.ijimpeng.2017.04.006.

[24] F. Barlat *et al.*, “Plane stress yield function for aluminum alloy sheets - Part 1: Theory,” *Int. J. Plast.*, vol. 19, no. 9, pp. 1297–1319, 2003, doi: 10.1016/S0749-6419(02)00019-0.

[25] A. Abedini, J. Noder, C. P. Kohar, and C. Butcher, “Accounting for Shear Anisotropy and Material Frame Rotation on the Constitutive Characterization of Automotive Alloys using Simple Shear Tests,” *Mech. Mater.*, vol. 148, no. February, p. 103419, 2020, doi: 10.1016/j.mechmat.2020.103419.

[26] J. E. Gutierrez, “Private correspondence.” 2020.

[27] J. Noder, “Private correspondence.” 2019.

[28] J. Min, T. B. Stoughton, J. E. Carsley, B. E. Carlson, J. Lin, and X. Gao, “Accurate characterization of biaxial stress-strain response of sheet metal from bulge testing,” *Int. J. Plast.*, vol. 94, pp. 192–213, Jul. 2017, doi: 10.1016/j.ijplas.2016.02.005.

[29] R. F. Young, J. E. Bird, and J. L. Duncan, “An automated hydraulic bulge tester,” *J. Appl. Metalwork.*, vol. 2, no. 1, pp. 11–18, Jul. 1981, doi: 10.1007/BF02833994.

[30] K. Yoshida, “Evaluation of Stress and Strain Measurement Accuracy in Hydraulic Bulge Test with the Aid of Finite-element Analysis,” *ISIJ Int.*, vol. 53, no. 1, pp. 86–95, 2013, doi: 10.2355/isijinternational.53.86.

[31] ISO, “ISO 16808:2014 - Metallic materials — Sheet and strip — Determination of biaxial stress-strain curve by means of bulge test with optical measuring systems,” 2014.

[32] Z. Marciniak, J. L. Duncan, and S. J. Hu, *Mechanics of Sheet Metal Forming*, 2nd Ed. Butterworth-Heinemann, 2002.

[33] MATLAB, “MATLAB.” The Mathworks, Inc, Natick, Massachusetts, 2020.

[34] J. D'Errico, "SLM - Shape Language Modelling." MATLAB Central File Exchange, 2022.

[35] P. Hora, L. Tong, and B. Berisha, "Modified maximum force criterion, a model for the theoretical prediction of forming limit curves," *Int. J. Mater. Form.*, vol. 6, no. 2, pp. 267–279, 2013, doi: 10.1007/s12289-011-1084-1.

[36] L. M. Smith, R. C. Averill, J. P. Lucas, T. B. Stoughton, and P. H. Matin, "Influence of transverse normal stress on sheet metal formability," *Int. J. Plast.*, vol. 19, no. 10, pp. 1567–1583, 2003, doi: 10.1016/S0749-6419(02)00035-9.

[37] "LS-DYNA." ANSYS/LST, 2020.

[38] "HyperMesh." Altair Engineering, 2020.

[39] Livermore Software Technology Corporation (LSTC), *Theory Manual*, vol. 19. California: Livermore Software Technology Corporation.

[40] T. Belytschko, J. I. Lin, and T. Chen-Shyh, "Explicit algorithms for the nonlinear dynamics of shells," *Comput. Methods Appl. Mech. Eng.*, vol. 42, no. 2, pp. 225–251, Feb. 1984, doi: 10.1016/0045-7825(84)90026-4.

[41] T. Belytschko, C. S. Tsay, and W. K. Liu, "A STABILIZATION MATRIX FOR THE BILINEAR MINDLIN PLATE ELEMENT," 1981.

[42] A. Haufe, K. Schweizerhof, and P. Dubois, "Properties & Limits : Review of Shell Element Formulations," in *LS-DYNA Developer Forum*, 2013.

[43] C. Butcher, "Private correspondence." 2020.

[44] J. E. Gutierrez, N. Parker, J. Bowman, and J. Dykeman, "Formability Characterization of 3rd Generation Advanced High-strength Steel and Application to Forming a B-pillar," *SAE*

Tech. Pap., 2021, doi: 10.4271/2021-01-0267.Abstract.

APPENDIX A. Limit Strain Detection

ISO Method Limit Strain Applied to a Stretch Bend Experiment

Shown in Figure A-1 is the ISO method applied to a stretch bend experiment from this thesis. The fitting window does not provide an adequate representation of the strain gradient in the X-direction (coordinate perpendicular to the neck).

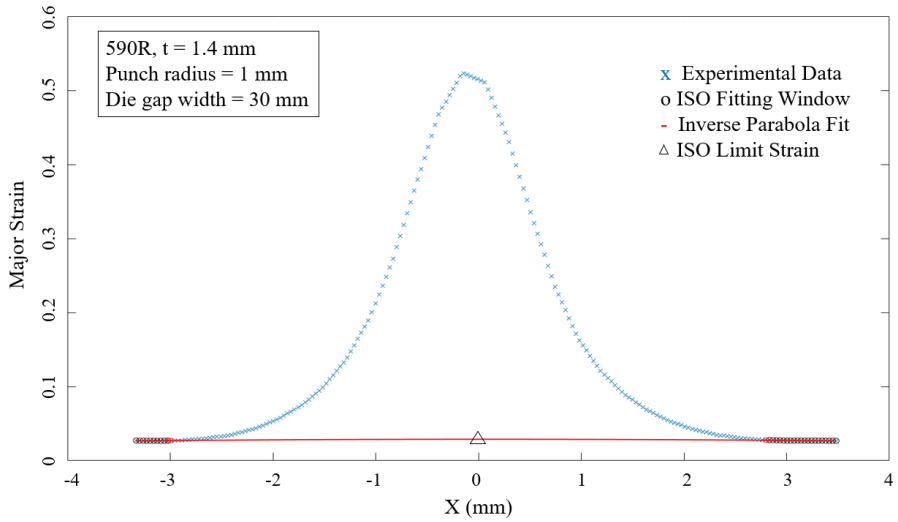

Figure A-1 - ISO method applied to an ASBT

APPENDIX B. Fracture Regularization

Fracture Regularization of the Angular Stretch Bend Test

In this section, fracture regularization is performed within LS-DYNA for the 3rd gen 1180 ASBT. Fracture regularization is a process where the load-displacement response is regularized across different mesh sizes. In LS-DYNA, the generalized incremental stress-state dependent damage model (GISSMO) is an phenomenological model that permits incremental damage accumulation such as softening or failure [39]. By scaling the fracture locus, regularization of the load-displacement response can be achieved with the GISSMO model.

Three test conditions are used for the fracture regularization which are shown below in Table B-1.

Table B-1 - Fracture regularization test conditions (3rd Gen 1180)

Gap width (mm)	Punch radius (mm)	t/R	Sample width (mm, inches)	Abbreviation
30	1	1.4	76.2, 3	3in-30-1
51	5	0.28	25.4, 1	1in-51-5
51	15	0.093	25.4, 1	1in-51-15

The fracture locus of the 3rd Gen 1180 [43] is shown in Figure B-1 and was used as input for the GISSMO model. The test conditions shown in Table B-1 are modeled using half symmetry (due to reduced computational cost of shell elements) and the LS-DYNA implicit solver was used. The yield criteria used was the Yld2000 yield function (see Table 2-4) and the constitutive model used was the modified Hockett-Sherby hardening model (see Table 2-2).

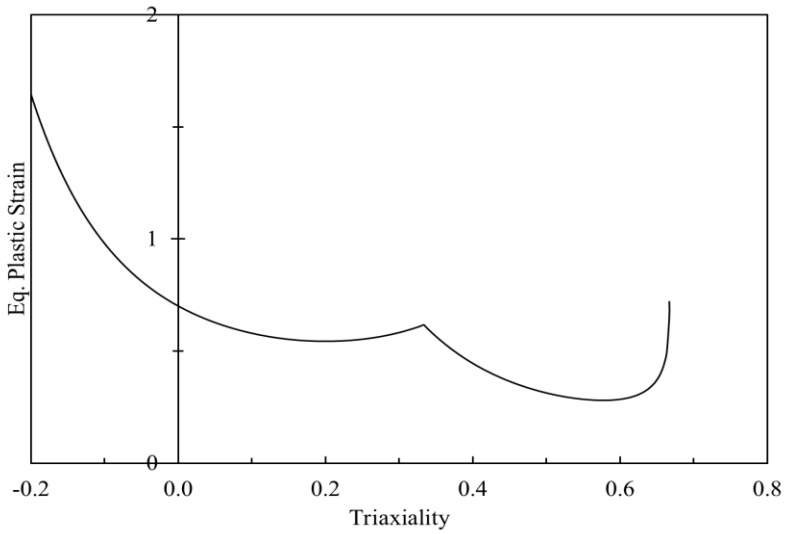

Figure B-1 - 3rd Gen 1180 fracture locus

The mesh sizes used for regularization were 0.5, 1, 2, 3, and 5 mm. The mesh was created such that the centre of the blank would consist of uniform, square elements. An example of the uniform region compared to the rest of the blank is shown for the 1 mm mesh size in Figure B-2.

The shell element type used was the type 16 shell element with IDOF set to 0 (default) and 5 integration points through the thickness. The regularization work shown here was completed as part of a research project where regularization was completed using type 16 shells.

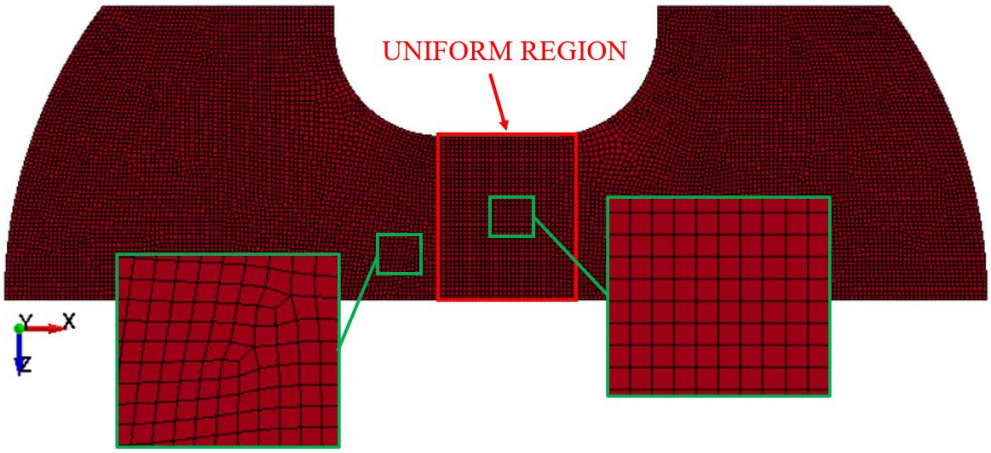

Figure B-2 - Regularization blank mesh details (1 mm)

For the GISSMO model, the number of shell integration points required for element failure was set to 80% (4 integration points).

The results of the regularization for the 76.2 mm sample, 30 mm gap width, and 1 mm punch are shown in Figure B-3, where 'sf' denotes the scale factor used. Even though the peak load is matched by scaling the fracture locus, the response of all the simulations is overly-stiff - the coarser the mesh, the stiffer the load-displacement response. This is due to the larger element sizes being unable to capture the bending accurately – for example the largest element size of 5 mm is five times as large as the punch radius. Another important takeaway is the large increase in regularization factor as the mesh size decreases. The regularization factor nearly doubles between the 1 and 0.5 mm mesh sizes.

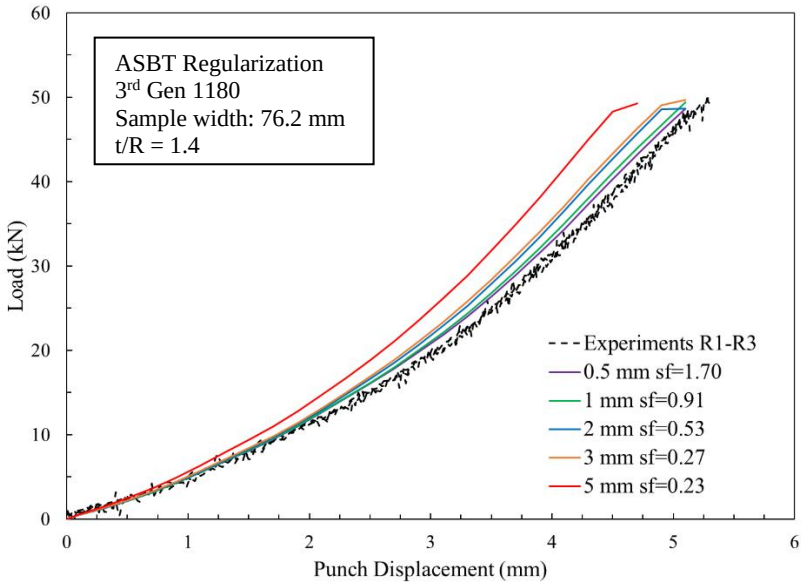

Figure B-3 - Load-displacement regularization (3in-30-1)

Shown in Figure B-4 is the results of the regularization for the 25.4 mm sample, 51 mm die gap width, and 5 mm punch. The 5 mm mesh size did not provide a suitable representation of the sample geometry and the results are not shown. The other mesh sizes show good agreement with the experiments, and notably the coarsest mesh size of 3 mm still retains good agreement with the experiments. Additionally, the regularization factor does not increase dramatically with decreasing mesh size; the 0.5 and 1 mm mesh use the same regularization factor!

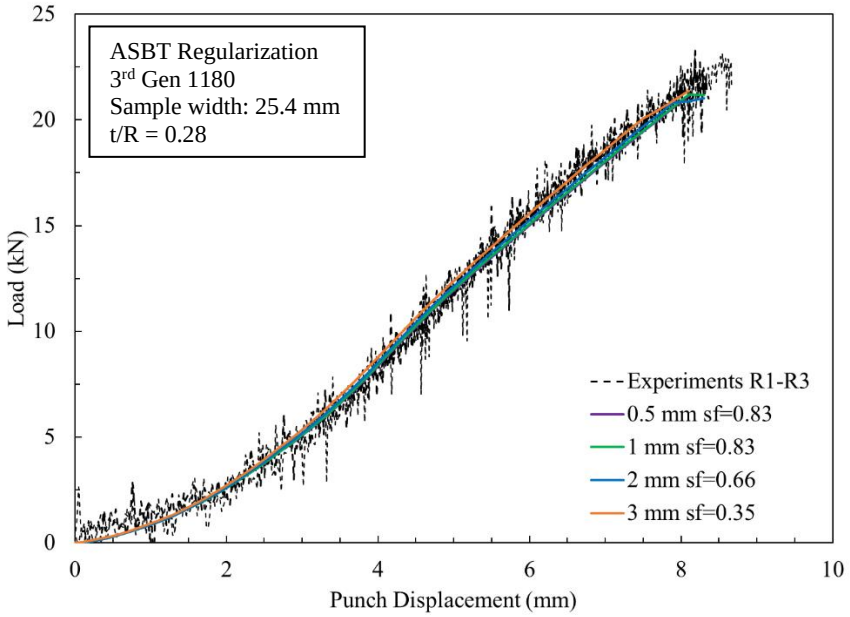

Figure B-4 - Load-displacement regularization (1in-51-5)

Shown in Figure B-5 is the results of the regularization for the 25.4 mm sample, 51 mm die gap width, and 15 mm punch. With the exception of the 5 mm mesh, all simulations provide good agreement with the experiments. Similar to the 3in-30-1 test condition, the 5 mm mesh produces an overly-stiff load-displacement response. Additionally, the regularization factor for the smallest 3 mesh sizes is identical, and the difference between the smallest and largest mesh regularization factor is much smaller than with the other two test conditions. The decreased bend severity provides a better case for the shell elements, and the regularization factor appears to converge at 0.5.

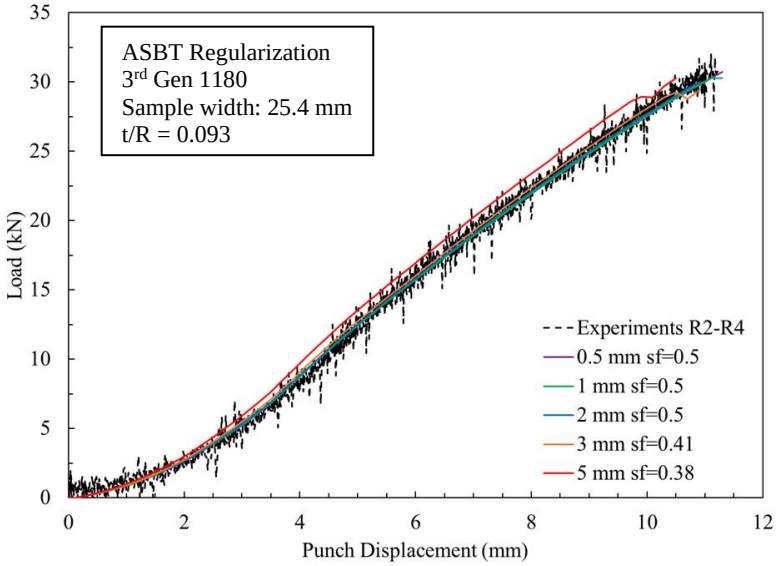

Figure B-5 - Load-displacement regularization (1in-51-15)

To gain insight into the ASBT regularization factors, the results of the regularization are shown below in Figure B-6, including the other coupon tests used for regularization completed for the research project. Note that the EB and PS dome tests have a bend severity of 0.028.

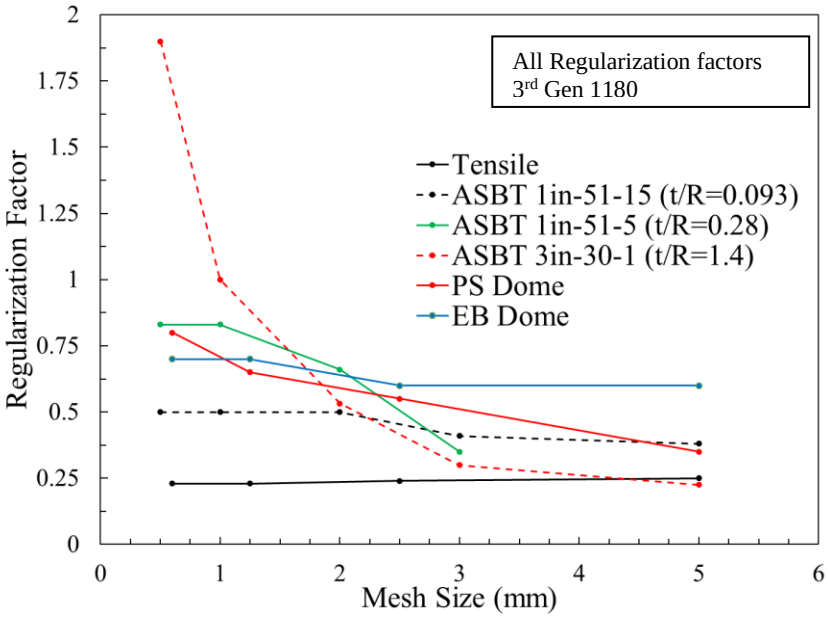

Figure B-6 - 3rd Gen 1180 Regularization factors (tensile, ASBT, PS/EB domes)

As expected, the regularization factors for the tensile test are very similar at all mesh sizes. This is an expected result since there is no bending present and the shell element accuracy will increase as the bend severity decreases. For the same reason the ASBT regularization factors are more consistent when the bend severity is decreased. Interestingly, the PS and EB domes $(t/R = 0.028)$ exhibit more variance than the ASBT even though the bend severity is 10 times lower.

Another important distinction that needs to be made when observing Figure B-6 is that the regularization factors shown are not created under identical strain paths. The tensile test produces a uniaxial strain path, with the closest comparison being the ASBT 25.4 mm sample, 51 mm die gap width, and 15 mm punch test condition. Additionally, although the coupon test is denoted as a plane strain dome test, the magnitude of the minor strain produced in the PS dome test is large compared to the ASBT 76.2 mm sample, 30 mm die gap width, 1 mm punch test condition. Therefore, caution must be exercised when comparing the regularization factors shown in Figure B-6.

The regularization factors provided by the ASBT can prove useful in forming situations, however, a cautious approach should be applied when using shell elements to model the ASBT. Although regularization with solid elements would be ideal, the additional cost of calibrating the fracture locus and using solid element simulations is very high.

The 3rd Gen 1180 material used in this thesis was characterized and formed into a B-pillar by Gutierrez et al. [44], where numerous splitting locations were predicted using AutoForm R8 software. The authors noted that various split locations were predicted in the model but in forming trials only one predicted location split for 7 of 10 B-pillars. The AutoForm model used an in-plane FLC (created using in-plane tests) and the predicted split locations were areas of the material in a plane strain bending state. When studying the regularization factors of the tensile ($t/R = 0$) vs. the ASBT 3in-30-1 ($t/R = 1.4$), it is clear that the formability produced with the ASBT is higher. Gutierrez et al. [44] concluded that a combination of high bend severity, tool contact pressure, and non-linear strain path in the predicted split locations were factors in contributing to the increased formability observed relative to the in-plane FLC.

APPENDIX C. Contact Stress

LS-DYNA Mortar Contact Stress

The mortar contact in LS-DYNA is a penalty-based, segment-to-segment contact; the mortar contact stress is given by

$$\sigma_c = \varepsilon \alpha_m K_s f\left(\frac{d}{\varepsilon d_c}\right) \tag{6.1.1}$$

where $\varepsilon = 0.03, \alpha_m$ is a stiffness scaling factor, K_s is the stiffness modulus of the slave segment, d_c is the characteristic length of the slave segment, and

$$f(x) = \begin{cases} \frac{1}{4}x^2 & x < \frac{1}{4\varepsilon} \\ cubic\ \ function\, that\, depends\, on\, IGAP & \frac{1}{4\varepsilon} \le x \end{cases}. \tag{6.1.2}$$

The IGAP parameter dramatically alters the contact stress for moderate-to-large penetrations which is shown in Figure C-1. Modifying IGAP is recommended if contact release occurs [39]. The details for contact settings used in the simulations are shown in Table 5-3.

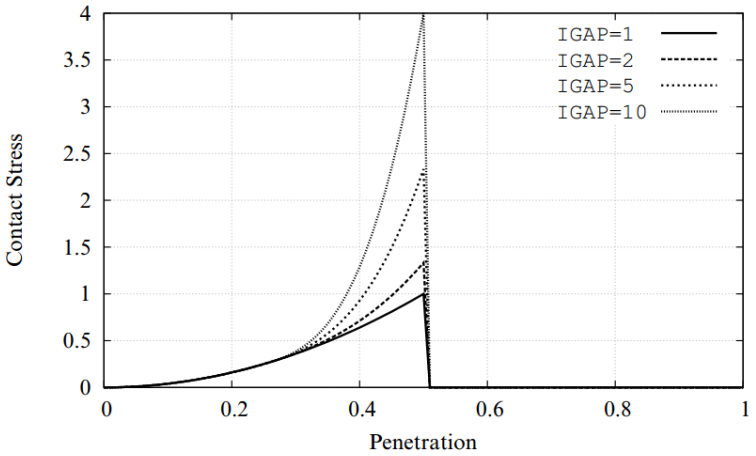

Figure C-1 - Effect of the IGAP parameter on the mortar contact stress

APPENDIX D. Experimental Data

LBF Limit Strains and Corrected Limit Strains

Table D-1 – 590R Limit Strains (25.4 mm sample)

Gap width (mm)	Punch radius (mm)	Experiment	Mod. LBF $\varepsilon_1, \varepsilon_2$	Linearized $\varepsilon_1, \varepsilon_2$	Pressure corrected $\varepsilon_1, \varepsilon_2$
30	1	R1	0.318, -0.010	0.318, -0.010	0.187, -0.008
30	1	R2	0.322, -0.014	0.322, -0.016	0.183, -0.012
30	1	R3	0.328, -0.014	0.329, -0.015	0.192, -0.012
30	10	R1	0.347, -0.073	0.349, -0.071	0.186, -0.048
30	10	R2	0.345, -0.076	0.346, -0.074	0.183, -0.050
30	10	R3	0.336, -0.073	0.337, -0.070	0.184, -0.048
76.2	1	R2	0.294, -0.018	0.294, -0.015	0.196, -0.012
76.2	1	R3	0.295, -0.018	0.294, -0.014	0.187, -0.011
76.2	10	R1	0.350, -0.073	0.348, -0.060	0.212, -0.043
76.2	10	R2	0.351, -0.074	0.349, -0.060	0.207, -0.043
76.2	10	R3	0.351, -0.074	0.348, -0.059	0.205, -0.042

Table D-2 - 590R Limit Strains (76.2 mm sample)

Gap width (mm)	Punch radius (mm)	Experiment	Mod. LBF $\varepsilon_1, \varepsilon_2$	Linearized $\varepsilon_1, \varepsilon_2$	Pressure corrected $\varepsilon_1, \varepsilon_2$
30	1	R2	0.308, -0.008	0.310, -0.011	0.181, -0.009
30	1	R3	0.272, -0.003	0.271, -0.002	0.135, -0.004
30	5	R1	0.303, -0.016	0.303, -0.015	0.138, -0.01
30	5	R2	0.290, -0.017	0.291, -0.017	0.135, -0.011
30	5	R3	0.302, -0.015	0.300, -0.013	0.146, -0.009
30	10	R1	0.330, -0.032	0.326, -0.018	0.147, -0.012
30	10	R2	0.310, -0.029	0.305, -0.013	0.142, -0.009
30	10	R3	0.308, -0.031	0.302, -0.019	0.151, -0.013
51	1	R1	0.288, -0.006	0.290, -0.01	0.177, -0.008
51	1	R2	0.262, -0.006	0.264, -0.007	0.179, -0.007
51	1	R3	0.283, -0.007	0.281, -0.004	0.183, -0.005
51	5	R1	0.313, -0.019	0.310, -0.012	0.180, -0.010
51	5	R2	0.335, -0.016	0.332, -0.012	0.187, -0.010
51	5	R3	0.308, -0.017	0.307, -0.014	0.182, -0.011
51	10	R1	0.312, -0.028	0.307, -0.017	0.169, -0.012
51	10	R2	0.312, -0.027	0.311, -0.019	0.172, -0.014
51	10	R3	0.311, -0.033	0.306, -0.020	0.173, -0.015
76.2	1	R1	0.294, -0.008	0.293, -0.007	0.190, -0.006
76.2	1	R2	0.305, -0.008	0.314, 9.3E-4	0.195, -0.002
76.2	1	R3	0.304, -0.007	0.301, -0.002	0.191, -0.004
76.2	5	R1	0.298, -0.016	0.297, -0.013	0.176, -0.010
76.2	5	R2	0.329, -0.010	0.327, -0.011	0.176, -0.009
76.2	5	R3	0.311, -0.018	0.308, -0.013	0.191, -0.010
76.2	10	R1	0.310, -0.028	0.307, -0.018	0.183, -0.013
76.2	10	R2	0.302, -0.028	0.298, -0.017	0.178, -0.013
76.2	10	R3	0.313, -0.030	0.308, -0.016	0.178, -0.012

Table D-3 – 3rd Gen 1180 Limit Strains (25.4 mm sample)

Gap width (mm)	Punch radius (mm)	Experiment	Mod. LBF $\varepsilon_1, \varepsilon_2$	Linearized $\varepsilon_1, \varepsilon_2$	Pressure corrected $\varepsilon_1, \varepsilon_2$
51	5	R1	0.267, -0.025	0.270, -0.030	0.129, -0.018
51	5	R2	0.266, -0.023	0.268, -0.028	0.123, -0.016
51	5	R3	0.277, -0.021	0.280, -0.030	0.145, -0.019
51	5	R4	0.265, -0.024	0.270, -0.040	0.112, -0.020
51	15	R2	0.236, -0.066	0.238, -0.078	0.082, -0.031
51	15	R3	0.255, -0.051	0.257, -0.071	0.091, -0.029
51	15	R4	0.240, -0.064	0.243, -0.077	0.084, -0.031
51	15	R5	0.262, -0.074	0.270, -0.075	0.095, -0.030

Table D-4 – 3rd Gen 1180 Limit Strains (76.2 mm sample)

Gap width (mm)	Punch radius (mm)	Experiment	Mod. LBF $\varepsilon_1, \varepsilon_2$	Linearized $\varepsilon_1, \varepsilon_2$	Pressure corrected $\varepsilon_1, \varepsilon_2$
30	1	R1	0.201, 0.001	0.199, 0.006	0.105, 0.001
30	1	R2	0.196, -0.001	0.196, -0.001	0.102, -0.003
30	1	R3	0.202, -0.002	0.205, -0.009	0.107, -0.007
30	1	R4	0.207, -0.003	0.215, -0.021	0.108, -0.013
30	1	R5	0.198, -0.003	0.195, -0.005	0.107, 0.001
30	1	R6	0.207, -0.006	0.211, -0.016	0.103, -0.010

Table D-5 - DP980 Limit Strains (25.4 mm)

Gap width (mm)	Punch radius (mm)	Experiment	Mod. LBF $\varepsilon_1, \varepsilon_2$	Linearized $\varepsilon_1, \varepsilon_2$	Pressure corrected $\varepsilon_1, \varepsilon_2$
51	5	R1	0.300, -0.030	0.304, -0.035	0.185, -0.027
51	5	R2	0.281, -0.030	0.283, -0.036	0.250, -0.034
51	5	R4	0.297, -0.030	0.299, -0.038	0.169, -0.028
51	15	R1	0.347, -0.102	0.355, -0.087	0.205, -0.061
51	15	R2	0.338, -0.102	0.347, -0.084	0.203, -0.059
51	15	R3	0.330, -0.097	0.340, -0.085	0.194, -0.058

Table D-6 - DP980 Limit Strains (76.2 mm sample)

Gap width (mm)	Punch radius (mm)	Experiment	ISO-12004-2 $\varepsilon_1, \varepsilon_2$	Linearized $\varepsilon_1, \varepsilon_2$	Pressure corrected $\varepsilon_1, \varepsilon_2$
30	1	R1	0.239, 0.003	0.239, 0.001	0.157, -0.002
30	1	R2	0.256, 0.004	0.258, 2.3E-4	0.164, -0.002
30	1	R3	0.255, 0.005	0.259, 0.001	0.164, -0.002

Comparison of Raw Experimental Data and Spline-fit Data

Shown below in Figure D-1 are the raw and spline-fit strain paths on the outer, middle, and inner layers of a 590R $t/R = 1.4$ sample. The middle and inner layer strain paths were calculated using the so-called 'Min model' detailed in Chapter 4. The spline-fit provides good agreement with the general trend of the experimental strain path and reduces noise in the raw data.

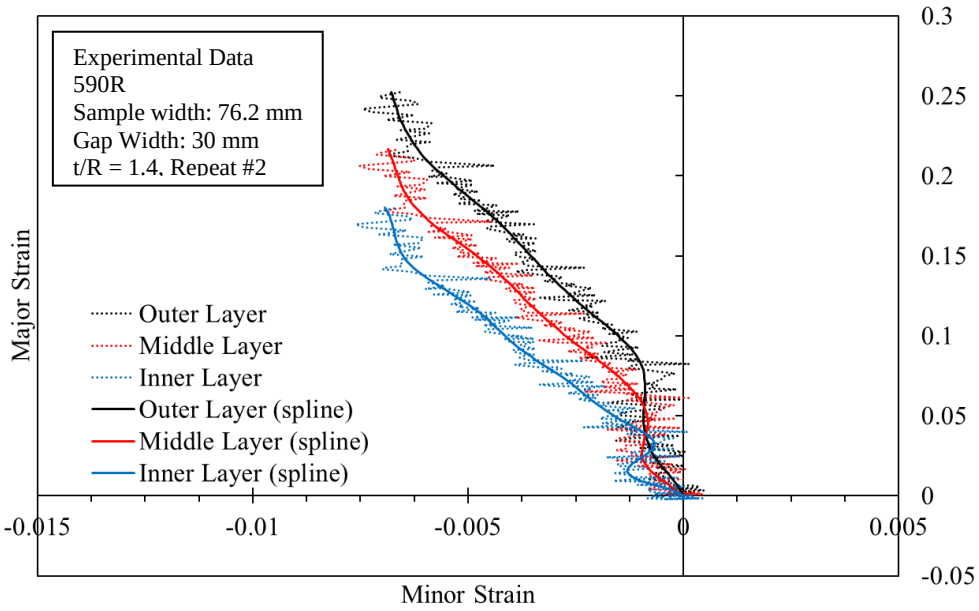

Figure D-1 - Comparison of raw and spline-fit strain path data (590R, t/R=1.4)

APPENDIX E. Tabulated Simulation Data

Punch Contact Area

Equations of the form $A_c = at^3 + bt^2 + ct + A_0$.

Shown in Table E-1 and Table E-2, are the cubic coefficients for the trendlines from the punch mesh convergence study and rigid/elastic tooling simulations respectively.

Table E-1 - Cubic coefficients for punch contact area trendlines for punch mesh convergence study

Punch Mesh	Coefficient *a*	Coefficient *b*	Coefficient *c*	A_0	R^2 value
0.2 × 0.2	0.0405	-0.1947	0.0924	7.21	0.9164
0.1 × 0.2	-0.0397	0.4786	-0.5716	3.4	0.9268
0.1 × 0.1	-0.0502	0.6362	-1.3188	3.93	0.9026
0.05 × 0.2	-0.0227	0.3128	-0.5437	3.78	0.9606
0.05 × 0.1	-0.0224	0.3103	-0.5435	3.79	0.9595
0.05 × 0.05	-0.0224	0.3087	-0.5348	3.78	0.9595

Table E-2 - Cubic coefficients for punch contact area trendlines of rigid/elastic tooling simulations

Simulation	Coefficient *a*	Coefficient *b*	Coefficient *c*	A_0	R^2 value
30-1_n=0.1_rigid	-0.1686	1.3457	-1.7602	3.7348	0.876
30-1-n=0.1_elastic	-0.0066	0.1577	0.8141	2.8969	0.9598
30-1_n=0.3_rigid	-0.0821	0.7488	-0.8214	3.4157	0.8801
30-1_n=0.3_elastic	-0.0676	0.6405	-0.4778	3.681	0.9743
30-10_n=0.1_rigid	0.011	0.2659	4.5249	5.85	0.9448
30-10_n=0.1_elastic	0.0072	0.2985	4.8734	5.85	0.9595
30-10_n=0.3_rigid	0.0384	-0.029	4.4948	5.85	0.9378
30-10_n=0.3_elastic	0.0544	-0.1965	5.2561	5.85	0.9531

Punch Displacements for Power-law material Simulations

The punch displacements in the power-law simulations were shown at percentages of the LBF limit strain punch displacement – slight differences in punch displacement was observed when comparing rigid and elastic tooling. The punch displacements used are shown in Table E-3.

Table E-3 - Punch displacements shown in through-thickness major strain distribution figures

Simulation	25% LBF	50% LBF	75% LBF	LBF (mm)
30-1_n=0.1_rigid	1.12	2.28	3.42	4.44
30-1_n=0.1_elastic	1.09	2.26	3.39	4.41
30-1_n=0.3_rigid	1.28	2.63	3.96	5.22
30-1_n=0.3_elastic	1.30	2.65	3.96	5.23
30-10_n=0.1_rigid	1.71	3.51	5.11	6.91
30-10_n=0.1_elastic	1.70	3.50	5.10	6.90
30-10_n=0.3_rigid	2.30	4.50	6.90	9.10
30-10_n=0.3_elastic	2.32	4.51	6.90	9.11